

Control and Schedule Adjustments of Battery Based Energy Storage in Low-Voltage Distribution Networks



Maximilian J. Zangs
School of Built Environment
University of Reading

A thesis submitted for the degree of
Doctor of Philosophy in Electronic Engineering

2018

It is not a dream. It is a simple feat of scientific electrical engineering. Electric power can drive the world's machinery without the need of coal, oil or gas. Although perhaps humanity is not yet sufficiently advanced to be willingly lead by the inventor's keen searching sense. Perhaps it is better in this present world of ours where a revolutionary idea may be hampered in its adolescence. All this that was great in the past was ridiculed, condemned, combatted, suppressed only to emerge all the more triumphantly from the struggle. [...] Our duty is to lay the foundation for those who are to come and to point the way, yes humanity will advance with giant strides. We are whirling through endless space with an inconceivable speed, all around everything is spinning, everything is moving, everywhere there is energy.

— Nocola Tesla

Abstract

Declaration

I confirm that this is my own work and the use of all material from other sources has been properly and fully acknowledged.

Maximilian J. Zangs

Dedication

Acknowledgements

Contents

Abstract	iii
Declaration	v
Dedication	vii
Acknowledgements	ix
Table of Contents	x
Table of Figures	xv
Nomenclature	xxiii
1 Introduction	1
1.1 Overview	1
1.2 Electrical Energy Storage	5
1.2.1 Energy Storage Technologies	7
1.2.2 Energy Storage Applications	8
1.3 New Thames Valley Vision	8
1.4 Problem Statement and Research Aim	8
1.5 Contribution	8
1.6 Publications	8

1.7	Thesis Structure	8
2	Literature Review of Storage Control	9
2.1	Overview	9
2.2	Battery Control	9
2.3	Summary of Gaps in Litearture	13
3	Improving network performance by adjusting battery operation at sub-half-hourly resolution	15
3.1	Overview	15
3.2	Key network parameters and derived cost functions	17
3.2.1	Voltage related cost functions	19
3.2.2	Power related cost functions	23
3.2.3	Current related cost functions	28
3.3	Data, models and storage scheduling	30
3.3.1	Load profiles	30
3.3.2	Network model	30
3.3.3	Battery model	32
3.3.4	ESMU scheduling	34
3.4	Optimisation method	39
3.4.1	Closed-loop schedule adjustment	40
3.4.2	Execution and result assessment procedure	41
3.5	Results and Discussion	44
3.5.1	Time Series Analysis	44
3.5.2	Difference Analysis	51
3.5.3	Probability Density Analysis	55
3.6	Summary	56

4 Real-Time Adjustment of Battery Operation using MPC Guided Schedule Deviation	59
4.1 Overview	59
4.2 System Explanation	61
4.2.1 ESMU model	62
4.2.2 Load data and ESMU scheduling	64
4.3 Control of ESMU	69
4.3.1 Dynamic control	70
4.3.2 Model predictive control	73
4.4 Case studies	75
4.5 Results and discussion	77
4.5.1 Time-series analysis	77
4.5.2 Daily peak reduction	79
4.5.3 Probability of peak reduction	81
4.6 Summary	83
5 Effects of Desynchronising Information Propagation when Distributing Smart-Charging	85
5.1 Overview	85
5.2 Coordination of EV charging	87
5.2.1 EV Demand	87
5.2.2 Base Load	88
5.2.3 Scheduling Algorithm	89
5.3 Distributed Systems	95
5.3.1 MAS Implementation	96
5.3.2 MAS Desynchronisation	96
5.3.3 Cases and Performance Metrics	97
5.4 Results and Discussion	97

5.5	Summary	97
6	Cooperative Battery Operation of without Communications Infrastructure Needs	99
6.1	Overview	99
6.2	Summary	99
7	Conclusion	101
7.1	Overview of Main Findings	101
7.2	Knowledge Contribution	101
7.3	Research Limits	101
7.4	Future Work	101
Bibliography		102
A	Additional Results	113
A.1	Improving operation performance of battery schedules at sub-half-hourly resolution	113
A.1.1	Additional Time Series Analysis	113
A.1.2	Additional Difference Analysis	122
A.1.3	Probability Density Analysis	131
B	Multi-Agent Systems	137
B.1	FIPA Implementation	137
B.2	Communication Protocols	137
C	Stochastic EV Demand Model	139
D	Network Simulation Interface	141
D.1	OpenDSS	141
D.2	Java	141

D.3	MATLAB	141
D.4	Python	141

List of Figures

1.1	Annual residential demand for electricity from FES2016 [1]	3
1.2	“Gone Green” power demand comparison to 2013/14 by type (excluding losses) from FES2015 [2]	4
1.3	Energy storage applications and corresponding value for various discharge durations [?]	6
3.1	Cost function values for different substation voltages	21
3.2	Sketch of the benefits that occur when ESMU injects power into the feeder in order to mitigate the voltage drop along the cable	21
3.3	Voltage at the loads in the IEEE LV Test Case network for a total load of 440kVA against distance between the corresponding load and substation: for the quadratic fit $R^2 = 58.76\%$	22
3.4	Sample network imbalance for different phase loadings as defined in ANSI/NEMA MG 1-2011	25
3.5	Losses against increasing power demand	27
3.6	Cost of line or fuse utilisation against network current	29
3.7	A power flow plot of the IEEE-PES European Test Case Feeder, i.e. a LV distribution network in the UK.	31
3.8	Flowchart to calculate the next SOC (i.e. $SOC(t + \Delta t)$) based on current ESMU power (i.e. $s_{ESMU}(t)$) and current SOC (i.e. $SOC(t)$) .	35

3.9	Highly variable and volatile demand profile vs half-hourly demand (i.e. a forecast under perfect foresight conditions)	37
3.10	Impact of half-hourly ESMU schedule on sub-half-hourly power profile	38
3.11	ESMU schedule adjustment flow diagram	40
3.12	Method execution and results assessment flowchart	42
3.13	Voltage level modifications as noted at the ESMU's PCC by adjusting its schedule	45
3.14	Voltage level improvements at all buses in the entire distribution network due to the ESMU schedule adjustment.	47
3.15	Reduction of the network's phase unbalance due to the adjustment of the ESMU schedule.	48
3.16	Neutral power reduction due to the ESMU schedule adjustments . . .	49
3.17	Power factor cost improvements due to the adjustment of the ESMU schedule	50
3.18	Instantaneous losses of the distribution network when adjusting the ESMU schedule in order to reduce the former (energy lost: 75.9Wh for base; 74.7Wh for normal; 69.9Wh for minimised).	50
3.19	Improvement of the worst line utilisation across the entire network when adjusting the ESMU schedule correspondingly.	51
3.20	Cost-function improvement spread, when comparing against the normal ESMU operation case and when optimising for the underlying cost (a separate y-axis is introduced for the optimisation of “neutral power”).	52
4.1	(4.1a) Traditional forecast driven BESS control; (4.1b) Traditional on-line system; (4.1c) Proposed dynamic control system	61
4.2	An example of applying a half-hourly ESMU schedule to its half-hourly schedule (Subfig. 4.2a) and the actual, sub-half-hourly daily load (Subfig. 4.2b).	68

4.3	Dynamic controller breakdown as previously shown in Figure 4.1c. . .	69
4.4	Underlying time-series based compensation strategy for compensator PID ₂	71
4.5	Exogenous auto-regressive model that is used for model predictive con- trol. Here, $t - \Delta t$ indicates the time delay by one sample period. . . .	74
4.6	Time series performance over a single day when using realistic load forecasts: (4.6a) total day; (4.6b) zoomed in on critical period	78
4.7	Daily peak reduction when using realistic forecasts.	80
4.8	Probability of load peak when using realistic forecasts.	81
4.9	Probability of load peak reduction when using realistic forecasts. . . .	82
5.1	Agent synchronisation before re-scheduling their EVs charging profile.	89
5.2	Charging power (green line) allocation on top of base network load (black line) for valley-filling behaviour. Here $n = 1$ for Fig. 5.2a, $n = 2$ for Fig. 5.2b, $n = 3$ for Fig. 5.2c, and $n = N$ for Fig. 5.2d. . .	91
5.3	A simplified MAS structure containing virtual seller and buyer agents (white), that negotiate power/charging profiles for physical entities (grey).	96
5.4	The implementation of FIPA on <i>HTCondor</i>	97
A.1	Additional substation voltage level comparison between base, normal and the case where the ESMU's schedule was adjusted.	114
A.2	Additional ESMU voltage level comparison between base, normal and the case where the ESMU's schedule was adjusted.	115
A.3	Additional voltage level comparison between base, normal and the case where the ESMU's schedule was adjusted.	116
A.4	Additional phase unbalance cost comparison between base, normal and the case where the ESMU's schedule was adjusted.	117

A.5 Additional power factor cost comparison between base, normal and the case where the ESMU's schedule was adjusted.	118
A.6 Additional comparison of the substation fuse utilisation between base, normal and the case where the ESMU's schedule was adjusted.	119
A.7 Additional line utilisation comparison between base, normal and the case where the ESMU's schedule was adjusted.	120
A.8 Additional comparison of distribution loss cost between base, normal and the case where the ESMU's schedule was adjusted.	121
A.9 Cost difference spread, based on the ESMU schedule adjustment to minimise substation voltage deviation	122
A.10 Cost difference spread, based on the ESMU schedule adjustment to minimise ESMU's PCC voltage deviation	123
A.11 Cost difference spread, based on the ESMU schedule adjustment to minimise the maximum voltage deviation on any bus of the network .	124
A.12 Cost difference spread, based on the ESMU schedule adjustment to minimise the network's phase unbalance	125
A.13 Cost difference spread, based on the ESMU schedule adjustment to minimise the network's power flow in the neutral conductor	126
A.14 Cost difference spread, based on the ESMU schedule adjustment to minimise the network's offset to unity power factor	127
A.15 Cost difference spread, based on the ESMU schedule adjustment to minimise the substation's fuse utilisation	128
A.16 Cost difference spread, based on the ESMU schedule adjustment to minimise the maximum line utilisation of any line in the network . .	129
A.17 Cost difference spread, based on the ESMU schedule adjustment to minimise distribution losses	130
A.18 Raw time-series that are supposed to be compared.	132

A.19 Rescaled time-series that are supposed to be compared.	132
A.20 Averaged log-scaled time-series.	133
A.21 Splitting of the conditioned data into two stationary sections	133
A.22 Difference of the two pre-conditioned time-series.	134
A.23 Auto-correlation of signal for (A.23a) morning and (A.23b) afternoon sections	134

Nomenclature

Acronyms

AR	Auto-Regressive
ARMAX	Auto-Regressive Moving-Average Exogenous
ARX	Auto-Regressive Exogenous
BES	Battery Energy Storage
BESS	Battery Energy Storage System
CAES	Compressed Air Energy Storage
DG	Distributed Generation
DNO	Distribution Network Operator
DOD	Depth of Discharge
DSM	Demand Side Management
DSR	Demand Side Response
EPRI	Electric Power Research Institute
ESMU	Energy Storage Management Unit
ESQCR	Electricity Supply Quality and Continuity Regulations
ESS	Energy Storage Solution
EV	Electric Vehicle
FCES	Fuel Cell driven Energy Storage
FIPA	Foundation for Intelligent Physical Agents
GB	Great Britain
JADE	Java Agent Development Environment

LCT	Low Carb on Technology
MPC	Mode-Predict Control
NARX	Nonlinear Auto-Regressive Exogenous
NTVV	New Thames Valley Vision
P2N	Phase to Neutral
P2P	Phase to Phase
PCC	Point of Common Coupling
PID	Proportional Integrating Derivative (control)
PMU	Power Management Unit
PV	Photo Voltaic
SMU	Storage Management Unit
SOC	State of Charge
SPC	Set-Point Control
SQP	Sequential Quadratic Programming
SSEN	Scottish and Southern Electricity Networks
TES	Thermal Energy Storage
UK	United Kingdom
VPP	Virtual Power Plant

Definition variables and dimensionality

$(x(t)) = \mathbf{x}$	The element $x(t)$ is part of the vector \mathbf{x}
\mathbb{C}^B	The B -dimensional set of all complex numbers (e.g. $\mathbb{Z}^{N \times 3}$ is $N \times 3$ dimensional)
\mathbb{R}_B^A	The A -dimensional set of all real numbers that lie within a range defined in B (e.g. $\mathbb{R}^{N \times 3}$ is $N \times 3$ dimensional set of all real numbers greater than or equal to zero)
\mathbb{Z}_B^A	The A -dimensional set of all integers that lie within a range defined in B (e.g. $\mathbb{Z}^{N \times 3}$ is $N \times 3$ dimensional set of all integers greater than or equal to zero)
\mathbf{X}	A matrix named \mathbf{X}

\mathbf{x}	A vector named \mathbf{x}
$x \in (0, 1)$	Scalar named x can take any number within in the exclusive range between zero and one
$x \in [0, 1]$	Scalar named x can take any number within in the inclusive range between zero and one
$x \in \{0, \dots, N\}$	Scalar named x can take any number within the discrete set of numbers of the sequence $\{0, \dots, N\}$
x	A scalar named x

Symbols used in Chapter 3

$\Delta E_{\text{bat}}(t)$	Change in stored energy at time t , where $\Delta E_{\text{bat}}(t) \in \mathbb{R}$ (Chapter 3)
$\delta s_{\text{ESMU},\phi}(t)$	Three-phase apparent ESMU power adjustment vector at time t , where $(\delta s_{\text{ESMU},\phi}(t)) = \delta \mathbf{s}_{\text{ESMU}}(t)$ and $\delta s_{\text{ESMU},\phi}(t) \in \mathbb{C}$ (Chapter 3)
Δt	Sample time, where $\Delta t \in \mathbb{Z}_{\geq 0}$ (Chapter 3)
$\delta \mathbf{s}_{\text{ESMU}}(t)$	Three-phase apparent ESMU power adjustment vector at time t , where $(\delta s_{\text{ESMU},\phi}(t)) = \delta \mathbf{s}_{\text{ESMU}}(t)$ and $\delta \mathbf{s}_{\text{ESMU}}(t) \in \mathbb{C}^{\Phi}$ (Chapter 3)
η	Round-trip efficiency of power electronics, where $\eta \in (0, 1]$ (Chapter 3)
μ	Self-discharge losses of battery, where $\mu \in (0, 1]$ (Chapter 3)
Φ	Number of phases, where $\Phi \in \mathbb{Z}_{>0}$ here $\Phi = 3$ (Chapter 3)
ϕ	Phase number, where $\phi \in \{1, \dots, \Phi\}$ (Chapter 3)
$\mathbf{i}_{\text{line}}(t)$	Multi-phase line currents at time t , where $(i_{\text{line},l,\phi}(t)) = \mathbf{i}_{\text{line}}(t)$, and $\mathbf{i}_{\text{line}}(t) \in \mathbb{R}^{L \times \Phi}$ (Chapter 3)
$\mathbf{i}_{ss}(t)$	Multi-phase substation current at time t , where $\mathbf{i}_{ss}(t) \in \mathbb{R}^{\Phi}$ (Chapter 3)
$\mathbf{s}_{\text{net}}^*$	Half-hourly network load, where $\mathbf{s}_{\text{net}}^* \in \mathbb{C}^{\frac{T_{\text{sch}}}{K}}$ (Chapter 3)
$\mathbf{s}_{\text{ESMU}}(t)$	Three-phase apparent ESMU power at time t , where $(s_{\text{ESMU},\phi}(t)) = \mathbf{s}_{\text{ESMU}}(t)$ and $\mathbf{s}_{\text{ESMU}}(t) \in \mathbb{C}^{\Phi}$ (Chapter 3)
$\mathbf{s}_{\text{load}}(t)$	Apparent load power vector of all loads at time t , where $\mathbf{s}_{\text{load}}(t) \in \mathbb{C}^I$ (Chapter 3)
$\mathbf{s}_{ss}(t)$	Apparent multi-phase power at substation level at time t , where $\mathbf{s}_{ss}(t) \in \mathbb{C}^{\Phi}$ (Chapter 3)

$\mathbf{v}_{\text{ESMU}}(t)$	Multi-phase voltage vector at ESMU at time t , where $(v_{\text{ESMU},\phi}(t)) = \mathbf{v}_{\text{ESMU}}(t)$ and $v_{\text{ESMU},\phi}(t) \in \mathbb{C}^\Phi$ (Chapter 3)
$\mathbf{v}_{\text{load}}(t)$	Multi-phase load voltage vector at time t , where $(v_{\text{load},i,\phi}(t)) = \mathbf{v}_{\text{load}}(t)$ and $\mathbf{v}_{\text{load}}(t) \in \mathbb{C}^{I \times \Phi}$ (Chapter 3)
$\mathbf{v}_{ss}(t)$	Phase voltage vector at time t , where $\mathbf{v}_{ss}(t) \in \mathbb{R}^\Phi$ (Chapter 3)
$\text{UF}(\mathbf{x})$	Function calculating the Unbalance Factor (UF) for any multidimensional vector \mathbf{x} , where $(x_n) = \mathbf{x}$, $n \in \mathbb{Z}_{>0}$ and $\text{UF}(\mathbf{x}) \in \mathbb{R}_{\geq 0}$ (Chapter 3)
$\zeta_{\text{fuse utilisation}}(\mathbf{i}_{ss}(t))$	Fuse utilisation cost, derived from multi-phase substation current vector \mathbf{i}_{ss} at time t , where $\zeta_{\text{fuse utilisation}}(\mathbf{i}_{ss}(t)) \in \mathbb{R}_{\geq 0}$ (Chapter 3)
$\zeta_{\text{load voltage}}(\mathbf{v}(t))$	Voltage deviation cost for load voltage vector \mathbf{v} at time t and $\zeta_{\text{load voltage}}(\mathbf{v}(t)) \in \mathbb{R}_{\geq 0}$ (Chapter 3)
$\zeta_{\text{losses}}(s(t))$	Losses based cost function, where $\zeta_{\text{losses}}(s(t)) \in \mathbb{R}_{\geq 0}$ (Chapter 3)
$\zeta_{\text{MMD}}(\mathbf{s})$	Cost of the underlying power profile \mathbf{s} , based on the Minimum-Maximum Difference (MMD), where $\zeta_{\text{MMD}}(\mathbf{s}) \in \mathbb{R}_{\geq 0}$ (Chapter 3)
$\zeta_{\text{neutral load}}(\mathbf{s}(t))$	Neutral load cost function for multi-phase apparent power vector \mathbf{s} at time t , where $\zeta_{\text{neutral load}}(\mathbf{s}(t)) \in \mathbb{R}_{\geq 0}$ (Chapter 3)
$\zeta_{\text{PAR}}(\mathbf{s})$	Cost of the underlying power profile \mathbf{s} , based on the Peak to Average Ratio (PAR), where $\zeta_{\text{PAR}}(\mathbf{s}) \in \mathbb{R}_{\geq 0}$ (Chapter 3)
$\zeta_{\text{PF}}(\mathbf{s}(t))$	Power Factor (PF) cost function for multi-phase apparent power vector \mathbf{s} at time t , where $\zeta_{\text{PF}}(\mathbf{s}(t)) \in \mathbb{R}_{\geq 0}$ (Chapter 3)
$\zeta_{\text{TRA}}(\mathbf{s})$	Cost of the underlying power profile \mathbf{s} , based on the power transients (TRA), where $\zeta_{\text{MMD}}(\mathbf{s}) \in \mathbb{R}_{\geq 0}$ (Chapter 3)
$\zeta_{\text{unbalance}}(\mathbf{s}(t))$	Power unbalance for multi-phase apparent power vector \mathbf{s} at time t , where $\zeta_{\text{unbalance}}(\mathbf{s}(t)) \in \mathbb{R}_{\geq 0}$ (Chapter 3)
$\zeta_{\text{voltage}}(\mathbf{v}(t))$	Voltage deviation cost for voltage vector \mathbf{v} at time t , where $\zeta_{\text{voltage}}(\mathbf{v}(t)) \in \mathbb{R}_{\geq 0}$ (Chapter 3)
C_{bat}	Battery capacity, where $C_{\text{bat}} \in \mathbb{R}_{>0}$ (Chapter 3)
C_f	Charge factor or “C-factor” of the battery, where $C_f \in \mathbb{R}_{>0}$ (Chapter 3)
$E_{\text{bat}}(t)$	Energy stored in battery at time t , where $E_{\text{bat}}(t) \in \mathbb{R}_{>0}$ (Chapter 3)
I_{fuse}	Nominal fuse rating at substation, where $I_{\text{fuse}} \in \mathbb{R}$ (Chapter 3)

$i_{\text{line},l,\phi}(t)$	Single-phase line current for phase ϕ of line l at time t , where $i_{\text{line},l,\phi}(t) \in \mathbb{R}$ (Chapter 3)
$I_{\text{nom},l}$	Nominal line current for line l , $I_{\text{nom},l} \in \mathbb{R}$ (Chapter 3)
$i_{\text{ss},\phi}(t)$	Single-phase substation current for phase ϕ at time t , where $i_{\text{ss},\phi}(t) \in \mathbb{R}$ (Chapter 3)
K	Number of sample periods over which the sub-half-hourly is to be downsampled, where $K \in \mathbb{Z}_{>0}$ and $\frac{T_{\text{sch}}}{K} \in \mathbb{Z}_{>0}$ (Chapter 3)
$k(t)$	Synchronisation function used to downsample the sub-half-hourly profile (Chapter 3)
L	Number of lines, where $L \in \mathbb{Z}_{>0}$ (Chapter 3)
l	Line number, where $l \in [1, \dots, L]$ (Chapter 3)
$p_{\text{bat}}(t)$	Single-phase active battery power at time t , where $p_{\text{bat}}(t) \in \mathbb{R}$ (Chapter 3)
$s_{\text{net}}^*(t)$	Half-hourly network load, where $(s_{\text{net}}^*(t)) = \mathbf{s}_{\text{net}}^*$ and $s_{\text{net}}^*(t) \in \mathbb{C}$ (Chapter 3)
$s_{\text{losses}}(t)$	Total apparent power losses in the network $s_{\text{losses}}(t) \in \mathbb{C}$ (Chapter 3)
$s_{\text{net}}(t)$	Apparent network load at time t , where $s_{\text{net}}(t) \in \mathbb{C}$ (Chapter 3)
S_{rating}	Rating of battery's power electronics, where $S_{\text{rating}} \in \mathbb{R}_{>0}$ (Chapter 3)
$s_{\text{ESMU},\phi}(t)$	Single-phase apparent ESMU power for phase ϕ at time t , where $(s_{\text{ESMU},\phi}(t)) = \mathbf{s}_{\text{ESMU}}(t)$ and $s_{\text{ESMU},\phi}(t) \in \mathbb{C}$ (Chapter 3)
$s_{\text{load},i}(t)$	Apparent load power for load i at time t , where $(s_{\text{load},i}(t)) = \mathbf{s}_{\text{load}}(t)$ and $s_{\text{load},i}(t) \in \mathbb{C}$ (Chapter 3)
$s_{\text{ss},\phi}(t)$	Apparent single-phase power at substation level for phase ϕ at time t , where $(s_{\text{ss},\phi}(t)) = \mathbf{s}_{\text{ss}}(t)$ (Chapter 3)
$SOC(t)$	State of charge at time t , where $SOC(t) \in (0, 1)$ (Chapter 3)
T	Length of simulation, where $T \in \mathbb{Z}_{\geq 0}$ (Chapter 3)
t	Time-steps of the simulation, where $t \in \{1, \Delta t, 2\Delta t, \dots, T\}$ (Chapter 3)
T_{sch}	Scheduling horizon, where $T_{\text{sch}} \in \mathbb{Z}_{>0}$ (Chapter 3)
V_{ss}	Nominal substation voltage, where $V_{\text{ss}} \in \mathbb{R}$ (Chapter 3)
V_h	High-voltage threshold of statutory voltage band, where $V_h \in \mathbb{R}$ (Chapter 3)

V_l	Low-voltage threshold of statutory voltage band, where $V_l \in \mathbb{R}$ (Chapter 3)
$v_{\text{ESMU},\phi}(t)$	Phase voltage at ESMU for phase ϕ at time t , where $(v_{\text{ESMU},\phi}(t)) = \mathbf{v}_{\text{ESMU}}(t)$ and $v_{\text{ESMU},\phi}(t) \in \mathbb{C}$ (Chapter 3)
$v_{\text{load},i,\phi}(t)$	Phase voltage of load i for phase ϕ at time t , where $(v_{\text{load},i,\phi}(t)) = \mathbf{v}_{\text{load}}(t)$ and $v_{\text{load},i,\phi}(t) \in \mathbb{C}$ (Chapter 3)
$v_{\text{ss},\phi}$	Phase voltage at substation for phase ϕ at time t , where $(v_{\text{ss},\phi}(t)) = \mathbf{v}_{\text{ss}}(t)$ (Chapter 3)

Symbols used in Chapter 4

$\boldsymbol{\alpha}$	PID weight vector for compensator PID_1 , where $\boldsymbol{\alpha} = \{\alpha_P, \alpha_I, \alpha_D\}$ and $\boldsymbol{\alpha} \in \mathbb{R}^3$
$\boldsymbol{\beta}$	PID weight vector for compensator PID_2 , where $\boldsymbol{\beta} = \{\beta_P, \beta_I, \beta_D\}$ and $\boldsymbol{\beta} \in \mathbb{R}^3$
Δt	Sub-half-hourly sample period, where $\Delta t \in \mathbb{Z}^{>0}$
η	Round-trip efficiency of power electronics, where $\eta \in (0, 1]$
$\hat{p}_{\text{net}}(t + \Delta t)$	Predicted next network power at sample t
μ	Self-discharge losses of battery, where $\mu \in (0, 1]$
\mathbf{a}	Weight vector for compensator input regression of the AR model, where $\mathbf{a} = \mathbb{R}^N$
\mathbf{b}	Weight vector for compensator output regression of the AR model, where $\mathbf{b} = \mathbb{R}^N$
\mathbf{p}	ESMU power vector, where $(p(t)) = \mathbf{p}$
\mathbf{p}_{for}	Half-hourly load forecast vector that is used for computing the ESMU schedule, where $(p_{\text{for}}(k(t))) = \mathbf{p}_{\text{for}}$
\mathbf{p}_{sch}	Half-hourly schedule vector that is generated from the load forecast, where $(p_{\text{sch}}(k(t))) = \mathbf{p}_{\text{sch}}$
\mathbf{p}_{bat}	Battery power vector, where $(p_{\text{bat}}(t)) = \mathbf{p}_{\text{bat}}$
$\zeta(\mathbf{p})$	Global cost for a given power profile \mathbf{p}
$\zeta_{\text{MMD}}(\mathbf{p})$	Cost of a power profile \mathbf{p} , based on the difference between minimum and maximum power, where $\zeta_{\text{MMD}}(\mathbf{p}) \in \mathbb{R}_{\geq 0}$
$\zeta_{\text{PAR}}(\mathbf{p})$	Cost of a power profile \mathbf{p} , based on Peak-to-Average Ratio (PAR), where $\zeta_{\text{PAR}}(\mathbf{p}) \in \mathbb{R}_{\geq 0}$

$\zeta_{\text{TRA}}(\mathbf{p})$	Cost of a power profile \mathbf{p} , based on largest power transient, where $\zeta_{\text{TRA}}(\mathbf{p}) \in \mathbb{R}_{\geq 0}$
C_{bat}	Battery capacity in kWh, where $C_{\text{bat}} \in \mathbb{Z}^{>0}$
C_f	Charge factor or “C-factor” of the battery, where $C_f \in \mathbb{Z}^{>0}$
$E_{\text{SOC}}(t)$	Error in state of charge at sample t , where $E_{\text{SOC}}(t) \in \mathbb{R}$
$E_p(t)$	Difference between current and predicting network power at sample t , where $E_p(t) \in \mathbb{R}$
$k(t)$	Sampling time conversion function, linking sub-half hourly samples t at sampling period Δr to half-hourly period $30\Delta t$
N	Number of regressors of the AR model, where $N \in \mathbb{Z}_{>0}$
$p(t)$	ESMU power at time t , where $(p(t)) = \mathbf{p}$ and $p(t) \in \mathbb{Z}$
$p_1(t)$	Corrective ESMU power components from PID ₁ , where $p_1(t) \in \mathbb{R}$
$p_2(t)$	Corrective ESMU power components from PID ₂ , where $p_2(t) \in \mathbb{R}$
$p_{\text{for}}(k(t))$	Half-hourly load forecast that is used for computing the ESMU schedule, where $p_{\text{for}}(k(t)) \in \mathbb{Z}$
$p_{\text{net}}(t)$	Most recent network demand at sample t , where $(p_{\text{net}}(t)) = \mathbf{p}_{\text{net}}$ and $p_{\text{net}}(t) \in \mathbb{R}$
$p_{\text{sch}}(k(t))$	Half-hourly schedule that is generated from the load forecast, where $p_{\text{sch}}(k(t)) \in \mathbb{Z}$
P_{bat}	ESMU power electronic rating, where $P_{\text{bat}} \in \mathbb{Z}^{>0}$
$p_{\text{bat}}(t)$	Battery power at time t , which is derived form $p(t)$, where $(p_{\text{bat}}(t)) = \mathbf{p}_{\text{bat}}$ and $p(t) \in \mathbb{Z}$
$SOC(t)$	Scheduled state of charge at sample t
$SOC^*(t)$	Battery’s state of charge at sample t , where $SOC^*(t) \in [0, 1]$
SOC_{tol}	SOC tolerance, i.e. maximum deviation from the prescheduled SOC profile, where $SOC_{\text{tol}} \in [0, 0.5]$
T	Number of samples during the entire simulation, where $T \in \mathbb{Z}_{>0}$
t	Discrete sample of time, where $t \in \{0, \Delta t, \dots, T\Delta t\}$
T_{sch}	Length of scheduling horizon, where $T_{\text{sch}} \in \mathbb{Z}_{>0}$ and $T \geq T_{\text{sch}}$

Symbols used in Chapter 5

β	Allocation parameter to assign a portion of the temporary energy demand, $\hat{E}_{u,n}$, where $\beta \in (0, 1]$ (Chapter 5)
Δt	Sample period for EV scheduling, where $\Delta t \in \mathbb{R}^{>0}$ (Chapter 5)
$\hat{\mathbf{p}}_{\text{base},n}$	Temporary demand vector, i.e. the aggregate of all EV charge vector and the base load vector, where $\hat{p}_{\text{base},n}(t) \in \hat{\mathbf{p}}_{\text{base},n}$ (Chapter 5)
$\hat{\mathbf{p}}_{\text{EV},u,n}$	Temporary charging vector during iteration number n , for EV u , where $\hat{p}_{\text{EV},u,n}(t) \in \hat{\mathbf{p}}_{\text{EV},u,n}$ (Chapter 5)
$\hat{p}_{\text{base},n}(t)$	Temporary demand at time t , i.e. the aggregate of all EV charge vector and the base load vector, where $\hat{p}_{\text{base},n}(t) \in \mathbb{Z}^{\geq 0}$ (Chapter 5)
$\hat{p}_{\text{EV},u,n}(t)$	Temporary charging power during iteration number n , for EV u , at time t , where $\hat{p}_{\text{EV},u,n}(t) \in \mathbf{Z}^{\geq 0}$ (Chapter 5)
$\mathbf{p}_{\text{base},n}$	Base load vector, where $p_{\text{base},n}(t) \in \mathbf{p}_{\text{base},n}$ (Chapter 5)
$\mathbf{p}_{\text{EV},u,n}$	Scheduled EV charging power vector, for EV u at algorithm iteration n , where $p_{\text{EV},u,n}(t) \in \mathbf{p}_{\text{EV},u,n}$ (Chapter 5)
N	Number of algorithm iterations to schedule multiple EVs, where $N \in \mathbb{Z}^{>0}$ (Chapter 5)
n	Iteration number of EV scheduling algorithm, where $N \in [1, \dots, N]$ (Chapter 5)
$p_{\text{base},n}(t)$	Base load at time t , where $p_{\text{base},n}(t) \in \mathbb{Z}^{\geq 0}$ (Chapter 5)
$p_{\text{EV},u,n}(t)$	Scheduled EV charging power, for EV u at algorithm iteration n for time t , where $p_{\text{EV},u,n}(t) \in \mathbb{R}^{\geq 0}$ (Chapter 5)
$P_{\min,u}$	Maximum EV charging power (Chapter 5)
$P_{\max,u}$	Minimum EV charging power (Chapter 5)
T_{sch}	Scheduling horizon for EV charging, where $T_{\text{sch}} \in \mathbb{Z}^{>0}$ (Chapter 5)
U	Number of EVs that need to be scheduled, where $U \in \mathbb{Z}^{>0}$ (Chapter 5)
u	EV unit number, where $u \in [1, \dots, U]$ (Chapter 5)

Chapter 1

Introduction

1.1 Overview

Today's society and its lifestyle are highly dependent on the continuous availability of energy. More specifically, electrical energy has experienced the most significant increase in demand. One reason behind this demand increase is due to the environmental aim to reduce green house gas emissions by 80% by 2050. Another reason is based on political agendas to reduce national dependence on fossil fuels like oil, coal and gas. Therefore, governments incentivised and subsidised the uptake of Low Carbon Technologies (LCTs). Ongoing electrification of heating and transport, as well as increased penetration of Distributed Generation (DG) are the results. Whilst the electricity grid's infrastructure was initially constructed to deliver electricity in a unidirectional manner, it may no longer be able to support the current energy trends. Conventional solutions are costly and disruptive network reinforcement. Instead, electrical energy storage is proposed to support the network operation and mitigate or defer network reinforcement [3, 4].

The demand for electricity in the United Kingdom (UK) has increased significantly over the past century, and reports suggest that this trend is going to continue.

National Grid, one of the big UK network operators, published their Future Energy Scenarios (FES), highlighting the challenges that are yet to come [2]. In this report, four scenarios have been identified, and National Grid explains them as follows (excerpts taken from FES [2]):

- “**Gone Green** is a world where green ambition is not restrained by financial limitations. New technologies are introduced and embraced by society, enabling all carbon and renewable targets to be met on time.”
- “**Slow Progression** is a world where slower economic growth restricts market conditions. Money that is available is spent focusing on low cost long-term solutions to achieve decarbonisation, albeit it later than the target dates.”
- “**No Progression** is a world focused on achieving security of supply at the lowest possible cost. With low economic growth, traditional sources of gas and electricity dominate, with little innovation affecting how we use energy.”
- “**Consumer Power** is a world of relative wealth, fast paced research and development and spending. Innovation is focused on meeting the needs of consumers, who focus on improving their quality of life.”

In Figure 1.1 the UK’s future residential electricity demand is plotted for each of the four scenarios. Here, despite a subtle dip towards a new low in demand during 2025, all scenarios show an increase in energy demand after 2025. Assuming that the UK is going to meet its environmental targets for 2050, National Grid’s “Gone Green” scenario may be the most likely.

In this case the total demand for electricity is predicted to significantly increase. This can be seen in Figure 1.2, where the change in national energy demand is compared against the current demand levels. Here, increased industry efficiency is foreseen to outweigh its demand for electricity, which is shown by an initially negative change

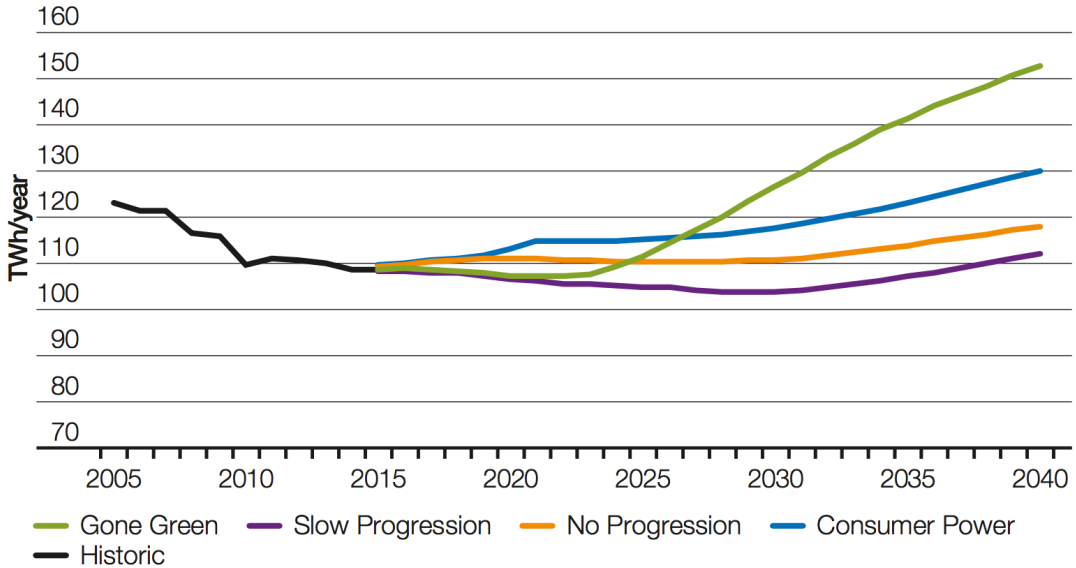


Figure 1.1: Annual residential demand for electricity from FES2016 [1]

in demand. Yet slower energy transitions in the private and commercial sector are foreseen to outweigh the industrial energy savings in 2025. Also, the ongoing uptake of sustainable technology will result in a further rise in annual residential demand, by nearly 50TWh in 2036. More than half of this residential demand, i.e. 27TWh, is expected to be caused by home charging of Electric Vehicles (EVs); which is the result of an expected 9.7 million EVs and Plug-in Hybrid EVs (PHEVs) being registered in the UK by 2040 [5]. This home charging will also have a significant impact on domestic peak power demand. In fact, it is expected to rise by as much as 6.5GW, predominantly because uncoordinated EV charging is feared to occur outside times of DG production [1].

The corresponding impact of this increased peak demand varies across the grid. For instance, the effect on the national transmission network's infrastructure is of little concern, since thermal limits are unlikely to be reached. Nonetheless, balancing demand and supply and controlling the grid's operating frequency are still key aspects that need to be considered. However, local power distribution networks are prone to thermal or voltage issues if peak demand is increased. One solution may be

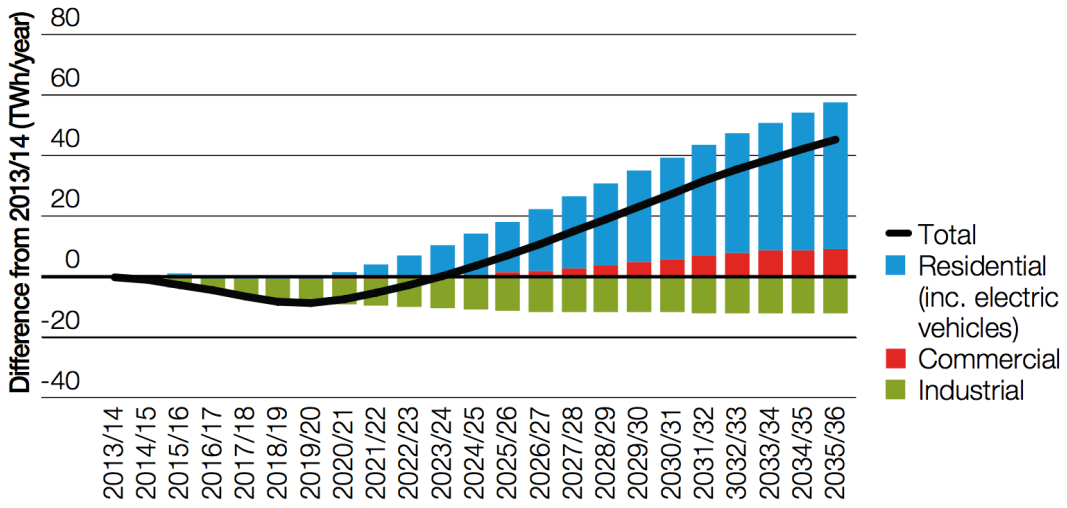


Figure 1.2: “Gone Green” power demand comparison to 2013/14 by type (excluding losses) from FES2015 [2]

the integration of Demand Side Response (DSM), where A study from 2010 shows that, as levels of EV and electric heating increase, equipment overloading becomes unavoidable unless devices are managed and coordinated intelligently [6]. In fact, the study suggests that in a Business as Usual (BaU) case, all transformers in distribution networks will overload when EV penetration reaches a level of 75%. This was shown to be the case for both areas of high demand density (i.e. 2MVA/km²) and low demand density (i.e. 0.5MVA/km²).

In the UK, Distribution Network Operators (DNOs) are the owners of the power distribution networks. Keeping this network within its operational constraints, e.g. preventing thermal overloads and voltage violations, used to be straight forward. For traditional reasons, energy is acquired in half-hourly chunks, but with the increasing electricity demand and associated power variation, estimating half-hourly demand becomes more difficult, and responding to sudden demand spikes becomes more difficult.

As already mentioned, electrical energy storage, the main focus of this research, has been identified as an valid alternative to conventional network reinforcements.

With the aforementioned challenges in mind, the author of this thesis focuses on the improved control of this storage to support the operation of the Low-Voltage (LV) power distribution network. More specifically, the question of how the important roles of electrical energy storage systems can be leveraged for both national and local benefits is addressed, and how their coordination is impacted by different external factors is researched. The remainder of this chapter explains the traditional and upcoming role of energy storage in the grid. Subsequent sections then introduce the UK distribution networks, the New Thames Valley Vision project and motivation of the author's work, the problem statement for the thesis, the novel contributions of this research and the structure of the thesis.

- Network issues including:

- Voltage deviation
- Phase unbalance
- Line utilisation
- Distribution losses

-

1.2 Electrical Energy Storage

The idea of using energy storage in the electricity grid has been discussed for quite some time, and its important role in future energy systems has already been identified in the 70s, i.e. Kalhammer [7]. As the name suggests, electrical energy storage systems have the ability to both consume, store, and release electrical energy by converting it into a different form of energy. Depending on the rate at which energy can be consumed and released, i.e. the system's power, as well as the amount of energy that can be stored, i.e. system's capacity, different functions can be provided. A study

for the Department Of Energy (DOE) showed that, when correctly exploited, these functions can yield direct financial benefits of \$157.56 billion over an estimated 10 year system lifecycle [8]. Figure 1.3 shows these benefits in relation to their typical discharge period, and links them to their associated functions, too. Here, Time Of Use (TOU) energy cost management yields the largest economic profit, yet from a historical point of view, bulk energy storage has played the most important role in the energy system. This kind of storage was used for large scale time-shifting and allowed the balancing of demand and supply without the need of ramping up or shutting down conventional power plants. Nowadays, this kind of storage can also tap into emerging revenue streams, i.e. to relief network congestion, thus deferring the need for network reinforcement whilst allowing the integration of volatile renewable energy sources. So far, 127GW of bulk energy storage has been built worldwide [?], tripling it ever since Kalhammer's publication [9, 10].

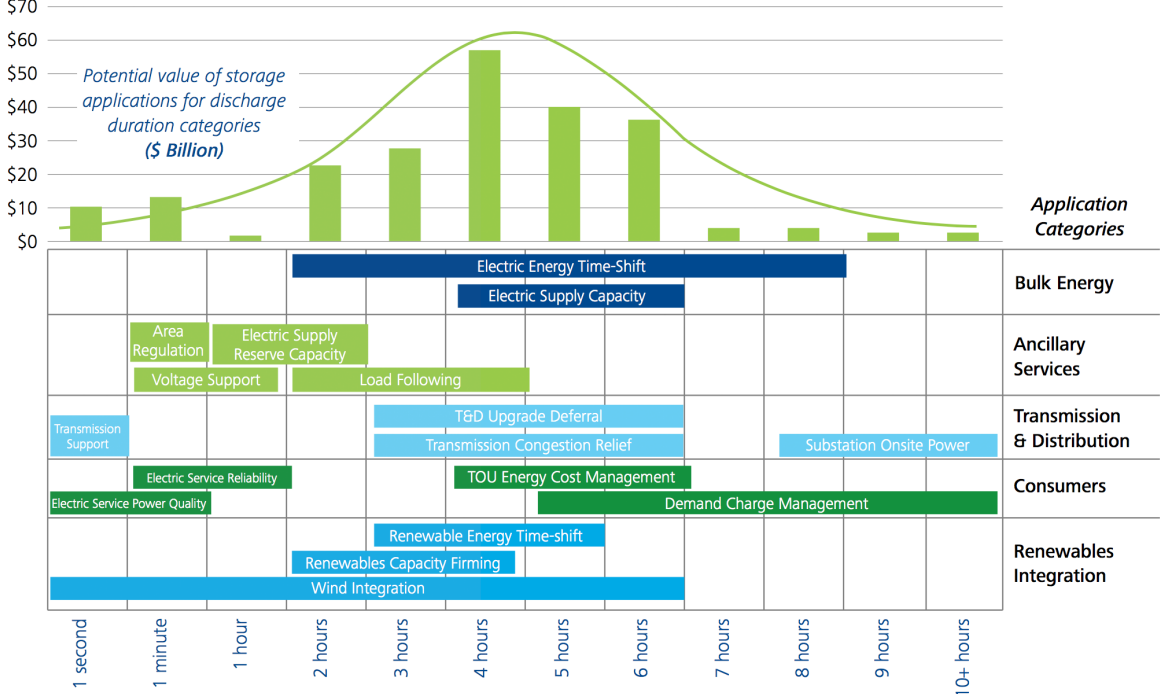


Figure 1.3: Energy storage applications and corresponding value for various discharge durations [?]

However, the scale and lack of responsiveness of such bulk energy storage systems

prevents them from being used in local distribution networks where fast system responses are required. Different energy storage technologies and their applications are briefly introduced in this section.

1.2.1 Energy Storage Technologies

The oldest form of grid scale energy storage, i.e. for bulk energy storage, is pumped hydro-electric energy storage. In 2012, 99% of bulk storage was comprised of pumped hydro [11]. Since pumped hydro is not a suitable technology for distribution network implementation, it is not considered in this technology assessment.

One of the first comprehensive reviews that included small- to medium-scale energy storage technologies was published by McLaron and Cairns [12]. They discussed electrochemical energy storage ^{*}, thermal energy storage [†], mechanical energy storage [‡], chemical energy storage [§], and magnetic energy storage [¶]. With subsequent advancements in technology, Battery Energy Storage Systems (BESS), Compressed Air Energy Storage Systems (CAESS) and Flywheel Energy Storage Systems (FESS) have become the most promising choices for deployment in distribution networks [13, 14, 15]. However, with no moving parts, the increasing energy density, and improved control systems, batteries are starting to outperform the competition. They can be deployed in ever decreasing form factors and are about to outlast their competition, too [16].

^{*}i.e. lead-acid batteries, iron/nickel-oxide batteries, zinc/chlorine batteries, zinc/bromine batteries, redox batteries, hydrogen/nickel oxide batteries, metal/air batteries, sodium/sulfur batteries, sodium/metal chloride batteries, lithium/iron sulfide batteries, and lithium/iron disulfide batteries

[†]i.e. aquifers, latent-heat storage systems, aqueous systems, salt hydrates, clathrates, molten salt systems, and more

[‡]pumped hydro-electric energy storage, compressed air energy storage, flywheel energy storage

[§]hydrogen generation, storage, transmission and utilisation

[¶]superconducting magnetic energy storage

1.2.2 Energy Storage Applications

1.3 New Thames Valley Vision

1.4 Problem Statement and Research Aim

1.5 Contribution

1.6 Publications

- M. J. Zangs, P. Adams, T. Yunusov, W. Holderbaum, and B. Potter, “Distributed Energy Storage Control for Dynamic Load Impact Mitigation,” Energies, vol. 9, no. 8, p. 647, Aug. 2016. doi: 10.3390/en9080647
- M. J. Zangs, T. Yunusov, W. Holderbaum and B. Potter, “On-line adjustment of battery schedules for supporting LV distribution network operation,” 2016 International Energy and Sustainability Conference (IESC), Cologne, 2016, pp. 1-6. doi: 10.1109/IESC.2016.7569485

1.7 Thesis Structure

Chapter 2

Literature Review of Storage Control

2.1 Overview

Technology advancements and increasing popularity of renewable energy sources, combined with government incentives to support their uptake, also lead to a significant rise in Distributed Energy Resources (DERs). Yet to allow DERs to be installed without significant negative impact on the local MV or LV networks, required functions that large scale power levelling systems could not provide. More specifically, fast response to counteract highly volatile loads or unpredictable and distributed DERs; e.g. home PV installations [17].

2.2 Battery Control

Motivation, not literature...

Outages are still very frequent in the UK. According to the UK energy regulator *OFGEM*, on average 45% of all customers experienced service disruptions in the period 2015-16 [18]. Whilst unanticipated outages due to severe winter weather lead to

\$39 million worth of damages [19], network upgrades and repairs however contributed the larger amount of customer interruptions and customer minutes lost. Such planned outages are intentions to strengthen networks and mitigate system overloads, due to increasing demand for electricity. This demand increase is only accelerated since major focus of UK energy policies has been put on transitioning towards a low carbon economy [20, 21]. Particularly the decarbonisation of heat and transport sectors are two areas of significant strategic focus and Low Carbon Technology (LCT) such as photovoltaic installations, electric vehicles and heat pumps are expected to contribute significantly to this transition.

However, as adaptation of these LCTs increases and they start to penetrate power distribution networks, stress on these networks will continue to increase even further, which may result in additional service disruptions. Furthermore, the uptake of LCTs is not expected to progress evenly throughout the entire power network, and instead clusters of early adopters are predicted to form, leading to certain Low-Voltage (LV) networks to exceed their operational constraints even at relatively low national rate of LCT adaption [22]. Traditional network planning approaches to circumvent constraint violations, follow the commonly used practice of aggregating a large number of customers and designing the power delivery network to cater for their largest probable demand, i.e. the After Diversity Maximum Demand (ADMD) method [23]. This ADMD method has remained the same for many years and uses historical load analysis and standard growth assumptions that are both no longer valid in this unprecedented LCT uptake scenario [24]. To make things worse, LV networks in the UK are generally unmonitored once installed. Distribution Network Operators (DNOs) have become aware of this issue and are developing updated planning strategies involving “smart” and “flexible” electricity grids. However, in situ equipment that will become subject to the same adaptation of LCT needs to be managed actively via innovation in the use of existing and new technologies; otherwise both frequency of

service disruptions and customer minutes lost will increase alongside the proliferation of LCTs [25].

Two solutions exist, allowing DNOs to support LV network's operation: 1. reinforcement of in situ network assets; 2. deployment of network support equipment. Whilst network reinforcement would certainly address immediate issues of current network capacity constraints, it is also the more expensive and disruptive option. More specifically, customer will need to deal with outages during periods of asset upgrades (e.g. transformer upgrade and line re-conductoring after secondary transformers' tap settings have been adjusted). Therefore, alternatives to defer or avoid network reinforcements have been sought and assessed [26, 27, 28, 29]. Most promising alternatives are to install flexible and controllable Distributed Energy Resources (DERs), or more specifically: Battery Energy Storage Solutions (BESS) [30]. BESS has not only seen significant advancements in technology, but also received increasing attention in both academic studies and industry trials [31].

Installing BESS on a strategic location in the LV network brings several advantages to DNOs' control over the network's performance. Regulating voltages to stay within statutory operating bands [32], shaving peak load to relieve stress from the installed network assets [33], or reducing phase unbalance to increase network efficiency [34] are only a few examples of recent research in this field. Whilst the questions regarding locating and scaling of BESS have mostly been addressed, BESS control can be split into two complementing yet unmarried approaches: 1. "off-line" control, using load forecasts and BESS schedules; and 2. "on-line" control, using Set-Points Control (SPC), Model Predictive Control (MPC) or similar dynamic control methods.

Off-line control uses historic data to predict future load patterns, which are used to schedule BESS operation accordingly. Early approaches, e.g. by Oudalov et al. [35], who used dynamic programming to generate BESS schedules, had a relatively high forecast error due to the inherent difficulty of predicting future loads, which ultimately

limits the ability of given BESS schedule to i.e. reduce peaks. This reason is why recent research either includes uncertainty, like the work by Baker et al. [36] where uncertainty of wind power was taken into account when scheduling and sizing BESS, or it frequently re-evaluates BESS schedules, as done by Wang et.al [37], where BESS control is adjusted after each decision epoch. Despite load forecasts being imperfect, forecasts remain a key component for scheduling BESS thanks to work like that by Rowe et al. [38], where a filtering mechanism was proposed for scheduling algorithms to reduce peak load in LV networks in spite of forecast errors. Furthermore, most day-ahead forecast only forecast at a temporal resolution down to half-hourly periods. As pointed out by Haben et al. [22, 39], forecasts at half-hourly resolution yield the best compromise between high accuracy and high temporal resolution, which is why they have become the standard for generating BESS operating schedules. Nonetheless, sub-half-hourly load volatility imposes the biggest stress on the network and cannot be addressed when using this kind of half-hourly forecast, which is why on-line control has been considered as an alternative to off-line control.

One flavour of on-line control is the Set-Point Control (SPC), which is a robust technique that can immediately respond to network changes. Since this kind of control runs the risk of reaching shortage or surplus of BESS stored energy, modifications like hysteresis control [40] and ramp-rate control [41] were proposed. However, this kind of on-line control is less effective in addressing daily demand peaks, since pure SPC can only react to current network demand and does not respond to general trends or upcoming load events. To address these shortcomings SPC has been extended, using short-term load predictions by implementing Model Predictive Control (MPC). Some MPC examples include Auto-Regressive (AR) models [42, 43], fuzzy logic models [44, 45], genetic algorithms [46, 47] or Artificial Neural Networks (ANN) [48, 49, 50, 51, 52, 53, 54]. Implementing increasingly complex MPC to support on-line control is therefore a strong research trend, however the computational burden to deliver

real-time solutions makes implementation of such systems not yet feasible.

2.3 Summary of Gaps in Litearture

Chapter 3

Improving network performance by adjusting battery operation at sub-half-hourly resolution

M. J. Zangs, et.al., “On-line adjustment of battery schedules for supporting LV distribution network operation,” 2016 International Energy and Sustainability Conference (IESC), Cologne, Germany, 2016, pp. 1-6.

— Available: <http://dx.doi.org/10.1109/IESC.2016.7569485>

3.1 Overview

Due to the trends in energy demand, future network load is expected to increase in both magnitude and volatility. As a result, DNOs have two choices to address the issues that are expected to result from increased network stress. They can either invest in network reinforcement or install network support equipment. For several reasons, e.g. decommissioning cost, installation cost, service disruption, etc., which have been outlined in Chapter 1, the installation of network support equipment was favoured. As mentioned in Section 1.3, SSEN deployed and trialled an Energy Storage Management Unit (ESMU) in some of their Low-Voltage (LV) power distribution

networks. Within the scope of their trials, ESMU had to be controlled to benefit the network, without exceeding or violating any operational constraints. In order to achieve this kind of operation, ESMU operation had to be scheduled. During this kind of operation, the system either consumes or injects power, according to a predetermined plan that changes at regular intervals. For historic reasons and system compliance, this interval was chosen to be of 30 minutes, i.e. at half-hourly period.

Since the ESMU schedule was generated based upon a demand forecast, any resulting impact on the LV network operation is therefore based upon two factors:

1. quality of the underlying forecast that is used to generate ESMU schedules, and
2. network parameters that are used to quantify the improvements that would have been expected, when the half-hourly schedule is applied.

Our previous research focused on improving half-hourly network operation to e.g. reduce peak load [38, 55]. However, in that research, sub-half-hourly demand variability has not been taken into account. Therefore, previously used performance parameters, and the corresponding measure of success, did not effectively quantify the ESMU's capability at mitigating negative impacts from this sub-half-hourly demand.

In this chapter, a closed-loop optimisation method is proposed that adjusts the ESMU's phase powers at a sub-half-hourly resolution in order to improve network operation, whilst maintaining the charging and discharging profile during the corresponding half-hourly period. Unlike previous work in the field, this approach guarantees the correct execution of the predetermined ESMU schedule, despite allowing ESMU to respond to high-resolution variations in three-phase network load.

In order to investigate how network operation may be improved, a collection of commonly used parameters are evaluated in a set of corresponding cost functions. Initially, these cost functions are minimised on an individual basis to inspect their separate impact on network performance. Then, all cost functions are combined as

a weighted sum to form a global cost function, which is used in the final analysis. For each optimisation approach, power flow simulations are run on a standardised UK power distribution feeder model in the simulation environment OpenDSS. This chapter therefore addresses the research question, whether sub-half-hourly adjustments to scheduled ESMU operation can significantly improve measured key network parameters.

The obtainment of key network parameters and their corresponding measure of improvement is explained next, in Section 3.2. All acquired data and the power network models used for this piece of work are shown in Section 3.3. Subsequently, the closed-loop optimisation method is presented in Section 3.4. At the end of this chapter, all results are presented and discussed in Section 3.5, and a concluding summary is presented in Section 3.6.

3.2 Key network parameters and derived cost functions

Two distinct approaches have emerged to quantitatively improve the performance of a system: either “cost” is reduced or “utility” is maximised. Both approaches rely on a mathematical explanation of underlying features that relate to performance of the system. The choice for this piece of work was to associate a cost to each key network parameter, for the reason that cost functions can be minimised to a finite value, i.e. zero. Utility maximisation on the other hand is a theoretically unbound problem that can only reach a maximum, if its maximum can be estimated in advance. In other words, solutions to a cost function where the resulting cost is zero, are by definition part of the set of optimal solutions. Determining the set of optimal solutions for the maximisation of a utility function is however more difficult.

With this in mind, the key network parameters are defined and their corresponding

cost functions are introduced. In this piece of work, power flow simulations are run at discrete times, t , which are separated by a sampling period Δt . The model used for these simulations is the IEEE LV Test Case, which consists of 906 three phase buses, resulting in a total of 2718 nodes. For each node, complex currents and voltages can be obtained, making the number of parameters to chose from nearly inexhaustible. In reality however, a power distribution network can only be observed at a limited number of measuring points. For the NTVV project, these points were at the substation and the ESMU’s Point of Common Coupling (PCC). Therefore, all derived network parameters that could be obtained in reality are seen as “realistic parameters”, despite the fact that all key network parameters are extracted from power flow simulations. The remaining key network parameters, i.e. those that could not easily be obtained in reality, are therefore referred to as “theoretical parameters”.

Due to the high number of theoretical parameters, only a subset of those theoretical parameters is used. The choice of parameters is based on their importance, role and impact on the actual network operation. A list of all realistic and theoretical key network parameters is presented below, and in this list all theoretical key network parameters are marked with a dagger (\dagger).

- Voltages at substation transformer’s secondary winding
- Voltages at ESMU’s PCC
- Voltages at customer lateral †
- Total power flow
- Substation line utilisation
- Maximum line utilisation †
- Distribution losses †

The following three substations cover all key network parameters, by detailing the cost functions relating to: voltages, powers and currents.

3.2.1 Voltage related cost functions

In the UK, LV networks operate at a nominal voltage of 230V Phase-to-Neutral (P2N) or 400V Phase-to-Phase (P2P). Substations supply electricity to a three-phase cable, i.e. the feeder, and link to MV distribution networks, which operate at 11kV P2P. In an ideal case the voltage measured at the substation transformer's secondary winding remains constant as load changes. But in reality, internal losses (e.g. conductive losses and magnetic leakage) lead to a dropping voltage level, when load increases. Therefore, any deviation from the substation's nominal voltage can be seen as an indication of suboptimal network operation.

The “voltage deviation cost function” $\zeta_{\text{voltage}}(\mathbf{v}(t))$ captures this suboptimal operation. This cost function is defined for a multi-phase complex voltage vector as $\mathbf{v}(t)$ where $(v_\phi(t)) = \mathbf{v}(t)$, where ϕ is the phase number and where t the time at which the measurement was taken. Both phase and time are discrete, i.e. $\phi \in \{1, \dots, \Phi\}$ where $\Phi \in \mathbb{Z}_{>0}$ and $t \in \mathbb{Z}_{\geq 0}$. When using the three-phase substation voltage vector, $\mathbf{v}_{ss}(t)$ (where $(v_{ss,\phi}(t)) = \mathbf{v}_{ss}(t)$), with this cost function, any drop in transformer voltage results in a positive cost.

$$\zeta_{\text{voltage}}(\mathbf{v}(t)) := \sum_{\phi=1}^{\Phi} \begin{cases} \zeta_h(v_\phi(t)) & \text{if } V_{ss} \leq v_\phi \\ \zeta_l(v_\phi(t)) & \text{otherwise} \end{cases} \quad (3.1)$$

where $\Phi \in \mathbb{Z}_{>0}$

In this voltage cost function, Φ represents the number of phases (i.e. $\Phi = 3$), and $\zeta_h(v)$ and $\zeta_l(v)$ are two functions that convert a single voltage value, i.e. v_ϕ , into

a normalised positive cost based upon the direction of voltage deviation. High and low voltage thresholds, respectively V_h and V_l , are introduced in order to define these two functions. When choosing these two thresholds, then they must also satisfy the following inequality:

$$V_l < V_{ss} < V_h \quad (3.2)$$

For the work presented here, these two thresholds are based on the UK's nominal LV voltage range of +10% -6% around V_n , i.e. 230V P2N. As a result, the following upper and lower threshold functions are defined, in order to form a continuously differentiable cost function with a single zero tangent.

$$\zeta_h(v) := \left| \frac{v - V_{ss}}{V_h - V_{ss}} \right|^2 \quad (3.3)$$

$$\zeta_l(v) := \left| \frac{V_{ss} - v}{V_{ss} - V_l} \right|^2 \quad (3.4)$$

Substations may boost the voltage above the nominal LV voltage level, since voltage levels drop continuously along a purely consumptive feeder. The impact on the cost function $\zeta_{\text{voltage}}(\mathbf{v})$ when V_{ss} is boosted is shown in Figure 3.1 (for simplicity the a single-phase voltage vector is shown, i.e. $\Phi = 1$).

In this figure, it can be seen that $\zeta_{\text{voltage}}(\mathbf{v})$ at the thresholds V_l and V_h equates to one, and to zero at the set substation voltage, even when this voltage is boosted. This intentional feature is demonstrated by raising V_{ss} from V_n by +4% and +8%. At the ESMU's Point of Common Coupling (PCC), the device has access to all three phases of the feeder. One can assume that the line voltage along a purely consumptive feeder will drop continuously. Reasons behind this voltage drop are the resistive and inductive losses in the distribution lines, which are amplified with proximity to the substation, due to aggregated load currents from "down stream" customers. Under

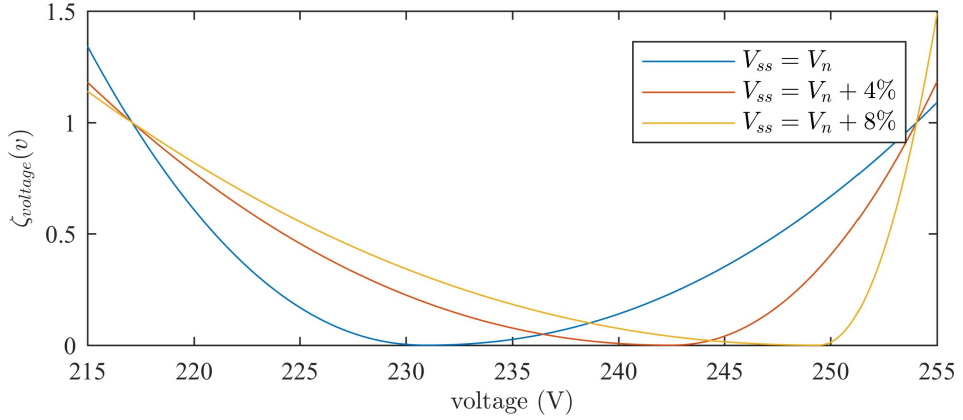


Figure 3.1: Cost function values for different substation voltages

heavy load conditions, this voltage is likely drop below the statutory operation limit. Since this limit is an operational constraint for DNOs, it must not be violated.

To mitigate this voltage drop, power is injected into the feeder at the ESMU's PCC. Doing so increases the voltage at its PCC and surrounding nodes, since the portion of load current that would normally be supplied by the substation is now delivered by the ESMU. This effect when injecting power is sketched in the Figure 3.2 below.

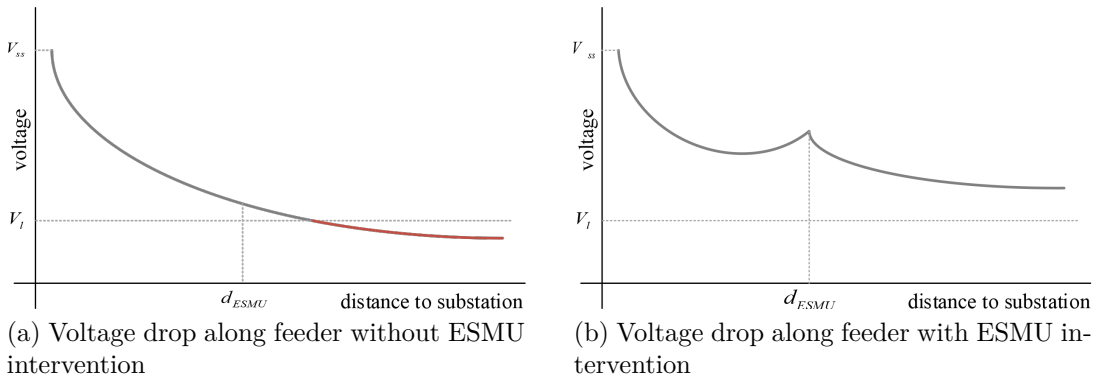


Figure 3.2: Sketch of the benefits that occur when ESMU injects power into the feeder in order to mitigate the voltage drop along the cable

In this figure, the expected voltage drop along the entire feeder is sketched. It can be seen how the voltage of the feeder's tailing section can potentially drop below V_l , but ESMU's intervention can alleviate some load and bring voltages back within

operational bounds. The three-phase ESMU voltage, $\mathbf{v}_{ESMU}(t)$ (where $(v_{ESMU,\phi}(t)) = \mathbf{v}_{ESMU}(t)$) is seen as a realistic key network parameter, which is also used in combination with a cost function. In fact, $\mathbf{v}_{ESMU}(t)$ is used with cost function, $\zeta_{\text{voltage}}(\mathbf{v}(t))$, which was defined in Equation 3.1. This is the same cost function that was used to assess the deviation in transformer voltage. Therefore, the resulting cost can be formulated as $\zeta_{\text{voltage}}(\mathbf{v}_{ESMU}(t))$. The Electricity Safety, Quality and Continuity Regulations (ESQCR) define the statutory voltage range at UK electricity customers. However, monitoring those voltages to assure they lie within limits is unfeasible, which is why they are unknown in reality. Nonetheless, in simulations all load voltages can easily be extracted, and since ESMU can impact all voltage levels to some degree, they are treated as theoretical key network parameters.

To illustrate this load voltage drop, a snapshot OpenDSS simulation was run on the used network model with all load consuming 8kW of power*. Figure 3.3 then shows all load bus voltages against their distances to the substation.

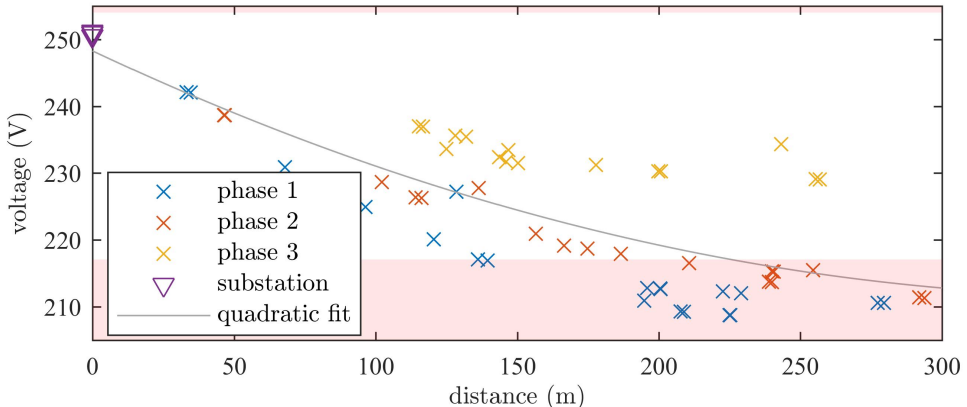


Figure 3.3: Voltage at the loads in the IEEE LV Test Case network for a total load of 440kVA against distance between the corresponding load and substation: for the quadratic fit $R^2 = 58.76\%$

In this figure, two observations can be made.

*Whilst historic and recent loads may reach values of this magnitude quite infrequently, future customer demand with the aggregated effect home-charging of EVs is expected to yield extreme scenarios like this.

1. It can be seen that phases are significantly unbalanced.
2. Customers further than 200m from the substation are likely to experience low-voltage events.

Although ESMU can reduce the number of such low-voltage events, including a cost for each load would add significant difficulty to the minimisation problem. Therefore, to solve this problem more efficiently, the previously defined voltage cost function (i.e. Equation 3.1) is expanded to only return a single value from all customer voltages. More specifically, only the cost deviation is used. By reducing this number to the worst case, any implemented solver only focuses on the edges of the problem. This focus is of particular importance, especially if the impact of the ESMU on some customer voltages is comparatively low. An aggregated voltage deviation cost would potentially obfuscate this impact and prevent the solver from effectively targeting the worst cases. Therefore, the customer (or load) voltage is defined as $\mathbf{v}_{\text{load}}(t)$, where $(v_{\text{load},i,\phi}(t)) = \mathbf{v}_{\text{load}}(t)$, and used in the new cost function, $\zeta_{\text{load voltage}}(\mathbf{v}_{\text{load}}(t))$, which is defined as:

$$\zeta_{\text{load voltage}}(\mathbf{v}(t)) := \max_{i,\phi} \zeta_{\text{voltage}}(v_{i,p}(t)) \quad (3.5)$$

where $i \in \{1, \dots, I\}$ and $\phi \in \{1, \dots, \Phi\}$ and $I \in \mathbb{Z}_{>0}$ and $\Phi \in \mathbb{Z}_{>0}$

Here, i represents the customer number out of a total customer count I , and ϕ represents the phase, out of the phase count Φ , to which the customer is connected.

3.2.2 Power related cost functions

Beside meeting voltage constraints, DNOs need to assure that their distribution networks operates both in an efficient and hence ideal manner. How ideal a three-phase network operates is indicated by its phase unbalance. This disturbance due to unbal-

anced phase load may not have an immediate impact, but negative long term effects (e.g. asymmetric load on transformers, rotating machines and increased neutral current) do weaken network assets and cannot be neglected. The way UK customers are connected to the feeder increases the problem of phase unbalance even more, because the single phase allocation is performed arbitrarily. Randomly assigning customers' phases was intended to distribute load evenly across all three phases, which in theory should balance the three-phase network load. In reality however this is not the case. Even in the unlikely case where the number of customers per phase is the same, the probability that all their loads match is very low. Therefore, the likeliness that LV distribution feeders in the UK are unbalanced is very high.

Substation monitoring is capable of providing reliable three-phase power measurements. Hence, they can be used as realistic key network parameters to determine the network's phase unbalance. The American National Standards Institute's (ANSI) definition of Unbalance Factor (UF) is used to calculate the phase unbalance [56]:

$$\text{UF}(\mathbf{x}) := \frac{\max_n |\bar{\mathbf{x}} - x_n|}{\bar{\mathbf{x}}} \quad \text{where } (x_n) = \mathbf{x} \quad (3.6)$$

and $n \in \mathbb{Z}_{>0}$

Here, \mathbf{x} can be an arbitrary vector, consisting of scalar values x_n (e.g. x_n may be voltage, current or power measurement per phase n). In this context, x_n is chosen to be the power flow into one of the network's phases. For clarity, the notation of $\bar{\mathbf{x}}$ is used to define the mean of the given vector, i.e.:

$$\bar{\mathbf{x}} := \frac{1}{N} \sum_{n=1}^N x_n \quad (3.7)$$

Substituting the three-phase substation power vector, $\mathbf{s}_{ss}(t)$ (where $(s_{ss,\phi}) = \mathbf{s}_{ss}$), for \mathbf{x} , allows the formulation of another cost, i.e. the "unbalance" cost, $\zeta_{\text{unbalance}}(\mathbf{s}_{ss}(t))$,

which is defined as:

$$\begin{aligned}
\zeta_{\text{unbalance}}(\mathbf{s}(t)) &:= \text{UF}(\mathbf{s}(t)) - 1 \\
&= \frac{\max_{\phi} |\overline{\mathbf{s}(t)} - s_{\phi}(t)|}{\overline{\mathbf{s}(t)}} - 1 \\
&= \frac{\max_{\phi} \left| \left(\frac{1}{\Phi} \sum_{\phi}^{\Phi} s_{\phi}(t) \right) - s_{\phi}(t) \right|}{\frac{1}{\Phi} \sum_{\phi}^{\Phi} s_{\phi}(t)} - 1
\end{aligned} \tag{3.8}$$

where $\phi \in \{1, \dots, \Phi\}$ and $\Phi \in \mathbb{Z}_{>0}$

Since the lowest value of $\text{UF}(\mathbf{x})$ is one, the corresponding cost function had to be adjusted in order to reach a minimum value of zero instead. A sample illustration, showing how this cost behaves as phase unbalance increases, is included in the Figure 3.4.

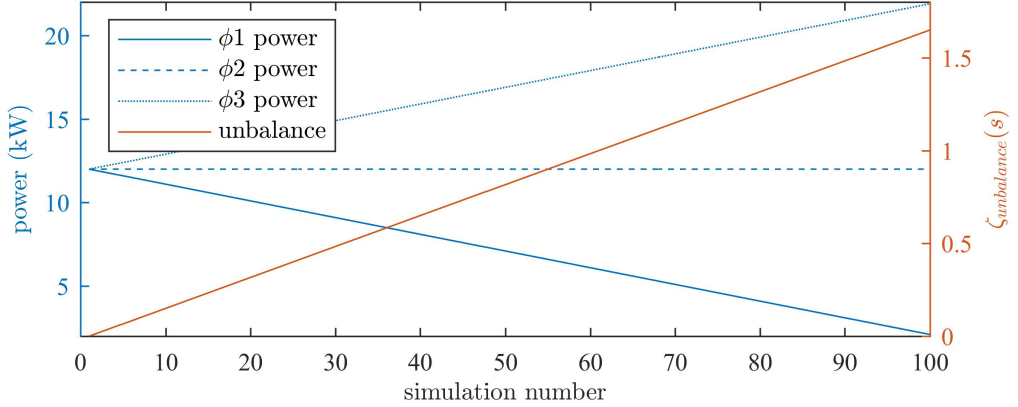


Figure 3.4: Sample network imbalance for different phase loadings as defined in ANSI/NEMA MG 1-2011

Here, it can be seen how $\zeta_{\text{unbalance}}(\mathbf{s}(t))$ rises with an increasing separation of the three-phase power values. Additionally, to assess the effective utilisation of the power distribution network, deviation from a unity Power Factor (PF) is also formulated as a cost. PF is the ratio between active (p) and apparent power (s), and gives an

indication of how much “good” power is being consumed by the system*. Experts would agree that keeping PF of a system close to unity indicates that it only requires active power to operate, which implies that uses the lowest possible amount of power transmission resources. In order to indicate the proximity to unity PF, a corresponding cost, $\zeta_{\text{PF}}(\mathbf{s}_{ss}(t))$, is used, which is defined as:

$$\zeta_{\text{PF}}(\mathbf{s}(t)) := \Phi - \sum_{\phi=1}^{\Phi} \frac{\text{Re}(s_{\phi}(t))}{|s_{\phi}(t)|} \text{ where } (s_{\phi}(t)) = \mathbf{s}(t) \text{ and } \Phi \in \mathbb{Z}_{>0} \quad (3.9)$$

Any deviation from a unity PF per phase increases the associated cost, whilst achieving a perfect PF for each phase results in a total cost of zero. In perfectly balanced systems that operate at unity PF, all three phases are 120° out of phase, and the sum of their instantaneous powers should equate to zero. This zero-sum also indicates, that no neutral current is flowing in the system. However, in an unbalanced system that operates at non-unity PF, the power transmitted through the neutral conductor can significantly deviate from zero. The negative impact of transmitting power through the neutral conductor is further amplified, since typical power distribution cables often use neutral conductors with significantly smaller cross-section areas than those used as line conductors. Results of any such additional power flow in the neutral conductor are further deviation of neutral voltages from ground, increased losses, and quicker exhaustion of the neutral conductor’s power carrying capability (making the system become more prone to failures). To address this last point, a “neutral load” cost, $\zeta_{\text{neutral load}}(\mathbf{s}_{ss}(t))$, is defined:

$$\zeta_{\text{neutral load}}(\mathbf{s}(t)) := \left| \sum_{\phi=1}^{\Phi} s_{\phi}(t) e^{\frac{j2\phi\pi}{\Phi}} \right| \text{ where } (s_{\phi}(t)) = \mathbf{s}(t) \text{ and } \Phi \in \mathbb{Z}_{>0} \quad (3.10)$$

*Reactive power is used to maintain magnetic fields in rotating machines, yet this can be supplied by local reactive power compensators and thus need not occupy otherwise free power transmission resources.

In this cost function, for a three-phase scenario, each single-phase power, $s_{ss,\phi}(t)$, is therefore rotated by an integer multiple of 120° in the complex plane, before adding them in order to obtain the neutral load vector. It is the magnitude of this apparent power vector is computed, which is then used as the resultant cost. Power losses have already been mentioned. In comparison to the losses of the entire electricity grid, losses in a LV distribution network are negligibly small. Nonetheless, the aggregate effect of reducing those losses could have a noticeable impact on both network efficiency and maximising profit margins (after all, nobody pays for undelivered energy). For example, in the high load scenario that was simulated in in Section 3.2.1, distribution losses were calculated as 58kW. This equates to 12% of the total network power (i.e. $\frac{s_{losses}(t)}{\sum_{\phi=1}^{\Phi} s_{ss,\phi}(t)} \approx \frac{58kW}{484kW}$), however, losses would be noticeably lower during normal network operation, e.g. a maximum of 5%. The rising proportion of losses, as uniform network load is continuously increased, is shown in Figure 3.5.

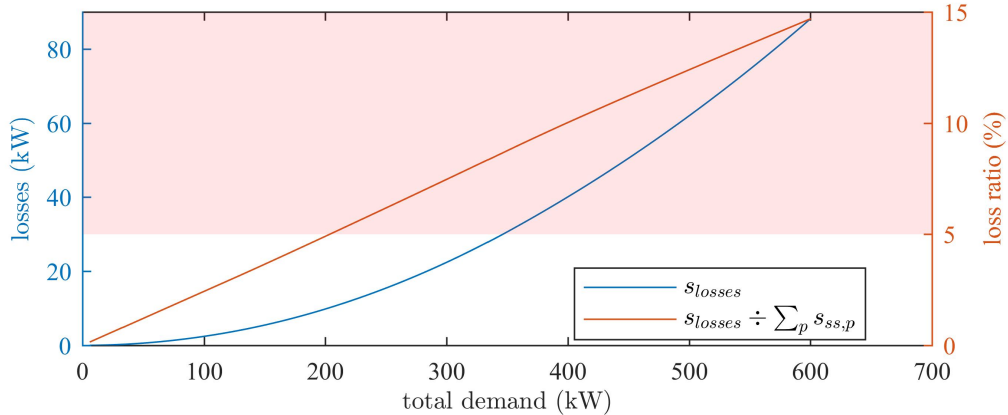


Figure 3.5: Losses against increasing power demand

In Figure 3.5, the region where losses exceed 5% of the total network power is highlighted in red. Whilst these losses are easily obtained from power flow simulations, in reality, distribution losses cannot be determined with such ease. Therefore, the network losses, $s_{losses}(t)$, are seen as theoretical key network parameters and they are used in the final power related cost, $\zeta_{losses}(s(t))$, which is defined as follows:

$$\zeta_{\text{losses}}(s(t)) := |s(t)| \quad (3.11)$$

3.2.3 Current related cost functions

Having addressed voltage deviation and inefficient network operation, physical network limits have not yet been taken into account: i.e. the current carrying capabilities of the cables. Heat, i.e. losses that are caused by the line's impedance, deteriorates the cable over time. Therefore, cables have an assigned thermal rating which should not be exceeded in order to minimise permanent cable damage and mitigate possible network failure. At substation level, to prevent over-currents, fuses or reclosers are installed that will disconnect the network under fault or high current conditions. To quantify whether the substation fuse is approaching its tripping point, its nominal fuse rating, I_{fuse} , is used. For the context of this work, I_{fuse} , is a static value which must not be exceeded. Using the three-phase current vector, $\mathbf{i}_{ss}(t)$ (obtained via substation monitoring, where $(i_{ss,\phi}(t)) = \mathbf{i}_{ss}(t)$) a cost, $\zeta_{\text{fuse utilisation}}(\mathbf{i}_{ss}(t))$, is formulated, and defined as follows:

$$\zeta_{\text{fuse utilisation}}(\mathbf{i}(t)) := \left| \frac{\sum_{\phi=1}^{\Phi} i_{\phi}(t)}{I_{\text{fuse}}} \right|^2 \text{ where } \phi \in \{1, \dots, \Phi\} \text{ and } \Phi \in \mathbb{Z}_{>0} \quad (3.12)$$

In the Figure 3.6, a plot has been included to illustrate how this quadratic cost behaves as substation current increases. For this simple case, the substation line rating was set as $i_{\text{fuse}} = 400\text{A}$, and the total substation current is the sum of all three phase currents. The red area indicates the region where current exceeds the fuse's nominal rating.

In addition to the currents flowing through the substation's fuse, currents flowing through all lines in the network may also be considered. Just like voltage levels at each

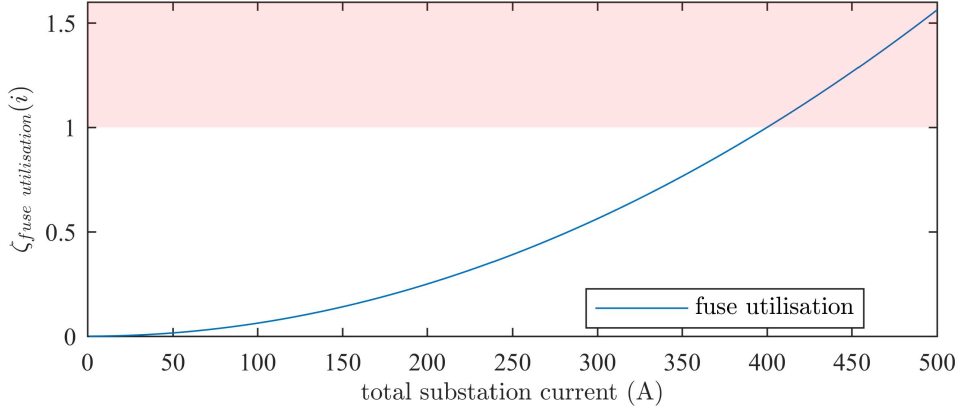


Figure 3.6: Cost of line or fuse utilisation against network current

customer, line currents are also seen as theoretical key network parameters, since they cannot easily be obtained. Generally, as the distance to the substation increases fewer “down stream” customers are connected to a radially expanding feeder, and therefore cables can be scaled down, i.e. to save cost. However with the expected uptake of LCTs, feeders are expected to deliver increasingly larger currents throughout all lines. For smaller lines at the network edge, these currents may increase to a magnitude larger than their nominal ratings. Therefore, the fuse current cost is expanded to take into account all line currents, $i_{\text{line},l,\phi}(t)$, and their nominal ratings, $I_{\text{nom},l}$. Here l represents the line number and ϕ the phase of that line. Collecting them in $\mathbf{i}_{\text{line}}(t)$ (where $(i_{\text{line},l,\phi}(t)) = \mathbf{i}_{\text{line}}(t)$) allows the formulation of an extended line utilisation cost, $\zeta_{\text{line utilisation}}(\mathbf{i}_{\text{line}}(t))$, which is defined as follows:

$$\zeta_{\text{line utilisation}}(\mathbf{i}(t)) := \max_l \left| \frac{\sum_{\phi=1}^P i_{l,\phi}(t)}{I_{\text{nom},l}} \right|^2 \quad (3.13)$$

where $l \in \{1, \dots, L\}$ and $\phi \in \{1, \dots, \Phi\}$ and $L \in \mathbb{Z}_{>0}$ and $\Phi \in \mathbb{Z}_{>0}$

Similar to Equation 3.5, this cost function only considers the maximum line utilisation in order to reduce computational burden without decreasing any parameter sensitivity.

3.3 Data, models and storage scheduling

In this section the used power data is presented first. Then the network model, from which all aforementioned key network parameters are extracted, and the battery model are explained. In the end, the scheduling procedure is detailed.

3.3.1 Load profiles

Alongside the LV Test Case model, the IEEE published 100 minutely demand profiles; each profile lasting 24h. Therefore, by assigning one load profile to each customer, a series of 1440 snapshot simulations could be run in OpenDSS in order to simulate the variation and volatility in demand over the entire day. A standardised power factor of 0.95 was used for all loads to calculate their reactive component. The apparent network power, $s_{\text{net}}(t)$, is therefore defined for each time-step, t , as the aggregate of all load apparent powers, $\mathbf{s}_{\text{load}}(t)$:

$$s_{\text{net}}(t) := \sum_{i=1}^I s_{\text{load},i}(t) \text{ where } I \in \mathbb{Z}_{\geq 0} \quad (3.14)$$

This demand profile does not take into account the distribution losses. Nonetheless, it functions as a simple time-series to schedule ESMU operation, which is detailed in Section 3.3.4.

3.3.2 Network model

The IEEE Power and Energy Society (IEEE-PES) provides several multi-node test cases. These test cases used to be limited to distribution networks in the United States. In 2015 however, they published a standardised model of a LV distribution network for the UK power network. This model is called the “European Low Voltage Test Feeder” [57]. Within the context of this work, this feeder is referred to as the “LV Test Case” and a network plot of this feeder has been included for reference.

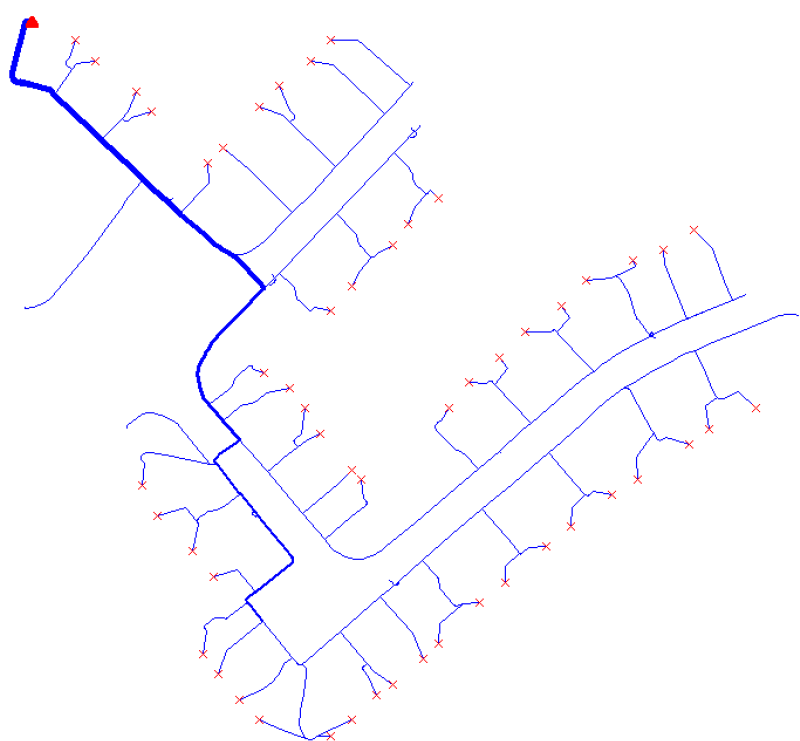


Figure 3.7: A power flow plot of the IEEE-PES European Test Case Feeder, i.e. a LV distribution network in the UK.

A substation (triangle in north west) provides power to the feeder, and the power magnitude is visualised by the thickness of the feeder's lines. In total, there are 55 single-phase households connected to the substation, which represents a medium-sized, unbalanced UK feeder.

3.3.3 Battery model

The ESMU systems that were deployed throughout the NTVV project consisted of two parts: the Power Management Unit (PMU) and the Energy Storage Unit (ESU). The PMU controls three-phase powers and links the ESU to the grid. Each PMU's single-phase power rating, S_{rating} , is 12kVA and can also perform filtering functions beside battery charging and discharging, e.g. compensating for harmonic distortion, reactive power and phase unbalance. The ESU is a modular container of 12.5kWh of Li-Ion energy storage that can be aggregated to increase the total energy storage capacity. All battery monitoring, conditioning and regulation is performed within the ESU and hence lies outside the scope of this work. However, control instructions that are sent to the ESMU system should not request the device to operate outside its own specifications, i.e. avoid under- or over-charge.

In order to simulate this ESMU system and its energy storing behaviour, a model is developed from the given device specifications. This model includes an charge-discharge efficiency, η , and standby losses, μ . η is related to the efficiency of the PMU's power converters, which are quoted to have a round trip efficiency of 98%, i.e. $\eta = 0.98$. μ on the other hand is linked to the nominal power drawn by the battery's control system as well as the battery's self-discharge rate. With the charge-discharge efficiency, η , the battery charge-discharge power, $p_{\text{bat}}(t)$, can be calculated for any given ESMU power, $\mathbf{s}_{\text{ESMU}}(t)$ (where $(s_{\text{ESMU},\phi}(t)) = \mathbf{s}_{\text{ESMU}}(t)$).

$$p_{\text{bat}}(t) := \begin{cases} \eta \operatorname{Re} \left\{ \sum_{\phi=1}^{\Phi} s_{\text{ESMU},\phi}(t) \right\} & \text{if } \operatorname{Re} \left\{ \sum_{\phi=1}^{\Phi} s_{\text{ESMU},\phi}(t) \right\} \geq 0 \\ \frac{1}{\eta} \operatorname{Re} \left\{ \sum_{\phi=1}^{\Phi} s_{\text{ESMU},\phi}(t) \right\} & \text{otherwise} \end{cases} \quad (3.15)$$

where $\phi \in \{1, \dots, \Phi\}$ and $\Phi \in \mathbb{Z}_{>0}$

Although the ESMU's PSU rating, S_{rating} , may allow for a maximum power consumption of 36kVA (i.e. $= 3 \times 12\text{kVA}$), the charging power is internally limited, by a charging factor, C_f . This factor is the ratio between the battery's maximum discharge power and its total capacity (i.e. $\max_t(p_{\text{bat}}(t)) \leq C_f \cdot C_{\text{bat}}$). In accordance to the ESMU's specification, C_f was fixed as 1.6. With those restrictions in mind, a charge-discharge power can be applied to charge or discharge the battery. Assuming that this power remains constant during a predefined sample period, Δt , then the change in stored energy can be defined as follows.

$$\Delta E_{\text{bat}}(t) = p_{\text{bat}}(t)\Delta t \quad (3.16)$$

The battery's dynamics can therefore be modelled as the change in energy level from time t to time $t + \Delta t$. Taking into account the standby losses, μ , the next energy level $E_{\text{bat}}(t + \Delta t)$ is defined as:

$$E_{\text{bat}}(t + \Delta t) := \mu (\Delta E_{\text{bat}}(t) + E_{\text{bat}}(t)) \quad (3.17)$$

In an ideal case, $\mu = 1$, where no energy would be lost in the storage system. However, to model energy storage dynamics, it became common practice to assess the energy storage's charge level as the State of Charge (SOC) instead of using the actual charge stored. This SOC is defined as the actual energy stored in the ESU, $E_{\text{bat}}(t)$, divided by the total capacity of the system, C_{bat} . i.e.:

$$SOC(t) := \frac{E_{\text{bat}}(t)}{C_{\text{bat}}} \quad (3.18)$$

Similar to the energy dynamics, the SOC dynamics can therefore be defined as:

$$SOC(t + \Delta t) := \mu \left(\frac{p_{\text{bat}}(t)\Delta t}{C_{\text{bat}}} + SOC(t) \right) \quad (3.19)$$

When summarising $\hat{s}_{\text{ESMU}}(t) = \text{Re} \left\{ \sum_{\phi=1}^{\Phi} s_{\text{ESMU},\phi}(t) \right\}$ and combining Equation 3.15 with Equation 3.19, then the battery model's full dynamics can be defined as:

$$SOC(t + \Delta t) := \begin{cases} \mu \left(\frac{\eta \hat{s}_{\text{ESMU}}(t)\Delta t}{C_{\text{bat}}} + SOC(t) \right) & \text{if } \hat{s}_{\text{ESMU}}(t) \geq 0 \\ \mu \left(\frac{\hat{s}_{\text{ESMU}}(t)\Delta t}{\eta C_{\text{bat}}} + SOC(t) \right) & \text{otherwise} \end{cases} \quad \forall t \quad (3.20)$$

A flowchart to visually represent the developed battery model, is included in Figure 3.8. In this figure, all green and blue fields indicate, respectively, model inputs and results. The white states represent operations applied onto those inputs and results and in the end yield the output, i.e. the yellow field.

3.3.4 ESMU scheduling

Computing the ESMU's daily schedule at the dataset's temporal resolution, i.e. sub-half-hourly, is ineffective and slow. Doing so is ineffective, because demand variability due to behavioural unpredictability makes forecasting at high temporal resolution unfeasible, and the large number of search parameters makes finding a solutions very computationally demanding. Therefore, forecasting and scheduling is generally performed at half-hourly temporal resolution. To obtain such a half-hourly profile, the sub-half-hourly profile had to be down-sampled and synchronised. This is done with the synchronisation function $k(t)$, which links the original sub-half-hourly demand to

[†]In the flowchart “charging” implies that $\hat{s}_{\text{ESMU}}(t) \geq 0$ as explained in Equation 3.15.

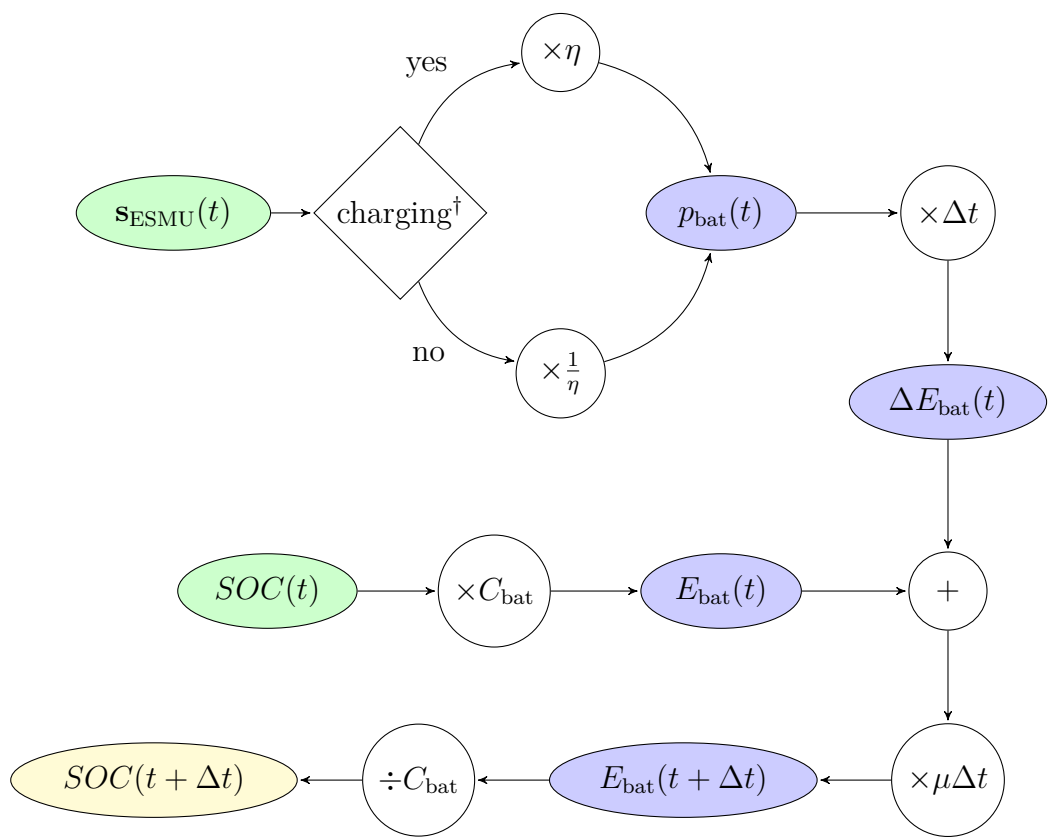


Figure 3.8: Flowchart to calculate the next SOC (i.e. $SOC(t + \Delta t)$) based on current ESMU power (i.e. $s_{ESMU}(t)$) and current SOC (i.e. $SOC(t)$)

a half-hourly time-series and is defined as follows:

$$k(t) := \left\lfloor \frac{t-1}{K\Delta t} \right\rfloor + 1 \quad (3.21)$$

Here, Δt is the sub-half-hourly sampling period of the simulation, and K is the duration of the half-hourly time-slot, i.e. number of sub-half-hourly periods within the half-hourly slot. It should be noted that the integer multiple of K has to equate to the scheduling horizon's length, T_{sch} ; i.e. $T_{\text{sch}} \stackrel{!}{=} \alpha K$ where $\alpha \in \mathbb{Z}_{>0}$. Otherwise, the sub-half-hourly profile cannot be divided into a set of equal length time-slots, where each time-slot is of length $K\Delta t$. Therefore, the resulting half-hourly network load, $s_{\text{net}}^*(t)$ (where $(s_{\text{net}}^*(t)) = \mathbf{s}_{\text{net}}^*$), is defined as follows:

$$s_{\text{net}}^*(t) = \frac{1}{K} \sum_{\tau=k(t)K}^{(k(t)+1)K-1} s_{\text{net}}(\tau) \text{ where } K \in \mathbb{Z}_{>0} \quad (3.22)$$

Now, over the period from $k(t)K$ to $(k(t) + 1)K - 1$, are power values are equal. To illustrate the difference between the original sub-half-hourly network load and the resulting half-hourly demand, both profiles are plotted in Figure 3.9. In this figure, it can be observed how the high variability and volatility in power is removed in the half-hourly profile. When generating ESMU schedules these variations are neglected and thus the unwanted peak power demands cannot be sufficiently compensated.

The main goals when scheduling battery operation are to achieve “valley-filling” and “peak-shaving” behaviour. As shown in the literature review in Chapter 2, the Peak-to-Average Ratio (PAR), the min-max-difference (MMD) and the power transients (TRA) are good indicators of such a behaviour. Therefore, three half-hourly costs regarding are used as, $\zeta_{\text{PAR}}(\mathbf{s}_{\text{ESMU}}^* + \mathbf{s}_{\text{net}}^*)$, $\zeta_{\text{MMD}}(\mathbf{s}_{\text{ESMU}}^* + \mathbf{s}_{\text{net}}^*)$, and $\zeta_{\text{TRA}}(\mathbf{s}_{\text{ESMU}}^* + \mathbf{s}_{\text{net}}^*)$ are defined as follows:

$$\zeta_{\text{PAR}}(\mathbf{s}) := \frac{\max_t |\mathbf{s}|}{\frac{1}{K} \sum_{t=1}^K s(t)} - 1 \text{ where } (s(t)) = \mathbf{s} \quad (3.23)$$

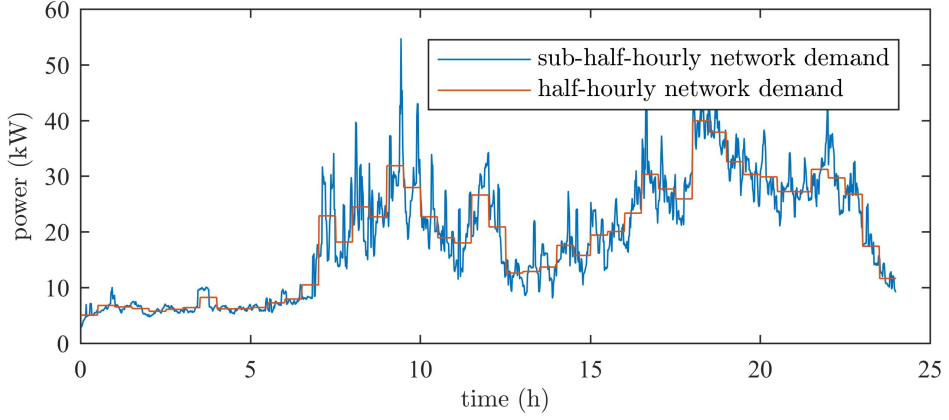


Figure 3.9: Highly variable and volatile demand profile vs half-hourly demand (i.e. a forecast under perfect foresight conditions)

$$\zeta_{\text{MMD}}(\mathbf{s}) := \frac{\max_k(\mathbf{s}) - \min_k(\mathbf{s})}{\frac{1}{K} \sum_{t=1}^K s(t)} \text{ where } (s(t)) = \mathbf{s} \quad (3.24)$$

$$\zeta_{\text{TRA}}(\mathbf{s}) := \max_t |s(t + \Delta t) - s(t)| \text{ where } (s(t)) = \mathbf{s} \quad (3.25)$$

All three costs functions assess the sum of the half-hourly ESMU schedule, $\mathbf{s}_{\text{ESMU}}^*$, and the half-hourly network load profile, $\mathbf{s}_{\text{net}}^*$. Combined with all underlying model constraints, the following minimisation problem is defined:

$$\begin{aligned} & \min_{\mathbf{s}_{\text{ESMU}}^*} \zeta_{\text{PAR}}(\mathbf{s}_{\text{ESMU}}^*, \mathbf{s}_{\text{net}}^*) + \zeta_{\text{MMD}}(\mathbf{s}_{\text{ESMU}}^*, \mathbf{s}_{\text{net}}^*) + \zeta_{\text{TRA}}(\mathbf{s}_{\text{ESMU}}^*, \mathbf{s}_{\text{net}}^*) \\ & \text{s.t. } \begin{cases} p_{\text{bat}}(t) \leq C_f \times C_{\text{bat}} \forall t \\ |s_{\text{ESMU},\phi}(t)| \leq S_{\text{rating}} \forall \phi \forall k \\ 0 \leq SOC(t) \leq 1 \forall t \end{cases} \end{aligned} \quad (3.26)$$

For this piece of work, a Sequential Quadratic Programming (SQP) approach was chosen to solve this minimisation problem. The resulting half-hourly ESMU power, $\mathbf{s}_{\text{ESMU}}^*$, could then be extrapolated using the same synchronisation function, $k(t)$, to

yield a sub-half-hourly ESMU schedule.

For the work presented in this chapter, the supplied half-hourly network load (or forecast) was obtained from sub-half-hourly data. Treating it as a forecast with perfect foresight does not skew the already imperfect schedule performance, which is obtained when applying the resulting half-hourly schedule to sub-half-hourly load. Figure 3.10 shows a sample day, where the impact of this half-hourly ESMU schedule becomes apparent.

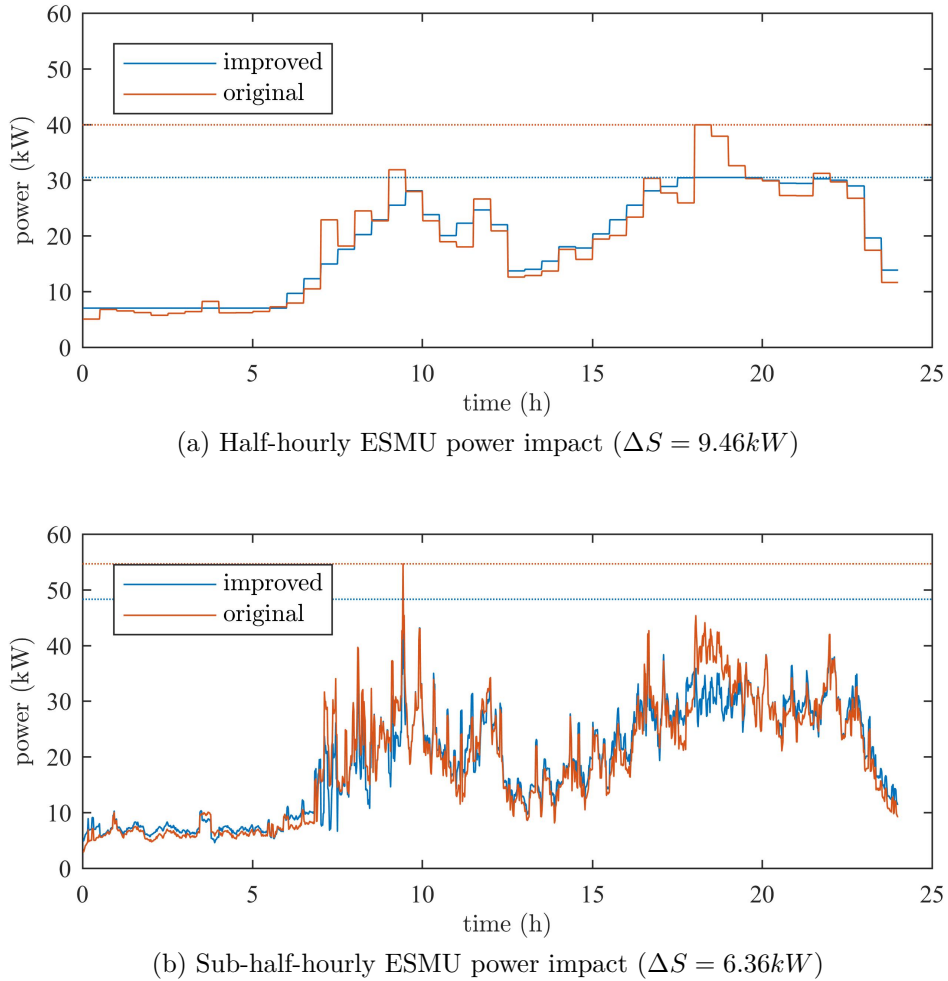


Figure 3.10: Impact of half-hourly ESMU schedule on sub-half-hourly power profile

This figure shows the positive impact on the half-hourly profile (i.e. in Figure 3.10a), which is particularly dominant during the evening peak load. However, the impact on the actual sub-half-hourly demand (i.e. in Figure 3.10b) has a much

larger demand spike during the morning hours, which is not that strongly addressed. When compared, the ideal peak power shaving dropped from 9.46kW to only 6.36kW. Nonetheless, the overall improvement yielded by the ESMU schedule can still be noticed. The method of how to adjust the ESMU's phase powers to mitigate the impact of such volatile load spikes is addressed in the following section.

3.4 Optimisation method

In the previous sections, the key network parameters and associated cost functions have been established, and the data, models and schedule generation is explained. The key network parameters that are used in this work are:

- substation phase voltages, $(v_{ss,\phi}(t)) = \mathbf{v}_{ss}(t)$,
- ESMU phase voltages, $(v_{ESMU,\phi}(t)) = \mathbf{v}_{ESMU}(t)$,
- all load voltages, $(v_{load,i}(t)) = \mathbf{v}_{load}(t)$,
- substation apparent phase power, $(s_{ss,\phi}(t)) = \mathbf{s}_{ss}(t)$,
- substation phase currents, $(i_{ss,\phi}(t)) = \mathbf{i}_{ss}(t)$,
- all line currents, $(i_{line,l,\phi}(t)) = \mathbf{i}_{line}(t)$, and
- all network losses, $s_{losses}(t)$.

In this section, the method of adjusting the predetermined ESMU schedule on a sub-half-hourly basis is presented. This method is designed to improve network performance, which in turn is indicated by the aforementioned key network parameters. After detailing the method itself, the generation and assessment of all results are explained.

3.4.1 Closed-loop schedule adjustment

To summarise all costs, that are derived from the key network parameters, a global cost is generated and formalised as follows:

$$\begin{aligned}
 \zeta(\mathbf{v}_{ss}(t), \mathbf{v}_{ESMU}(t), \mathbf{v}_{load}(t), \mathbf{s}_{ss}(t), \mathbf{i}_{ss}(t), \mathbf{i}_{line}(t), s_{losses}(t), \boldsymbol{\alpha}) := \\
 \alpha_1 \sum_{\phi=1}^{\Phi} \zeta_{\text{voltage}}(v_{ss,\phi}(t)) + \alpha_2 \sum_{\phi=1}^{\Phi} \zeta_{\text{voltage}}(v_{ESMU,\phi}(t)) + \alpha_3 \zeta_{\text{load voltage}}(\mathbf{v}_{load}(t)) \\
 + \alpha_4 \zeta_{\text{unbalance}}(\mathbf{s}_{ss}(t)) + \alpha_5 \zeta_{\text{PF}}(\mathbf{s}_{ss}(t)) + \alpha_6 \zeta_{\text{neutral load}}(\mathbf{s}_{ss}(t)) \\
 + \alpha_7 \zeta_{\text{fuse utilisation}}(\mathbf{i}_{ss}(t)) + \alpha_8 \zeta_{\text{line utilisation}}(\mathbf{i}_{line}(t)) + \alpha_9 \zeta_{\text{losses}}(s_{losses}(t))
 \end{aligned}$$

where $\phi \in \{1, \dots, \Phi\}$ and $\Phi \in \mathbb{Z}_{>0}$ and $\boldsymbol{\alpha} = \{\alpha_1, \dots, \alpha_9\}$ (3.27)

Here, $\boldsymbol{\alpha}$ is a binary choice vector, with which the weight of the global cost function can easily be adjusted. In other words, this vector allows the global cost to target any specific key network improvement, which is based on a specific cost. To simplify the notation, and since all key network parameters are outputs of the power flow simulations and not directly adjustable, the global cost function is shortened to $\zeta(\boldsymbol{\alpha})$.

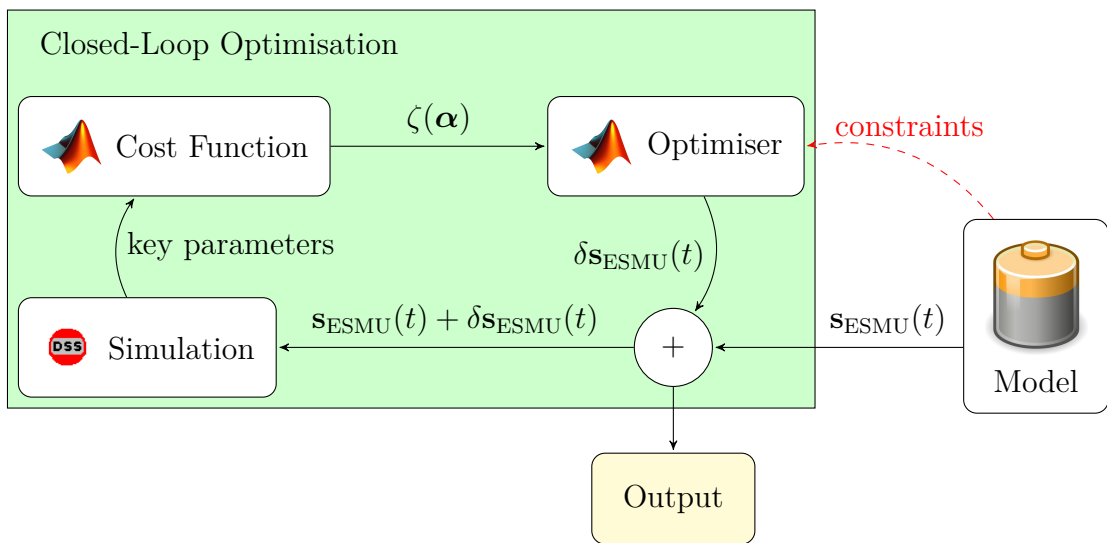


Figure 3.11: ESMU schedule adjustment flow diagram

The underlying method that performs the proposed closed-loop optimisation is shown in Figure 3.11. For each time-slot, t , the pre-scheduled ESMU power vector, $\mathbf{s}_{\text{ESMU}}(t)$, is extracted and adjusted by an offset vector, $\delta\mathbf{s}_{\text{ESMU}}(t)$. An optimal offset vector is found through iterative optimisation to minimise the global cost function, $\zeta(\boldsymbol{\alpha})$. This minimisation is achieved by repetitively running power flow simulations of the IEEE distribution feeder and adjusting $\delta\mathbf{s}_{\text{ESMU}}(t)$. Once the adjusted ESMU schedule (i.e. $\mathbf{s}_{\text{ESMU}}(t) + \delta\mathbf{s}_{\text{ESMU}}(t)$) has converged and a solution has been found, then the closed-loop optimisation process terminates and the simulation begins optimisation during the next time slot (i.e. $t + \Delta t$). Since $\delta\mathbf{s}_{\text{ESMU}}(t)$ must not impact the underlying half-hourly ESMU schedule, one more constraint is defined. This constraint assures that the sum of all phase powers in the adjustment vector equates to zero, hence keeping the internal battery's charging-discharge power the same. Including the previously mentioned battery system constraints, which ensure that the ESMU operates within its technical limitations, the minimisation problem for the closed-loop optimisation mechanism is formulated as follows:

$$\min_{\delta\mathbf{s}_{\text{ESMU}}(t)} \zeta(\boldsymbol{\alpha}) \text{ s.t.} \begin{cases} \sum_{\phi=1}^{\Phi} \text{Re}(s_{\text{ESMU},\phi}(t)) = 0 \\ p_{\text{bat}}(t) \leq C_f \times C_{\text{bat}} \\ |s_{\text{ESMU},\phi}(t)| \leq S_{\text{rating}} \forall \phi \\ 0 \leq SOC(t) \leq 1 \end{cases} \quad (3.28)$$

where $(s_{\text{ESMU},\phi}(t)) = \mathbf{s}_{\text{ESMU}}(t)$ and $\Phi \in \mathbb{Z}_{>0}$

3.4.2 Execution and result assessment procedure

After having established what parameters the global cost focuses on when trying to improve network operation, and after having established how the closed-loop optimising method aims to achieve these improvements, the performance assessment

procedure is introduced. The complete evaluation procedure and assessment is summarised in Figure 3.12.

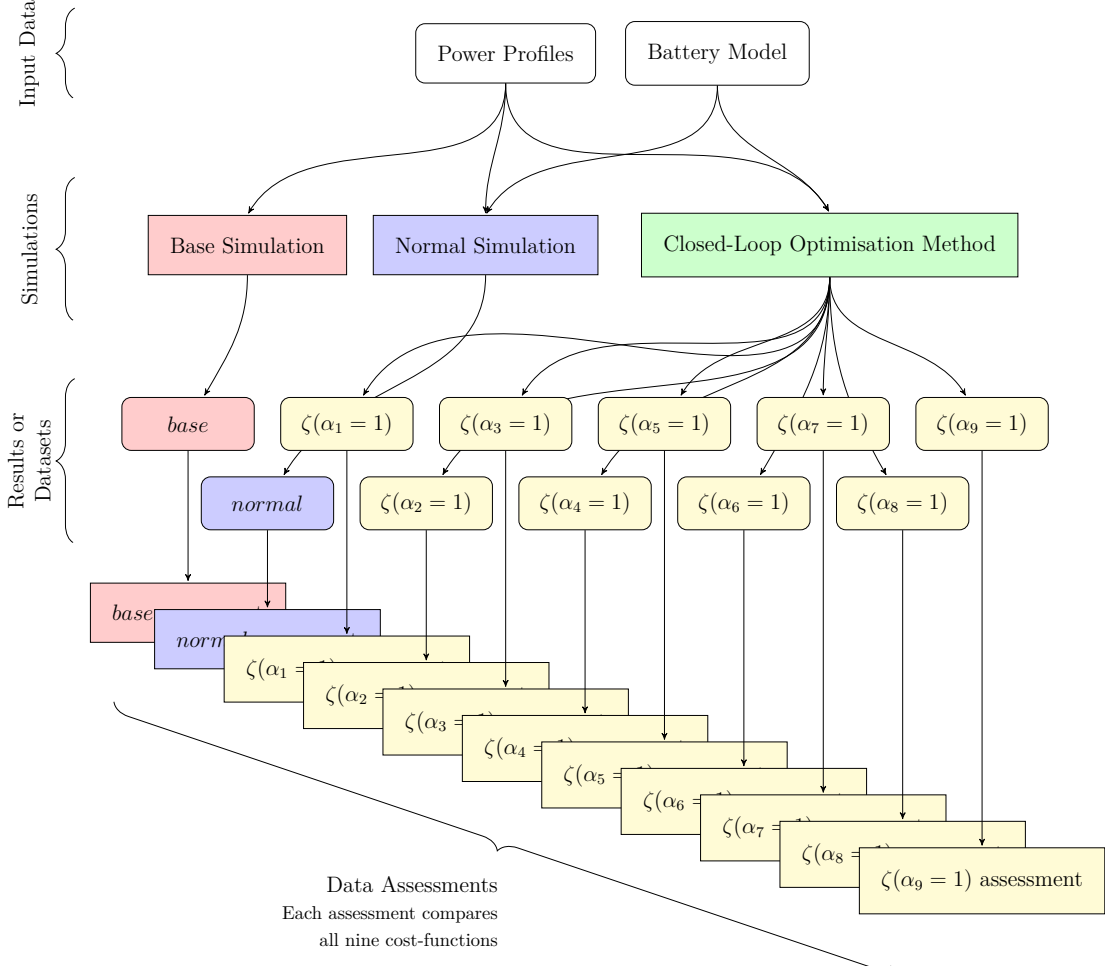


Figure 3.12: Method execution and results assessment flowchart

In total, there are eleven datasets of simulation results, which need to be assessed and compared. These results are obtained from a *base* simulation, a *normal* simulation and nine cost driven *optimisation* simulations. For the *base* simulation, the outcome is generated by applying just the daily power profiles without any ESMU intervention. Therefore, this case represents the baseline of network performance, which should be improved by any ESMU intervention. The *normal* simulation is the simplest of all ESMU interventions, since the ESMU executes its normal (or traditional) half-hourly schedule without any additional modifications. Comparing results from the

base and *normal* simulations does show the direct impact of the traditional ESMU operation on network performance. The remaining nine datasets are results of the nine different cost driven simulations, where the ESMU schedule is adjusted on a sub-half-hourly level for each simulation. This adjustment is designed to minimise one underlying cost-function, whilst conforming to the ESMU's overall half-hourly charging and discharging profile. In order to treat each cost-function separately α is set to focus on each cost independently, e.g. by setting $\alpha_1 = 1$ and $\alpha_2 = \alpha_3 = \dots = \alpha_9 = 0$. For simplicity, the flowchart in Figure 3.12 abbreviates the specific costs by only indicating which entry in the α vector is set to 1, e.g. $\zeta(\alpha_1 = 1)$.

Once all eleven simulations have completed, their corresponding datasets are assessed in an identical manner, so that their impact on network performance can be compared. This comparison is broken into three parts for all dataset:

1. **Time Series Analysis** - The underlying profiles are plotted and compared against their respective counterpart cases, in order to link the immediate network impacts to their physical meaning. For the same profiles, their corresponding cost profiles are calculated and plotted. This is done to highlight how the profiles are interpreted by the cost-functions in terms of improvement (i.e. lower cost) or worsening (i.e. increased cost).
2. **Difference Analysis** - The difference in cost profiles, compared to the respective *base* or *normal* case, is calculated and boxplots of these differences are presented to show a statistical spread of improvements or worsening. For these plots, a generally positive boxplot indicates a general improvement of the underlying network parameters, whilst a generally negative boxplot does indicate worse performance in regards to the underlying network parameters.
3. **Probability Density Analysis** - A set of Probability Density Functions (PDF) is derived for each cost profile using the well established kernel density estima-

tion. These PDFs indicate the probability that a certain cost value occurs. An improvement is noted when the PDF is shifted towards the lower cost values, whereas a shift towards higher cost values worsened the network performance.

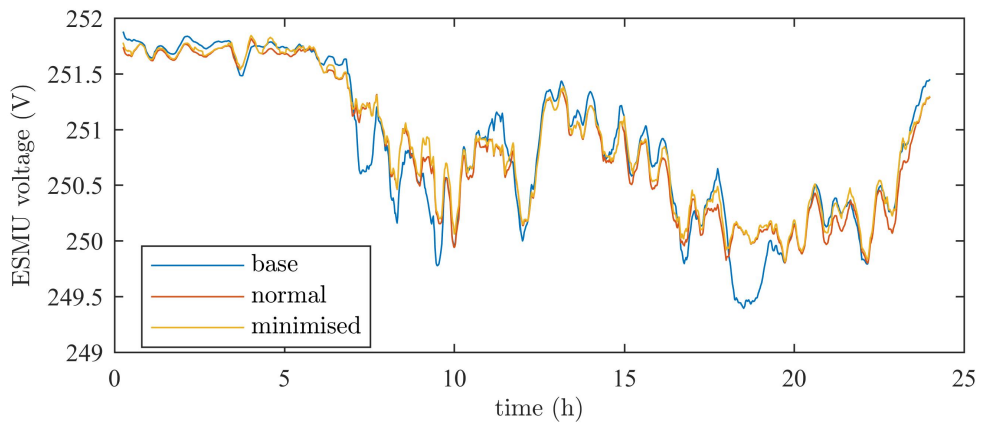
3.5 Results and Discussion

In this section, all results are presented and briefly discussed. Each of the three assessments in this section focuses on improvements in voltage level, improvements in network efficiency (i.e. power quality and network losses), and improvements in resource utilisation. Hence, only a subset of all results is included, but the complete set of results has been appended to this Thesis in Appendix A.1.

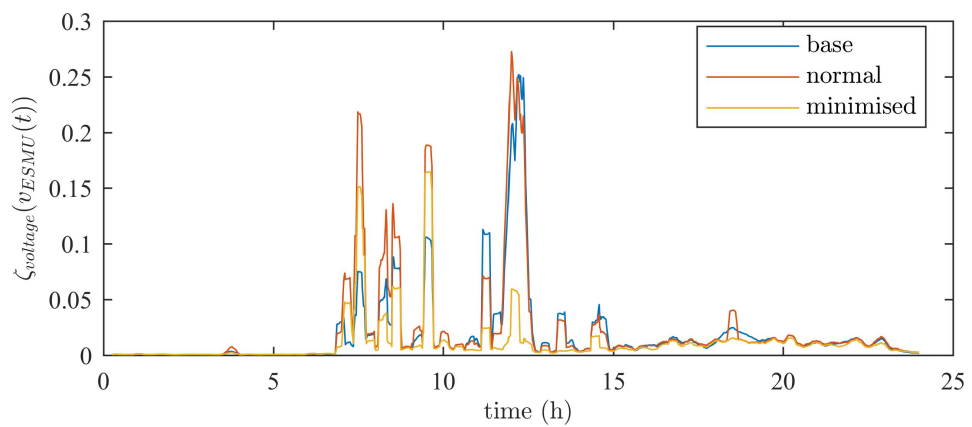
3.5.1 Time Series Analysis

The ESMU's largest impact on network voltage levels can be noticed at the ESMU's PCC. Consequently, any adjustments to the ESMU powers should become most noticeable, too. This impact can clearly be observed in Figure 3.13.

In this figure, the *base* and *normal* case's voltage profiles are plotted alongside the *minimisation* case, for which voltage deviation is minimised. The plot shows that during the night's light load (i.e. from 0:00 to 6:00), ESMU was able to boost its voltage towards the nominal feeder voltage. This is also the case during the lighter load in the afternoon (i.e. between 12:00-14:00). But during the rest of the day when network load increases, the ESMU is unable to reduce voltage deviation to match its PCC voltage with the network's nominal substation voltage. The reason behind this behaviour that the ESMU has allocated its resources to serve for the underlying half-hourly ESMU schedule. Therefore, the remaining resources that could provide voltage support during periods of low demand become limited during periods of high demand. Combined with the fact that the LV distribution networks are more resistive



(a) Voltage levels at ESMU's PCC when minimising its voltage deviation (nominal substation voltage included for reference)



(b) Cost associated with the minimisation of the ESMU's PCC voltage deviation

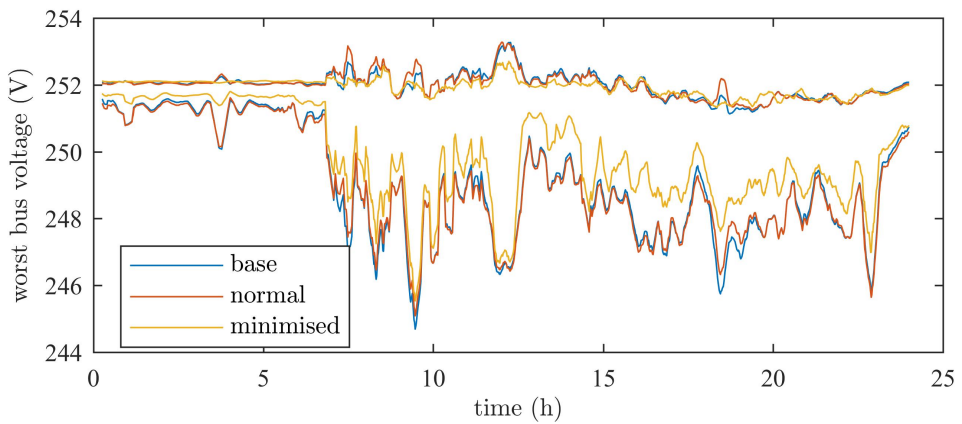
Figure 3.13: Voltage level modifications as noted at the ESMU's PCC by adjusting its schedule

than inductive (i.e. unlike HV transmission networks), adjusting only being able to adjust the ESMU's reactive powers to stabilise voltage levels, has an even smaller impact. Nonetheless, due to some continuous yet small availability of power resource, ESMU is able to boost voltages to some extent at all times. In Figure 3.13b, this can be seen since the associated cost has always been reduced in comparison to the *base* and *normal* cases.

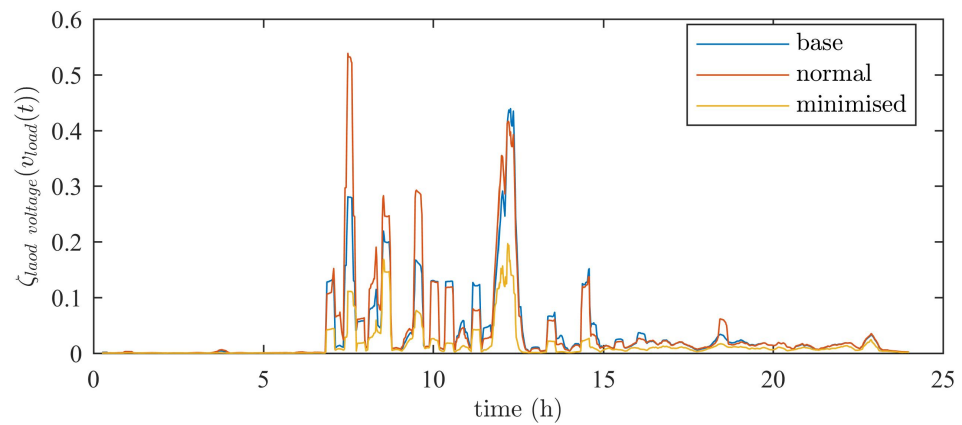
The ability to support voltage levels at the ESMU's PCC is interesting, yet supporting voltage levels at all buses throughout the network is more relevant since some of these buses are linked to customers, for which it is essential to maintain a constant voltage level. Therefore, the results assess both the highest and lowest voltage level that is recorded throughout the network.

In Figure 3.14a, despite no voltage violations taking place due to the already boosted substation voltage, the ESMU's positive impact can be observed. Here, the difference between highest and lowest voltage in the network is noticeably reduced at all times, and their average voltage is brought closer to a nominal voltage level. The ESMU's function to support the network in providing more stable voltage levels at customer endpoints is therefore met. This fact is also supported by the associated cost plot in Figure 3.14b, where a reduction in cost can be observed at all times.

Beside providing stable voltage levels, power quality should also be upheld to assure that distribution networks operate as efficient as possible. The first power related parameter that indicates network efficiency is phase unbalance. In Figure 3.15a, the power value of the highest and lowest loaded corresponding phases is plotted over time. At all times, the sub-half-hourly adjustments of the ESMU's schedule did reduce the underlying phase imbalance. This is achieved by redistributing power from the most loaded phase to the least loaded phases; hence utilising the unused capacity of the lighter loaded phases. As expected, the associated cost has been noticeably lowered in comparison to the *base* and *normal* cases. It should however be noted, that

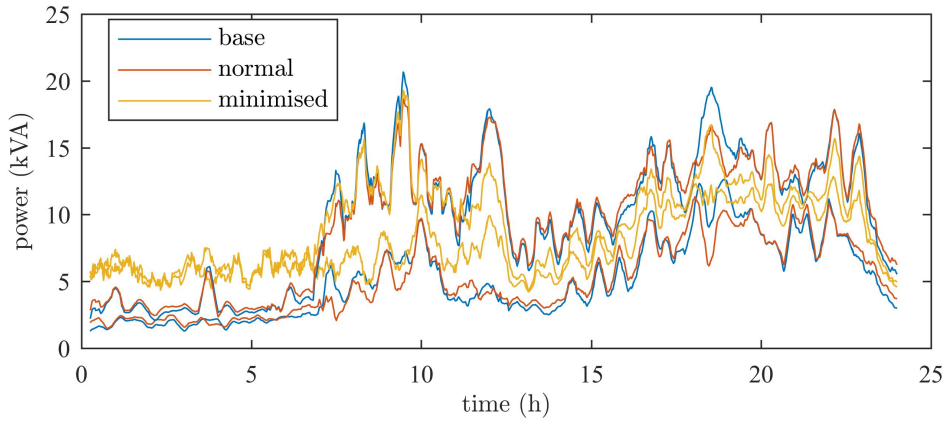


(a) Highest and lowest voltage levels that were recorded throughout the network when minimising the worst voltage deviation (nominal substation voltage included for reference)

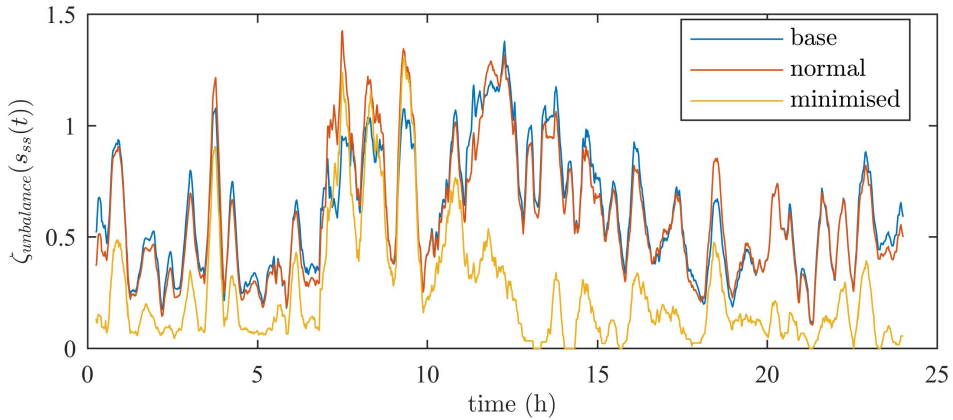


(b) Cost associated with the worst voltage deviation throughout the entire network

Figure 3.14: Voltage level improvements at all buses in the entire distribution network due to the ESMU schedule adjustment.



(a) Network's highest and lowest phase power demand when phase unbalance was minimised



(b) Cost associated with the network's phase unbalance

Figure 3.15: Reduction of the network's phase unbalance due to the adjustment of the ESMU schedule.

phase balancing during the morning hours is predominantly achieved by using reactive power injection and absorption. This can be seen by the similar yet increased phase loadings between 0:00 and 7:00. Therefore, the tradeoff between adding additional strain onto the network, versus balancing phases has to be taken into account. One such strain that is being put onto the network, is increased neutral power flow due to phasor misalignment.

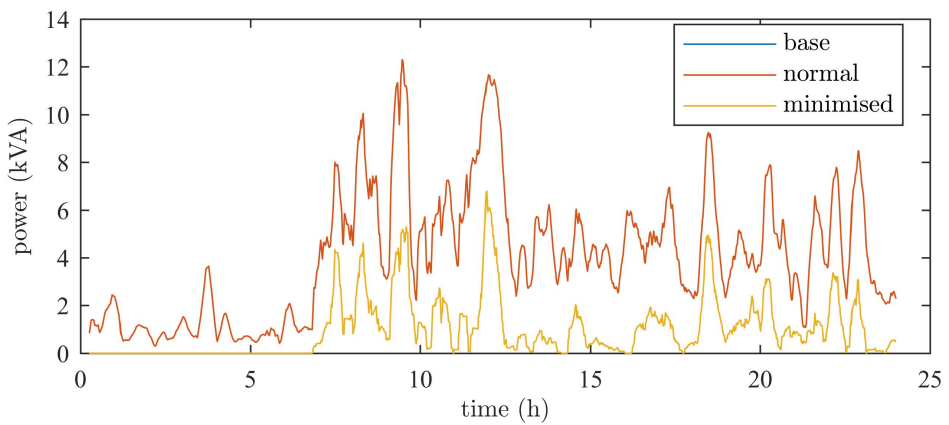


Figure 3.16: Neutral power reduction due to the ESMU schedule adjustments

For the results that are plotted in Figure 3.16, neutral power flow is minimised through the adjustment of ESMU powers. It can be seen, that for the *normal* case, neutral power is not affected at all. Reason for this result is the choice of evenly assigning the scheduled ESMU power to all three phases. Therefore, neither phase unbalance nor loading of the neutral conductor is being taken into account. For the *minimisation* case however, loading of the neutral conductor is successfully reduced in comparison to both the *normal* and *base* case.

Unlike neutral phase unbalance and neutral loading, power factor on the other hand is impacted just by introducing the half-hourly ESMU schedule, as shown in Figure 3.17. Whilst the choice of a static power factor for all loads in the *normal* case resulted in a constant power throughout the day, half-hourly ESMU intervention in the *base* case results in a noticeable power factor variation. This variation is

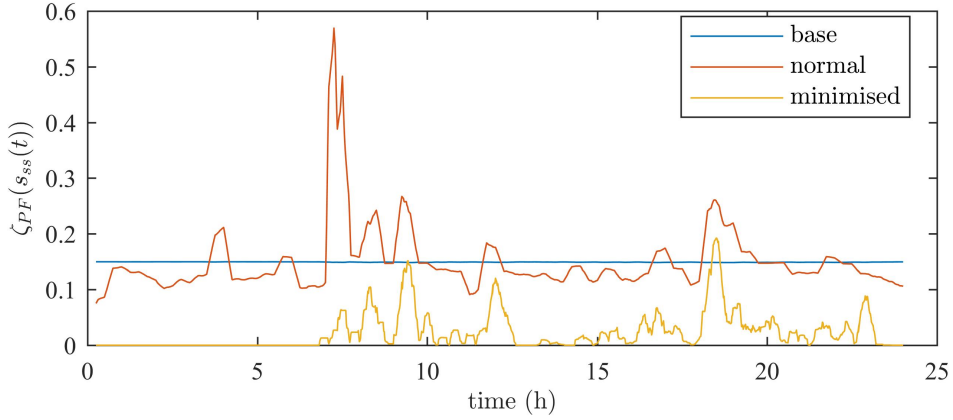


Figure 3.17: Power factor cost improvements due to the adjustment of the ESMU schedule

however successfully reduced throughout the entire day for the *minimisation* case, in comparison to the *normal* cases.

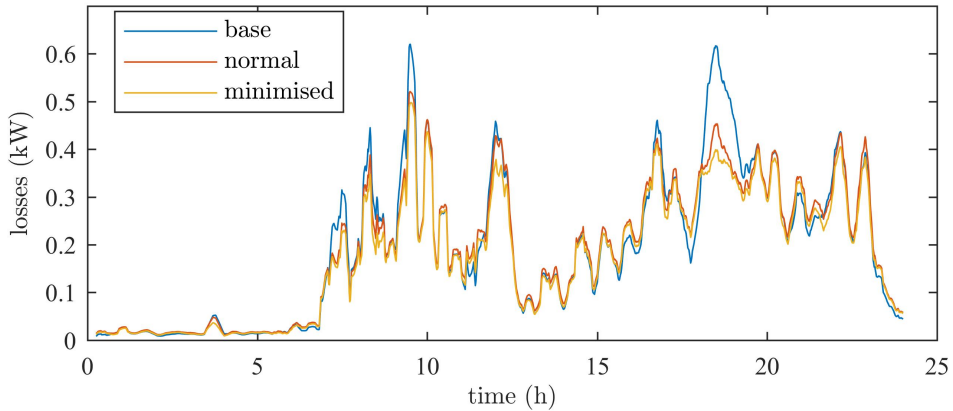


Figure 3.18: Instantaneous losses of the distribution network when adjusting the ESMU schedule in order to reduce the former (energy lost: 75.9Wh for base; 74.7Wh for normal; 69.9Wh for minimised).

The final parameter that indicates system efficiency are the distribution losses. Figure 3.18 shows the reduction in distribution losses that were achieved when adjusting the ESMU powers accordingly. In fact, an additional 6.42% energy savings is achieved, simply by adjusting the ESMU's power injection and absorption behaviour, when comparing the *base* and *minimisation* cases. Although this amount of energy may seem negligibly small, these saving can amount to a noticeable level of savings on

a national scale, which can potentially benefit the entire power network. Nonetheless, measuring losses is difficult and costly, which is why attempting to do so will likely outweigh the benefits.

Instead, a better way of relieving stress from the power network is to minimise its assets utilisation by mitigating demand spikes. Since the ESMU was constrained not to deviate from its underlying half-hourly schedule, only phase related demand differences could be addressed. Hence the impact of correcting those phase differences is barely noticeable, which can be seen in Figure 3.19.

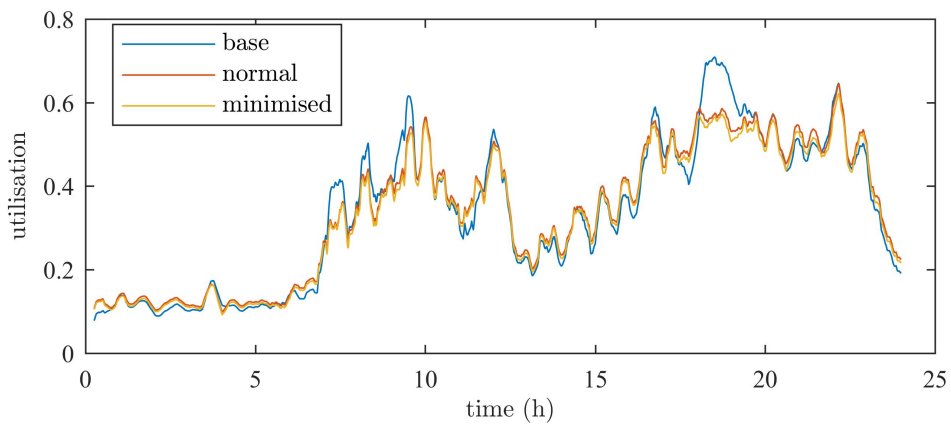


Figure 3.19: Improvement of the worst line utilisation across the entire network when adjusting the ESMU schedule correspondingly.

Whilst the *normal* case noticeably lowered some of the daily demand, power spikes after e.g. 9pm were not addressed at all. Even the *minimisation* case could barely reduce those spikes, due to the constraining half-hourly schedule. Nonetheless, throughout the entire day, ESMU was still able to reduce line utilisation at the substation level; despite those improvements being relatively small in comparison to the impact in the *normal* case.

3.5.2 Difference Analysis

In order to gauge whether the sub-half-hourly ESMU power adjustment results in a statistical difference in network performance, a box-plot was generated to compare

each *minimisation* with the corresponding *normal* case. Hence, the underlying data for each box-plot represents the difference between the *minimisation* case's costs and the *normal* case's costs, i.e. when operating without adjusting ESMU powers. Therefore, any positive difference in cost indicates an improvement to the system's performance, whilst a negative difference would imply a worsening. All cases are compared and plotted in Figure 3.20, and the complete set of box-plots (showing the "cross-cost difference") is included in Appendix A.1.2.

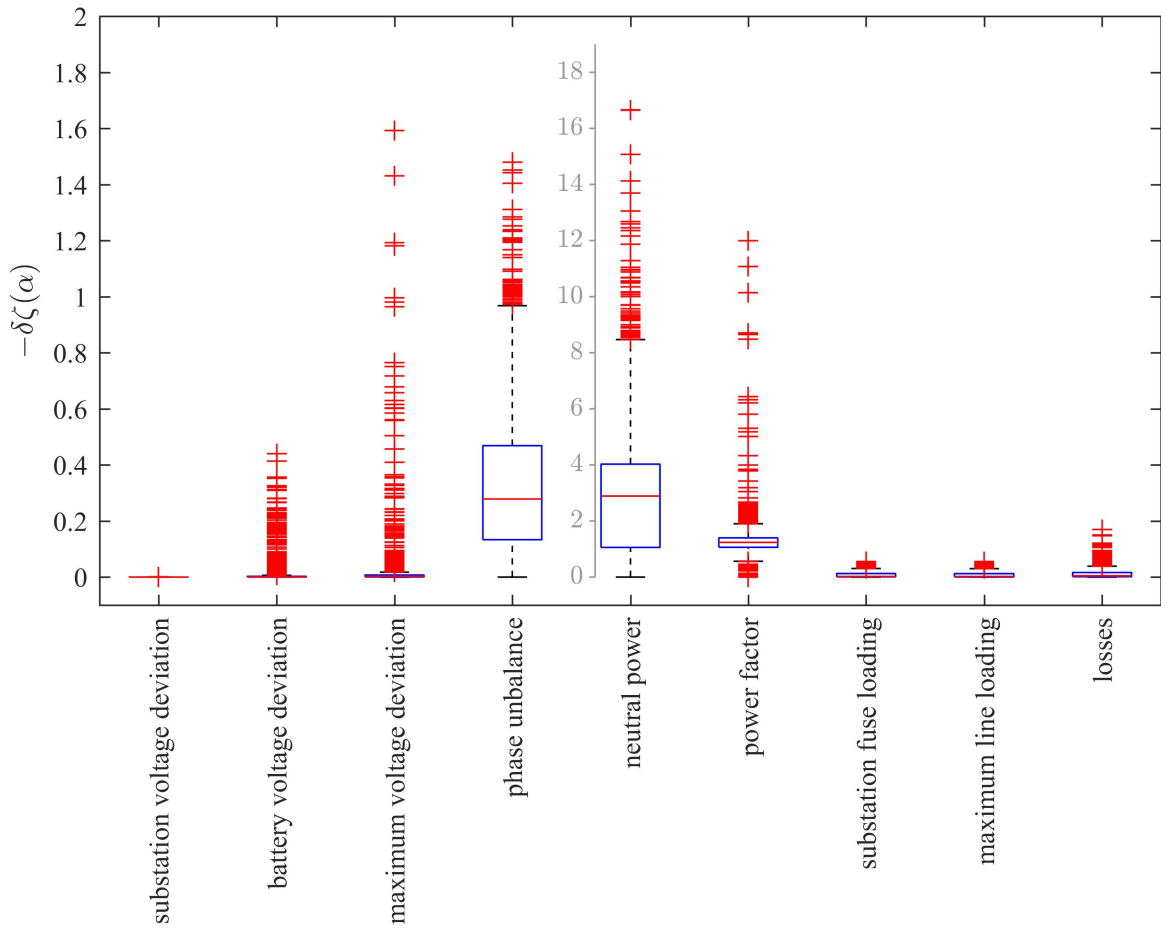


Figure 3.20: Cost-function improvement spread, when comparing against the normal ESMU operation case and when optimising for the underlying cost (a separate y-axis is introduced for the optimisation of "neutral power").

In this figure, it can be seen that the most significant cost related impact on the network is yielded, when improving phase unbalance, neutral power and power factor costs. Reason for this noticeably larger impact is due to ESMU being able to assign

its scheduled active power to all three phases in an optimal manner, as long as the predetermined half-hourly schedule is obeyed. It is this obedience constraint, that limits the extend by which all other key network parameters can be impacted. Reactive power on the other hand is only indirectly constrained by the ESMU schedule. The only limit that applies to the ESMU's reactive power injection capabilities is the remaining PMU capacity after committing the scheduled active power. Also, unlike active power, reactive power has a smaller impact on the LV network due to its physical property, i.e. being more resistive than inductive. Nonetheless, when each key network parameters became subject to their corresponding cost minimisation, all of them were impacted positively.

In addition to the box-plots, the cross-cost improvements (whose box-plots are presented in the Appendix A.1.2), are calculated and tabulated in Table 3.1. This table includes the cumulative difference in cost between the *normal* case and the *minimisation* case. However, instead of only presenting the cost reduction that is yielded when minimising it, this table also includes all other resulting costs; i.e. the daily aggregated cost to be precise. This value is defined as the “cumulative cost difference”. In addition to the comparison between *minimisation* and *normal* cases, the *normal* case is compared to the *base* case for reference. For convenience, all positive cost reductions (i.e. network improvements) have been highlighted.

As expected, all entries along the diagonal are positive in cross-cost difference, i.e. where the evaluated cost is also the cost that was minimised. But beside this fact, one can also observe which cost minimisation has an impact on different costs. For example, adjusting the ESMU schedule to achieve the largest reduction in distribution losses (i.e. far right column) improves nearly all key network parameters, apart from substation voltage deviation. Furthermore, Table 3.1 indicates that reducing battery voltage deviation, maximum voltage deviation, phase unbalance and neutral power (respectively, columns 3, 4, 5 and 6) have a noticeable impact on each other.

	minimisation cases									
	normal									
substation voltage deviation	substation voltage deviation									
battery voltage deviation	battery voltage deviation									
maximum voltage deviation	maximum voltage deviation									
phase unbalance	phase unbalance									
neutral power	neutral power									
power factor	power factor									
substation fuse loading	substation fuse loading									
maximum line loading	maximum line loading									
losses	losses									
substation voltage deviation	0.00	0.08	-2.49	-1.39	-4.89	-8.72	0.04	0.00	0.01	-1.09
battery voltage deviation	-5.01	-0.40	15.52	17.04	9.14	14.93	-2.85	-0.43	-1.62	13.69
maximum voltage deviation	-6.83	-1.15	28.22	36.42	24.66	33.05	-3.07	-0.56	-2.57	25.44
phase unbalance	12.15	40.93	284.87	380.57	490.22	351.35	40.66	10.02	5.03	441.24
neutral power	-0.83	-96.72	2303.70	1642.37	2698.78	4415.85	319.23	133.46	53.53	2401.12
power factor	-0.27	159.42	-7.63	-37.25	-633.30	-314.11	183.01	145.35	136.87	88.84
substation fuse loading	5.14	13.34	-0.43	-8.69	-51.76	-72.68	14.37	10.98	10.91	5.64
maximum line loading	4.53	12.88	-6.17	-10.04	-80.41	-97.30	13.89	10.69	10.94	4.72
losses	4.34	7.22	13.38	-4.46	-46.37	-66.32	12.89	9.65	9.02	17.13

Table 3.1: Gross-cost improvements due to adjustments to the original ESMU schedule.

Minimising any of these four costs does however not impact power factor, loading and losses (apart from reducing battery voltage deviation).

Then again, although the impact on network improvements for some costs is easily determined and explained with the underlying physical properties of distribution systems, other impacts of minimising cost do not share this transparency. For example, minimising power factor (column 7) has a greater impact on reducing line loadings than directly minimising substation or maximum line loading (column 8 and 9, respectively). Reason behind this effect is due to instantaneous apparent power contributing to the line current. This means, that maximising the network's power factor minimises reactive load, which in turn lowers the total line current. Since the solving algorithm does not know which cost to minimise first, the task of finding a global minimum becomes more difficult. To improve the performance of adjusting ESMU powers, one could propose to concatenate several cost minimisation procedures in a sequential series. Doing so would focus the search for global minima for each iteration of the sequence, yet this lies outside the scope of this Thesis and may be sought in future research.

3.5.3 Probability Density Analysis

The final part of analysing the results is to determine, whether the cumulative cross-cost differences are statistically significant. To do so, the probability density functions (PDF) of the cross-cost differences is analysed using a null hypothesis test. The underlying data is conditioned in order to meet all prerequisites that are necessary to perform the null hypothesis test, e.g. the standard t -test. These prerequisites include stationarity, low auto-correlation and high gaussianity of the underlying time-series. The procedure to meet these prerequisites is carried out without falsifying the data, which means that all applied conditioning operations were restricted to time-series division and linear transformation. Details on the exact data conditioning steps are

outside the scope of this chapter, but for completeness they are included in Appendix A.1.3.

Table 3.2 presents the results from this analysis, where p -values have been tabulated and those cells with a value below 0.05 have been highlighted. A similar pattern to that in the previous table can be seen (i.e. Table 3.1). In this table however, instead of just comparing cross-cost reductions, statistical indications to support the significance of the findings is presented. In combination with the preceding table, one can therefore determine that e.g. the impact of optimising operation based on maximum voltage deviation has little to no significant impact on improvements in power factor, whilst adjusting ESMU powers to improve the network’s power factor has the most significant statistical impact on the chosen key network parameters.

3.6 Summary

In this chapter, a method to adjust three-phase ESMU powers on a sub-half-hourly basis to support network operation, whilst following a pre-determined half-hourly schedule, is proposed and tested. The ESMU schedule is tailored to result in a “peak-shaving” and “valley-filling” behaviour and uses a realistic ESMU model to meet any operational constraints. A set of key network parameters to indicate the performance of the network, were used in a corresponding set of cost functions. By adjusting the ESMU’s active and reactive powers, each cost could be minimised and therefore network operation is improved.

Results indicate that when explicitly focusing on the improvement of certain key network parameters, then the derived cost reduces for every single case. Nonetheless, any cost minimisation had an effect on different costs (e.g. loss minimisation positively impacted nearly all other costs). Using cumulative cross-cost differences, it is shown that a net cost reduction is achieved, simply by implementing the proposed ESMU

	minimisation cases							
	normal				losses			
substation voltage deviation	0.851	< 0.001	0.999	1.000	0.999	1.000	< 0.001	< 0.001
battery voltage deviation	0.899	< 0.001	< 0.001	< 0.001	< 0.001	< 0.001	0.022	0.018
maximum voltage deviation	0.718	0.000	< 0.001	< 0.001	< 0.001	< 0.001	0.086	0.167
phase unbalance	0.331	< 0.001	< 0.001	< 0.001	< 0.001	< 0.001	0.001	0.038
neutral power	0.940	0.999	< 0.001	< 0.001	< 0.001	< 0.001	< 0.001	0.016
power factor	0.488	< 0.001	0.020	0.999	0.999	1.000	< 0.001	< 0.001
substation fuse loading	0.777	< 0.001	0.929	0.999	0.999	1.000	< 0.001	< 0.001
maximum line loading	0.846	< 0.001	0.996	0.999	0.999	0.999	< 0.001	< 0.001
losses	0.881	< 0.001	< 0.001	0.637	0.910	0.999	< 0.001	< 0.001

Table 3.2: p -values for statistical evidence of cross-cost improvements based on statistical two-sample single-tailed t -test.

power adjustment method top of the normal execution of a half-hourly schedule. This fact is also supported by the statistical sensitivity analysis, using the two-paired *t*-test. Using this test after having correctly preconditioned the data to meet the test's prerequisites, the initial null hypothesis is successfully be disproven; i.e. the hypothesis that sub-half hourly power adjustments have no impact. Hence there is strong evidence that those power adjustments do have a positive impact on the distribution network's operation.

The main limitation of the proposed method is however the battery's half-hourly schedule. It dictates the active power that has to be injected into or absorbed from the distribution network. Also, this schedule inadvertently dictates the remaining overhead in reactive power that may be compensated for on each phase. Therefore, the next chapter in this thesis presents a method of dynamically adjusting this scheduled power profile in real-time without violating any physical constraints.

Chapter 4

Real-Time Adjustment of Battery Operation using MPC Guided Schedule Deviation

M. J. Zangs, et.al., “Battery control algorithm for peak load shaving in low-voltage power network with high demand volatility,” Applied Energy, 2017

— Unpublished: (In review)

4.1 Overview

In the preceding chapter an Energy Storage Management Unit (ESMU) is used to improve network operation. This improvement is achieved by optimally adjusting the device’s scheduled three-phase powers. Any improvement is indicated by reduction of cost functions, which are tied to key network parameters. By focusing on different costs and repetitively optimising and simulating the ESMU powers, shows the extend by which the device can improve the network’s operation. However, this improvement is limited by the constraint of having to obey the underlying half-hourly ESMU schedule, despite applying adjustments at a sub-half-hourly level.

In the following chapter, this limiting constraint is lifted, and the corresponding sub-half-hourly ESMU schedule adjustment method is proposed. This method unifies the benefits from sub-half-hourly demand measurements and half-hourly demand forecasts. Unlike previous work in the field, the proposed approach reverses the traditional control paradigm to compensate for schedule inaccuracies. To reiterate, these traditional approaches implemented on-line control mechanisms, e.g. Set-Point Control (SPC), in combination with prediction models in order to adjust and prepare ESMU for future load trends. In this presented work however, instead of supporting on-line control with real-time load predictions, forecast driven schedules are adjusted using on-line measurements. This is achieved by first scheduling ESMU operation at half-hourly resolution, i.e. by following a “peak-shaving” and “valley-filling” behaviour which has been explained in Chapter 3, and then modifying this schedule using MPC. In this case, MPC is comprised of a lightweight AR model to assure real-time deployability. These two control signals are unified using two Proportional Integral Derivative (PID) compensators that are tuned to assure system robustness, regardless of the forecast’s erroneousness. All ESMU schedules are generated under the constraints of a realistic ESMU model, and all demand measurements and corresponding forecasts used in this work are based on real data, provided by the project partner and DNO: *Scottish and Southern Energy Networks* (SSEN). Results are generated from this realistic (i.e. provided) network load with corresponding load forecasts, and cases are compared against the original and a baseline load case (i.e. traditional off-line control). It is shown that, even under these imperfect forecast conditions, the proposed schedule adjustment method can successfully reduce sub-half-hourly peaks. In fact, whilst the probability distribution of the baseline case sat around an average of 1.78kW peak reduction, the proposed method increased the reduction to 5.24kW. Since this proposed control method is the natural extension of our previous work in [58], it is hereon referred to as “dynamic control”.

The chapter is organised as follows: In Section 4.2, all constituent system components including ESMU model, forecast acquisition and ESMU schedule generation are explained. Section ?? presents the dynamic control, including the dual PID setup and MPC. Section 4.4 outlines the different case studies that were used to compare the performance of the dynamic control. In Section 4.5, all results from these case studies are presented and discussed. Finally, conclusion and the future work are described in Section 4.6.

4.2 System Explanation

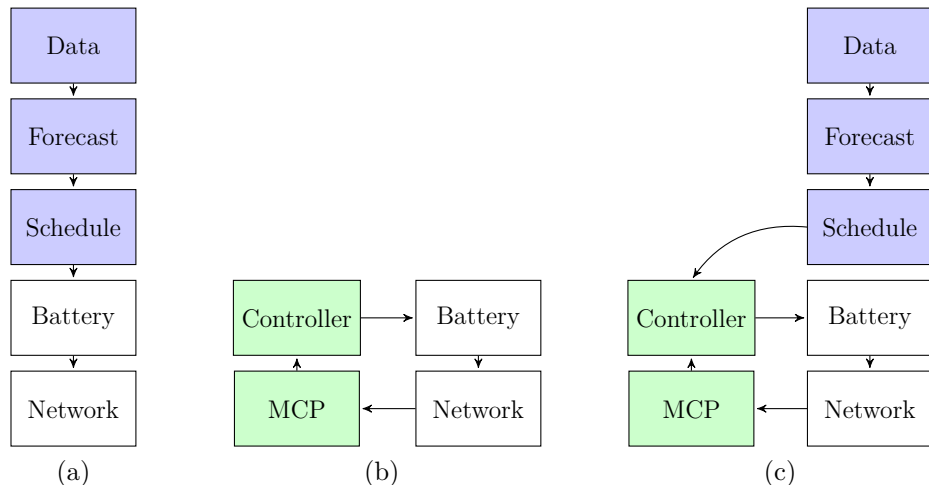


Figure 4.1: (4.1a) Traditional forecast driven BESS control; (4.1b) Traditional on-line system; (4.1c) Proposed dynamic control system

The presented work is part of the *New Thames Valley Vision* (NTVV) research project, and was conducted in collaboration with the British DNO *Scottish and Southern Energy Networks* (SSEN) [59]. From the findings of this research project, the diagram in Figure 4.1 was generated, showing two well established ESMU control approaches and the proposed dynamic control approach. This figure includes all constituent systems that were used during the ESMU street-level deployment. The two traditional systems are off-line and on-line ESMU control, which are shown in Figure

4.1a and 4.1b, respectively. Alongside these two control approaches is the proposed dynamic control system, as shown in Figure 4.1c. This control approach entails the benefits from both the traditional half-hourly forecast driven and the sub-half-hourly ESMU control system, and can therefore be seen as the hybrid of the two traditional systems. Unlike previous work however, this hybrid system does not use Set-Point Control (SPC), which is aided by a MPC to compensate for trends in the load profile. Instead, it operates by executing a predetermined half-hourly ESMU schedule with sub-half-hourly adjustments. Those adjustments are based on MPC-guided instructions, and details about this dynamic control are outlined in Section ??.

In this section however the battery model, which is used in this work, is explained first. Also the load data acquisition, forecasting and ESMU schedule generation are outlined, where scheduling is performed in accordance to the ESMU model's constraints.

4.2.1 ESMU model

The ESMU model is based on the physical system that was deployed by SSEN during the NTVV project. Therefore, the model is designed to accurately capture the physical limitations of the device, which includes a limited capacity of the battery pack, C_{bat} , and a corresponding charge and discharge factor (i.e. the “C-factor”), C_f , to also limit the maximum charge and discharge rate*. Furthermore, the power electronics unit that regulates the three-phase power flow into and out of the ESMU is limited by its power ratings, P_{bat} , which must not be exceeded. Corresponding conversion losses within the power electronics unit lead to a limited ESMU round-trip efficiency, η , where $\eta \in (0, 1]$. Self-discharge losses inside the battery pack are also included as the ratio μ , where $\mu \in (0, 1]$. This ratio expresses how much energy is lost over time,

*Nominal charge and discharge powers are calculated from the “C-factor” and the capacity of the battery. For example, a 12.5kWh battery with a C-factor of $1.6(\text{h}^{-1})$ would have a maximum dis/charge rate of 20kW ($= 12.5 \cdot 1.6$).

due to the battery's imperfect means of storing energy.

The dynamics of ESMU are modelled over discrete time, t where $t \in \mathbb{Z}_{\geq 0}$, by simulating the transition from one State of Charge (SOC) to the next. A finite sampling period between each simulation's time-step is defined and notated as Δt , and this sample period represents the highest temporal resolution used in the context of this work, i.e. sub-half-hourly resolution. Change in State of Charge, i.e. $\delta SOC(t)$, can then be defined as the difference between the current State of Charge, $SOC(t)$, and the subsequent State of Charge, $SOC(t + \Delta t)$. When combining this definition with the self-discharge loss, the following SOC equation can be formulated:

$$SOC(t + \Delta t) := \eta(SOC(t) + \delta SOC(t)) \quad (4.1)$$

Hence, $\delta SOC(t)$ is the result of charging or discharging the battery by consuming or releasing energy. The amount of energy that flows into or out of the ESMU is equal to the active power, $p(t)$, that is applied over the sampling period Δt . Yet $\delta SOC(t)$ is not equal to this consumed energy, due to the imperfect round-trip efficiency. In order to act like a load in the LV network, positive power is associated to charging and negative power is associated to discharging the ESMU. Therefore, the sign of the ESMU power indicates the direction of the flowing energy, and based upon this direction of energy flow, the true amount of stored charge can be calculated by using the aforementioned round-trip efficiency, μ . In order to correctly inject or absorb power into or from the network, ESMU power is given and battery power, $p_{bat}(t)$, is derived and defined as follows:

$$p_{bat}(t) = \begin{cases} \mu p(t) & \text{if } p(t) \geq 0 \\ \frac{1}{\mu} p(t) & \text{otherwise} \end{cases} \quad (4.2)$$

As power electronics approach ideal performance, μ tends towards one, however a

value of 0.95 is chosen for the model to coincide with the technical specifications of the deployed ESMU units. Knowing both the power at street- and at the battery-level, the amount of energy injected into the battery during Δt can be determined:

$$\delta SOC(t) = \frac{\Delta t}{C_{bat} (3.6 \times 10^6)} p_{bat}(t) \quad (4.3)$$

Combining Equation 4.1, 4.2 and 4.3 and solving for $SOC(t + \Delta t)$, yields the following battery model equation:

$$SOC(t + \Delta t) = \begin{cases} \eta \left(SOC(t) + \frac{\mu \Delta t p(t)}{C_{bat} (3.6 \times 10^6)} \right) & \text{if } p(t) \geq 0 \\ \eta \left(SOC(t) + \frac{\Delta t p(t)}{\mu C_{bat} (3.6 \times 10^6)} \right) & \text{otherwise} \end{cases} \quad (4.4)$$

For the purpose of the simulation, it is assumed that the battery is initially charged up to 50%. Hence, the initial conditions of this model are defined as $SOC(0) = 0.5$, which makes the model valid for a time span of $t \geq 0$.

4.2.2 Load data and ESMU scheduling

Having established the ESMU model, the procedure to generate a corresponding schedule is explained in this section. Following common scheduling practice and for the reasons mentioned in the literature review, this schedule is generated at half-hourly temporal resolution. Since ESMU operates at a sub-half-hourly period, i.e. with a sampling period of Δt , the schedule's period is denoted as multiple of that, e.g. $30\Delta t$ when Δt is defined as one minute. These two sampling periods introduce the requirement of having to synchronise the two, i.e. half-hourly and sub-half-hourly periods. For clarity, a conversion function, $k(t)$, is therefore defined that links the sub-half-hourly timing, t , to its corresponding half-hourly sample:

$$k(t) := \left\lfloor \frac{t-1}{30\Delta t} \right\rfloor + 1 \quad (4.5)$$

Having established a means of synchronising the two sampling periods, the wanted behaviour of the ESMU schedule is defined next. For simplicity linear forwarding was chosen, which means that the power assigned at e.g. $t = 1$ remains constant over the scheduling period of $30\Delta t$, until $t = 31$. With this assumption, the ESMU's SOC can be calculated for each t despite the scheduled power profile only having been defined for every 30th t . Furthermore, with this second assumption, not only every sub-half-hourly ESMU power can be derived from its half-hourly schedule, but it also enables the calculation of every SOC, i.e. $SOC(t)$ is well defined.

For the generation of the ESMU schedule a load forecast, \mathbf{p}_{for} , was required; here $(p_{\text{for}}(k(t))) = \mathbf{p}_{\text{for}}$. This forecast, similar to the ESMU schedule, is also at half-hourly temporal resolution and is provided by SSEN as part of the NTVV research project. The task at hand is to find a half-hourly ESMU schedule, \mathbf{p}_{sch} , where $(p_{\text{sch}}(k(t))) = \mathbf{p}_{\text{sch}}$, that improves the shape of the underlying forecast, e.g. by reducing load peaks. In order to generate this optimised ESMU schedule, a metric quantifying improvements had to be defined first. The only remaining problem is to find a half-hourly schedule, \mathbf{p}_{sch} , which is done through by minimising several cost-functions.

In this work, three cost-functions are used that quantify the network improvements, yielded by \mathbf{p}_{sch} . These costs entailed the Peak-to-Average Ratio (PAR), the difference between the resulting power profile's maximum and minimum (MMD) load, and the magnitude of all power transients (TRA) [60, 61]. Before explaining each of these three cost functions however, a notation simplifying power as, \mathbf{p} , is introduced:

$$p(t) = p_{for}(k(t)) + p_{sch}(k(t)) \quad (4.6)$$

where $(p(t)) = \mathbf{p}$

Within this section, the vector \mathbf{p} represents the power profile as it would be measured at the substation when both forecast, $p_{for}(t)$, and scheduled, $p_{sch}(t)$, power were applied. The first cost function, addressing the minimisation of PAR, is defined as follows:

$$\zeta_{\text{PAR}}(\mathbf{p}) := \frac{\max_t |\mathbf{p}|}{\bar{\mathbf{p}}} - 1 \quad (4.7)$$

Here, $\bar{\mathbf{p}}$ represents the mean power, i.e. $\bar{\mathbf{p}} = \frac{\Delta t}{T_{\text{sch}}} \sum_{t=1}^{T_{\text{sch}}} p(t)$ and $\bar{\mathbf{p}} \in \mathbb{R}$, where T_{sch} is the length of the scheduling horizon in regards to the sampling period Δt . From this cost, a perfect power profile would yield a PAR cost of zero, if the profile is a perfectly flat. However, due to limited battery capacity, achieving such a cost of zero is unlikely. The second cost function represents the difference between minimum and maximum power of \mathbf{p} :

$$\zeta_{\text{MMD}}(\mathbf{p}) := \max_t(\mathbf{p}) - \min_t(\mathbf{p}) \quad (4.8)$$

Similar to the PAR, this cost also reduces to zero when the resulting power profile is a perfectly flat line. Unlike the PAR, this cost does not incentivise an increase of mean power. Minimising PAR by itself may result in unnecessary and potentially damaging battery cycling, when trying to elevate the power profile's mean, yet this is avoided when ζ_{MMD} is included alongside ζ_{PAR} . However, ζ_{PAR} and ζ_{MMD} only impact the fringes of the resulting half-hourly power profile. The final cost therefore addresses the interim power volatility by aiming to minimise the largest possible power transient:

$$\zeta_{\text{TRA}}(\mathbf{p}) := \max_t |p(t + \Delta t) - p(t)| \quad (4.9)$$

Minimising this final cost has a smoothening effect on the improved half-hourly power profile, since a profile with no transients is by definition a flat smooth profile. All three cost functions are summaries into a single global cost function, where only the half-hourly ESMU schedule, \mathbf{p}_{sch} , is used as an input and the forecast, \mathbf{p}_{for} , is kept as constant:

$$\begin{aligned} \zeta(\mathbf{p}_{\text{sch}}) := & \zeta_{\text{PAR}}(\mathbf{p}_{\text{sch}} + \mathbf{p}_{\text{for}}) \\ & + \zeta_{\text{MMD}}(\mathbf{p}_{\text{sch}} + \mathbf{p}_{\text{for}}) \\ & + \zeta_{\text{TRA}}(\mathbf{p}_{\text{sch}} + \mathbf{p}_{\text{for}}) \end{aligned} \quad (4.10)$$

Subject to ESMU constraints, this global cost function is minimised using a standard solver (i.e. Sequential Quadratic Programming - SQP) to yield a ESMU schedule that is optimised for the given forecast:

$$\begin{aligned} \min_{\mathbf{p}_{\text{sch}}} & \zeta(\mathbf{p}_{\text{sch}}) \\ \text{s.t. } & \begin{cases} SOC_{tol} \leq SOC(t) \\ SOC(t) \leq 1 - SOC_{tol} \\ |p_{bat}(t)| \leq C_{bat} \times C_f \end{cases} \end{aligned} \quad (4.11)$$

In order to limit the control's flexibility, a State Of Charge tolerance, SOC_{tol} , is included in this minimisation problem. SOC_{tol} defines the maximum allowed deviation from the computed SOC profile without hitting operational limits, i.e. SOC of one or zero, and may take values in the form of $SOC_{tol} \in [0, 0.5]$, where 0 implies no

tolerance and 0.5 implies complete flexibility. For the work at hand, a value of 0.1 was chosen.

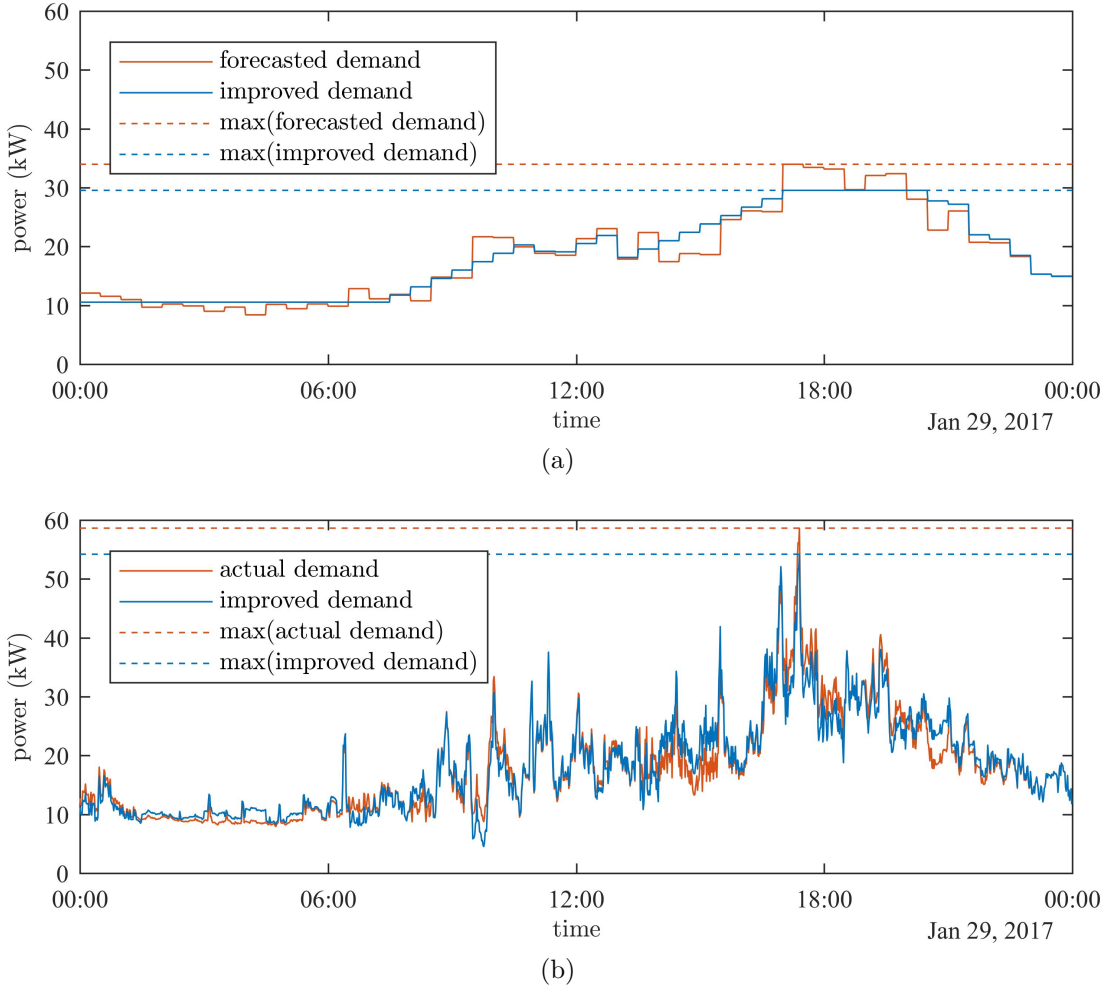


Figure 4.2: An example of applying a half-hourly ESMU schedule to its half-hourly schedule (Subfig. 4.2a) and the actual, sub-half-hourly daily load (Subfig. 4.2b).

As repetitively mentioned, the ESMU that results from this scheduling mechanism is at half-hourly resolution and has therefore limited impact on sub-half-hourly load variation. To visualise this limitation, a single day's ESMU schedule was generated from its corresponding forecast as defined in Equation 4.11, and plotted in Figure 4.2. In this simple comparison, the noticeable discrepancy between the half-hourly ESMU schedule and the actual, sub-half-hourly demand can be observed. Furthermore, noticeable disparity in peak duration, magnitude and volatility can be noted. This

discrepancy and disparity emphasise the incompatibility issues between half-hourly ESMU schedules and the actual sub-half-hourly load. As previously discussed, benefits of ESMU were intended to mitigate sub-half-hourly load volatility, yet this cannot be achieved when solely applying half-hourly ESMU schedules in an off-line manner. Therefore, in the next section, the control strategy to add an on-line component is explained.

4.3 Control of ESMU

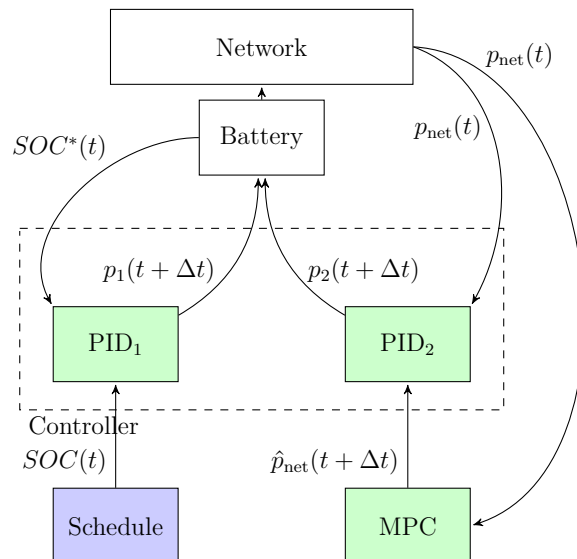


Figure 4.3: Dynamic controller breakdown as previously shown in Figure 4.1c.

This section explains the dynamic control (i.e. the controller block that is shown in Figure 4.1c), which contains the two PID compensators. The first PID compensator is fed by the ESMU schedule, and the other is fed by the MPC load estimations. After the control system is detailed in this section, the auto-regressive models, which were used during the course of this research, are explained, too.

4.3.1 Dynamic control

The content of the dynamic control procedure is shown in Figure 4.3. Here, two reference signals are used as inputs to the dynamic control. The first reference signal is the SOC profile derived from the ESMU scheduled, $SOC(t)$, and the second is an estimated future network power, $\hat{p}_{\text{net}}(t + \Delta t)$. These two inputs are fed into compensator PID₁ and compensator PID₂, respectively. The output of each compensator is a corrective battery power component that, when summed, yields the next ESMU power, i.e. $p_1(t + \Delta t)$ and $p_2(t + \Delta t)$, which is applied to the ESMU model. Each PID compensator also receives a feedback signal to compute the internal error states. More specifically, PID₁ receives the most recent SOC value that is obtained from the ESMU model, $SOC^*(t)$, and PID₂ receives the network's most recent power demand, $p_{\text{net}}(t)$ (e.g. through measurements by substation monitoring).

Inside the PID₁ component, a SOC error term, $E_{\text{SOC}}(t)$, is computed. This term is the difference between the scheduled SOC profile, $SOC(t)$, and the actual (or simulated) SOC values, $SOC^*(t)$. The following equation captures this error term.

$$E_{\text{SOC}}(t) := SOC^*(t) - SOC(t) \quad (4.12)$$

Applying a standard, linearly weighted dynamic gain vector, $\boldsymbol{\alpha}$, to the SOC error, allows the calculation of a corrective ESMU power component dynamically. Here, $\boldsymbol{\alpha} = \{\alpha_P, \alpha_I, \alpha_D\}$, where being the P, I and D weights, respectively. This corrective power is denoted as $p_1(t + \Delta t)$, and is defined as follows:

$$\begin{aligned} p_1(t + \Delta t) &:= \alpha_P E_{\text{SOC}}(t) \\ &+ \alpha_I \sum_{i=0}^{\infty} E_{\text{SOC}}(t - i\Delta t) \\ &+ \alpha_D \frac{E_{\text{SOC}}(t) - E_{\text{SOC}}(t - \Delta t)}{\Delta t} \end{aligned} \quad (4.13)$$

Here, the integral component removes steady-state error and the instantaneous error differential prevents overshooting. All in all, this compensator uses present and past values to issue a corrective future ESMU instruction. Compensator PID_2 on the other hand uses values from the present, past and future in order to minimise the power transient and load peaks.

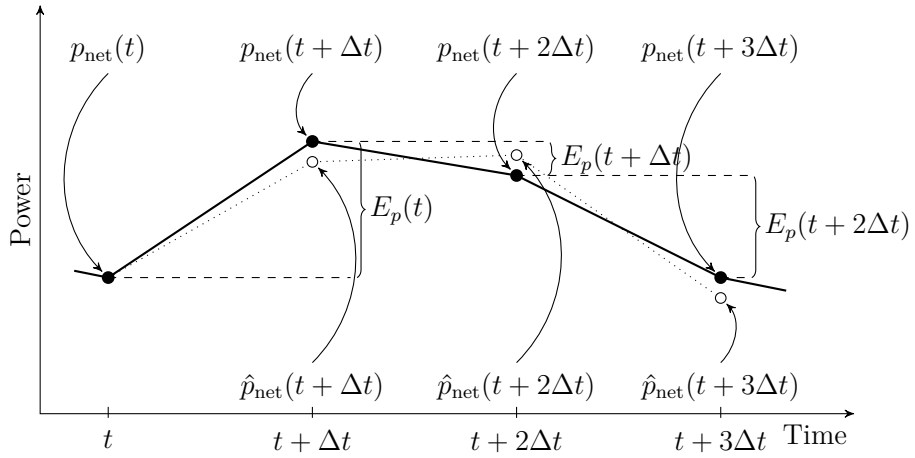


Figure 4.4: Underlying time-series based compensation strategy for compensator PID_2 .

Figure 4.4 summarises the time series computations for each power sample at times t , $t + \Delta t$, etc. Ideally, PID_2 uses present power readings, $p_{\text{net}}(t)$, and a power value of the immediate future, i.e. $p_{\text{net}}(t + \Delta t)$, to compute a power error signal, which is to be reduced to a smallest possible value. This error signal is defined as:

$$E_p(t) := p_{\text{net}}(t + \tau) - p_{\text{net}}(t) \quad (4.14)$$

However, since the future network power is unknown an “estimated next power”, $\hat{p}_{\text{net}}(t + \Delta t)$, is used instead. This value is the PID_2 ’s input from the MPC and results in an “estimated power error signal”:

$$\hat{E}_p(t) = \hat{p}_{\text{net}}(t + \tau) - p_{\text{net}}(t) \quad (4.15)$$

Similarly to PID_1 , PID_2 produces a corrective ESMU power component, $p_2(t)$ that

smoothens the resulting power profile. This corrective ESMU power is also computed using a standard linear weighted dynamic vector β (with $\beta = \{\beta_P, \beta_I, \beta_D\}$, being the P, I and D weight, respectively):

$$\begin{aligned} p_2(t + \tau) &:= \beta_P E_p(t) \\ &+ \beta_I \sum_{i=0}^{\infty} E_p(t - i\tau) \\ &+ \beta_D \frac{E_p(t) - E_p(t - \tau)}{\tau} \end{aligned} \quad (4.16)$$

Finally, the “next ESMU power” can be deduced by adding the two corrective ESMU power components, as shown in the equation below.

$$p(t + \Delta t) = p_1(t + \Delta t) + p_2(t + \Delta t) \quad (4.17)$$

Both PID compensators do however depend on correctly chosen weights for α and β . Therefore they need to be tuned prior to executing the dynamic control. For this work a minimisation problem was formulated, based on a cost function, $\zeta^*(\alpha, \beta)$, to deduce the two weight vectors as follows:

$$\begin{aligned} \min_{\alpha, \beta} \zeta^*(\alpha, \beta) \\ \text{s.t. } \begin{cases} SOC(t) - SOC_{tol} \leq 0 \\ -SOC(t) \leq 0 \\ SOC(t) - 1 \leq 0 \end{cases} \end{aligned} \quad (4.18)$$

Here, $\zeta^*(\alpha, \beta)$ is defined as:

$$\zeta^*(\alpha, \beta) := \max_t (\mathbf{p}_{net} + \mathbf{p}) \quad (4.19)$$

where $(p_{net}(t)) = \mathbf{p}_{net}$ and $(p(t)) = \mathbf{p}$

In Equation 4.18 and 4.19, $\zeta^*(\alpha, \beta)$ represents the sub-half-hourly peak load during a day, when ESMU schedules are adjusted with the corresponding α and β weights. Also, the same SOC tolerance that was used to generate the SOC schedule, i.e. SOC_{tol} , is included to prevent the solution from deviating off the prescheduled SOC profile. To generalise this solution for all load cases, a minimisation problem was formulated to solve multiple daily load profiles in order to find ideal α and β weights. This resulting set of α and β weights, therefore guaranteed a convergent and stable solutions. The details concerning these case studies themselves, are however outlined in Section 4.4.

4.3.2 Model predictive control

As explained in the literature review in Chapter 2, Model Predictive Control (MPC) is favoured over Set-Point Control (SPC), since it takes into account time-series to produce a behaviour. With this knowledge, MPC can be used to not only react to recent changes but also to counteract foreseen trends. Different approaches exist to obtain these foreseen trends and these approaches highly vary in accuracy, computational burden and robustness. Equally, the characteristics of underlying data which is used to train these models impacts their performances. For the presented work, an efficient and robust approach is required, since system deployment dictates these functional requirements. As a result, prediction accuracy is an optional requirement, which becomes important only when the predicting model can issue predictions in real-time and does (for the predicting horizon) remain stationary and bounded.

The simplest form of producing a prediction, is to assume that the currently

observed load will also apply in the future. This kind of prediction does however not take into account model dynamics. An AR model on the other hand, uses a series of past observations to predict the next. Yet the further into the future these predictions are made, the less accurate they become. Therefore, this work only attempts to issue a power prediction for the immediate future, i.e. next sample time at $t + \Delta t$. Furthermore, to reduce computational burden and guarantee real-time operation, the simplest dynamic model, i.e. an Auto-Regressive (AR) model is chosen instead of e.g. deep artificial neural networks. Since external forces can and often do impact the behaviour of the model, the AR model is treated as an exogenous model, with a time-series of input powers, $p(t) \in \mathbf{p}$, a time-series of predicted “next powers”, $\hat{p}(t) \in \hat{\mathbf{p}}$, and an internal delay function $t - \Delta t$.

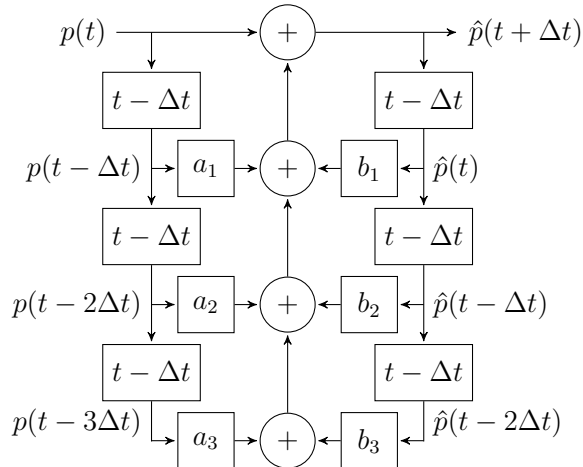


Figure 4.5: Exogenous auto-regressive model that is used for model predictive control. Here, $t - \Delta t$ indicates the time delay by one sample period.

Figure 4.5 graphically captures the standard AR model’s function tree, which is also represented mathematically in the following equation:

$$\begin{aligned} \hat{p}(t + \Delta t) = & p(t) + \sum_{i=1}^N a_i p(t - i\Delta t) \\ & + \sum_{i=1}^N b_i \hat{p}(t - (i-1)\Delta t) \end{aligned} \quad (4.20)$$

Values of the two weight vectors **a** and **b**, where $(a_i) = \mathbf{a}$ and $(b_i) = \mathbf{b}$, are determined during runtime using the standard adaptive least squares algorithm. This algorithm dynamically adjusts **a** and **b** to minimise the prediction error at each time-step. Beside finding optimised values for **a** and **b**, the model's number of regressors, N , is also predicted to impact the model's performance (N is also referred to as the “model length”). The example in Figure 4.5 represents a symmetric model where $N = 3$. This short length however is most likely insufficient in predicting $p(t + \Delta t)$, which is why several models of increasing lengths are assessed and compared. From this comparison, the impact of N on the models' resulting values of $\hat{p}(t + \Delta t)$, and correspondingly on the performance of the dynamic controller can be discussed. Details about the cases for different model length are presented in the case studies in Section 4.4.

4.4 Case studies

Two cases are defined that the performance of the proposed dynamic control is compared against: case **O** and case **B**. More specifically, case **O**, original case, is the scenario where no ESMU operation takes place. Traditional off-line ESMU operation that only uses predetermined half-hourly ESMU schedules is referred to as the benchmark case, or case **B**. All remaining cases, which are explained below, are capture different versions of the dynamic control.

In addition to the two comparison cases, three more different case studies are defined: cases **I**, **II** and **III**. This group of three case studies evaluates the impact of the proposed dynamic control when subjected to realistic (i.e. imperfect) half-hourly load forecasts. In each of the three cases, a different mechanisms is used to predict the power volatility. More specifically:

- case **I** implements the simplest prediction mechanism, i.e. it is assumed that

the current power measurements repeats,

- case **II** uses the aforementioned MPC, and performance of different AR model lengths is compared, and
- case **III**, the third and final case, represents an ideal scenario where perfect foresight is assumed and the exact next load can be estimated.

For clarity, all three cases, numbered **I** to **III**, are summarised and tabulated in Table 4.1.

estimation method	real forecast
power repetition	I
MPC (AR/ARX)	II
perfect foresight	III

Table 4.1: Three cases and their dynamic control input assumptions

Results from all ESMU cases (**B**, **I**, **II** and **III**) are first compared against the original, i.e. uncompensated, network load case (**O**). Here, by using a sample day, the assessment of load profile improvements are made clear. Once it is clear how each day's peak is reduced by the algorithm, the daily peak reduction capability from all cases' results are compared. Rather than assessing the underlying load profile from a time-series perspective, only focus is put on any further peak load reductions. However, the number of days may make it difficult to spot trends and improvements in the data. Therefore, from the daily peak reduction results, a Probability Density Function (PDF) is derived, which is based on kernel density estimation. The PDF shows the stochastic improvement of each case type in comparison to the original case, i.e. case **O**.

4.5 Results and discussion

The proposed cases are used to control power flow of the ESMU using 24 days of uninterrupted sub-half-hourly load record. At first, the time-series improvements are presented, where a day’s peak reduction due to the sub-half-hourly schedule adjustment are highlighted. Then, the daily peak reduction across the entire dataset is presented, following by a probability density plot to better compare these findings.

4.5.1 Time-series analysis

A single day was plotted in Figure 4.6, which shows the time-series improvements, yielded by the ESMU operation. For visual clarity, Figure 4.6a and 4.6b show, respectively, the entire day and a zoomed in version of the ESMU impact. It can be observed, that the unmodified demand profile, i.e. the original case (case **O**), and the case where scheduled half-hourly ESMU operation is applied, i.e. the baseline case (**B**), result in noticeably higher load peaks than any of the three adjustment cases. More specifically, the original peak reduction (which is equal to the scheduled ESMU power) was 1.8kW (3.9% reduction), whereas the average peak reduction when adjusting ESMU operation was 9.6kW (20.6% reduction). Furthermore, figure 4.6a highlights the volatility of the underlying data, which was not included in the half-hourly ESMU schedule.

Interestingly, both the standard AR and the exogenous AR estimation models, that were used in case **II**, performed very similar and show little to no significant difference in peak reduction performance. Equally noteworthy is the fact, that the simplest prediction methods of them all, i.e. the method of “assuming a power repetition occurs”, like in case **I**, yields good results, too. The amount by which the three cases were able to reduce the daily peak load is also highlighted with the corresponding horizontal dashed lines and dots located at the point of peak load. These initial

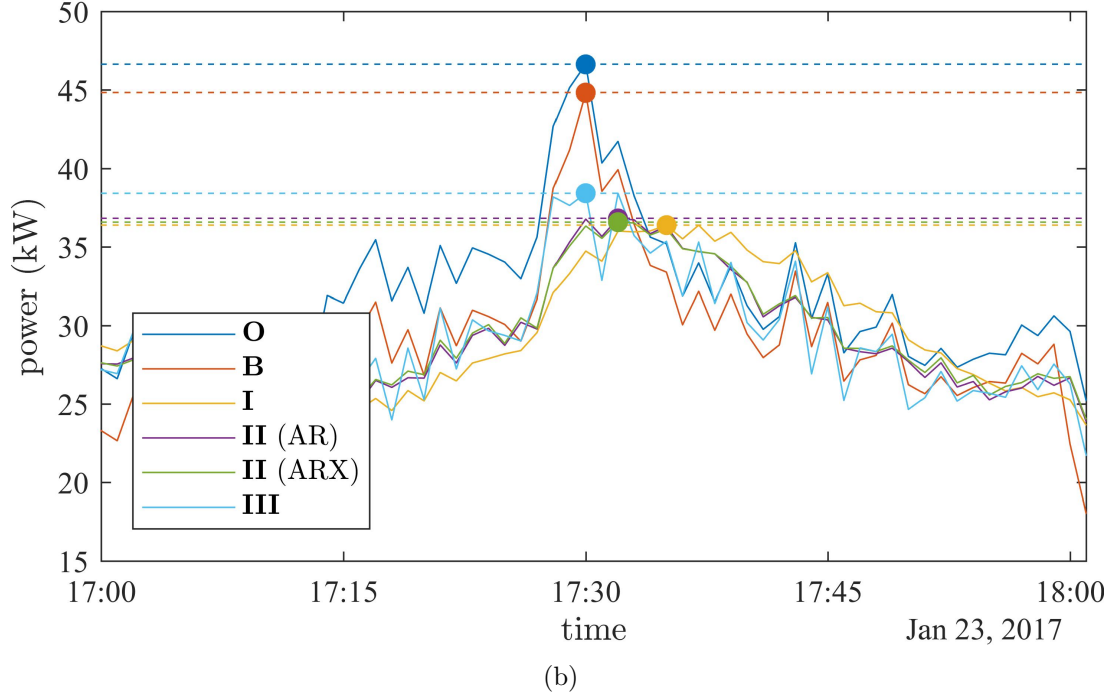
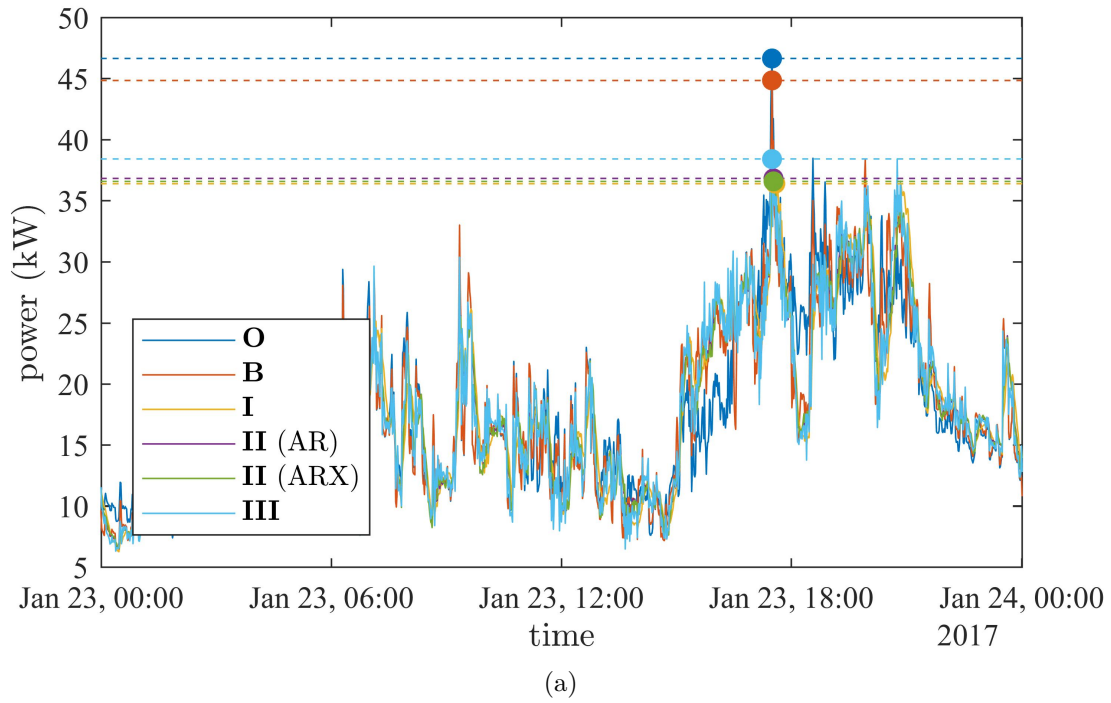


Figure 4.6: Time series performance over a single day when using realistic load forecasts: (4.6a) total day; (4.6b) zoomed in on critical period

findings show that every single version of dynamic control reduces peak load further, when compared to the baseline case **O**. This finding is as tabulated in Table 4.2, and suggest that the prediction mechanism by itself did play a small role in compensating for demand volatility.

case	O	B	I	II (AR)	II (ARX)	III
peak (kW)	46.6	44.8	36.4	36.8	36.6	38.4

Table 4.2: Peak reduction in time-series sample

However, the general magnitude of peak reduction performance can only be assessed if the complete dataset is evaluated. Hence, the next section compares the daily peak load reduction from the application of each case.

4.5.2 Daily peak reduction

In Figure 4.7, every day's power peak was extracted, similar to the procedure used for Figure 4.6. Here, however, both the actual power peaks as well as the relative power improvements, i.e. in comparison to the original power peak, were plotted. This was done in Figure 4.7a and Figure 4.7b, respectively. From both plots, it can be seen that controlling ESMU using the proposed dynamic control lowers peak load, especially when the underlying ESMU schedule originally worsened and increased peak load. Such behaviour can be observed for e.g. days six, where the half-hourly ESMU schedule worsened the actual load peak, yet ESMU schedule adjustment mechanisms compensated for this error. Nonetheless, having a larger set of peak reduction results to compare the dynamic control's performance against the baseline cases, sensitivity to the underlying power prediction approaches become apparent, too. For example, case **I**, using the simplest prediction mechanism, underperformed on day 23 and worsened the peak power. In order to get a better idea of the general peak reduction

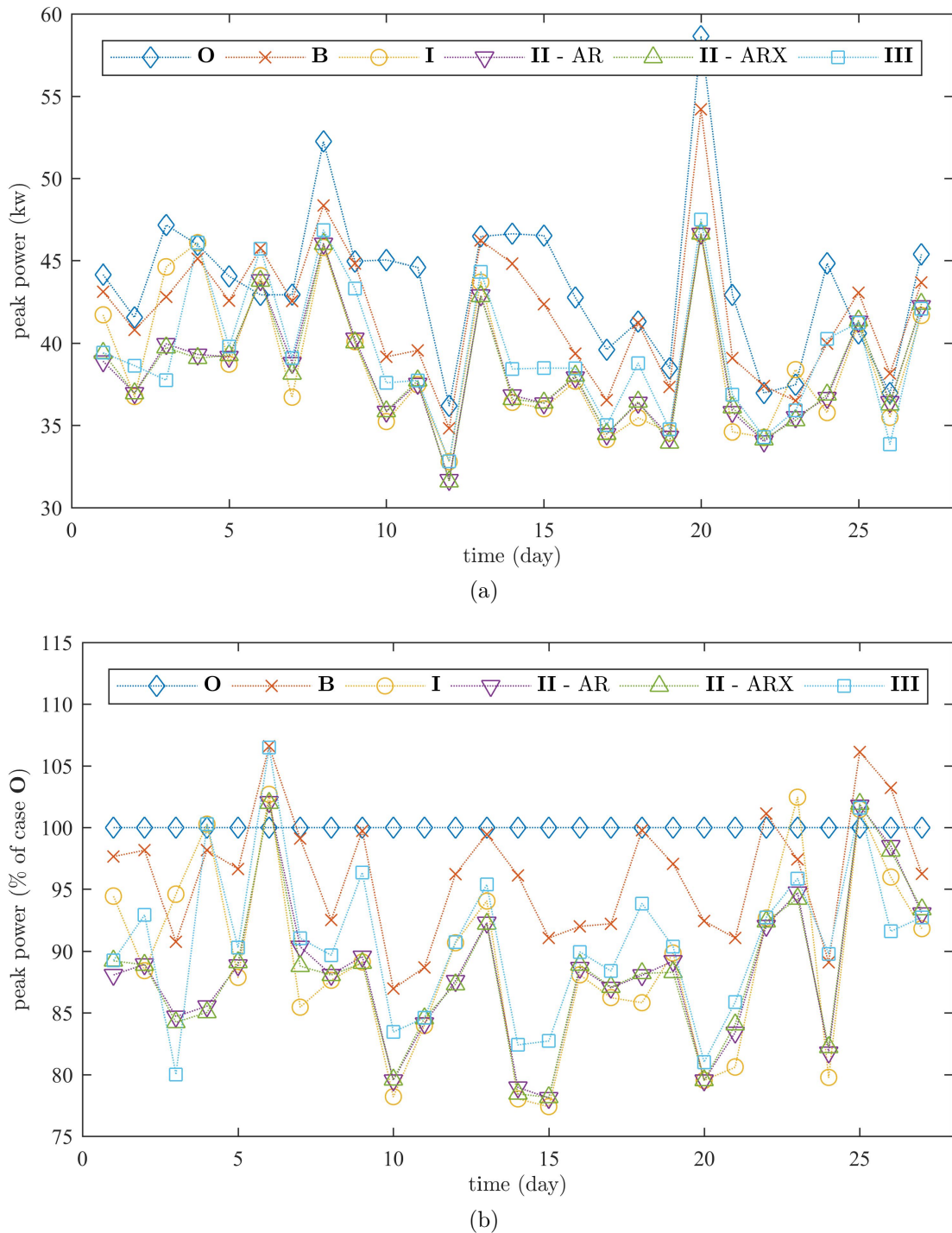


Figure 4.7: Daily peak reduction when using realistic forecasts.

performance when applying case **I**, **II** or **III**, the Probability Density Function was estimated and plotted in the following section.

4.5.3 Probability of peak reduction

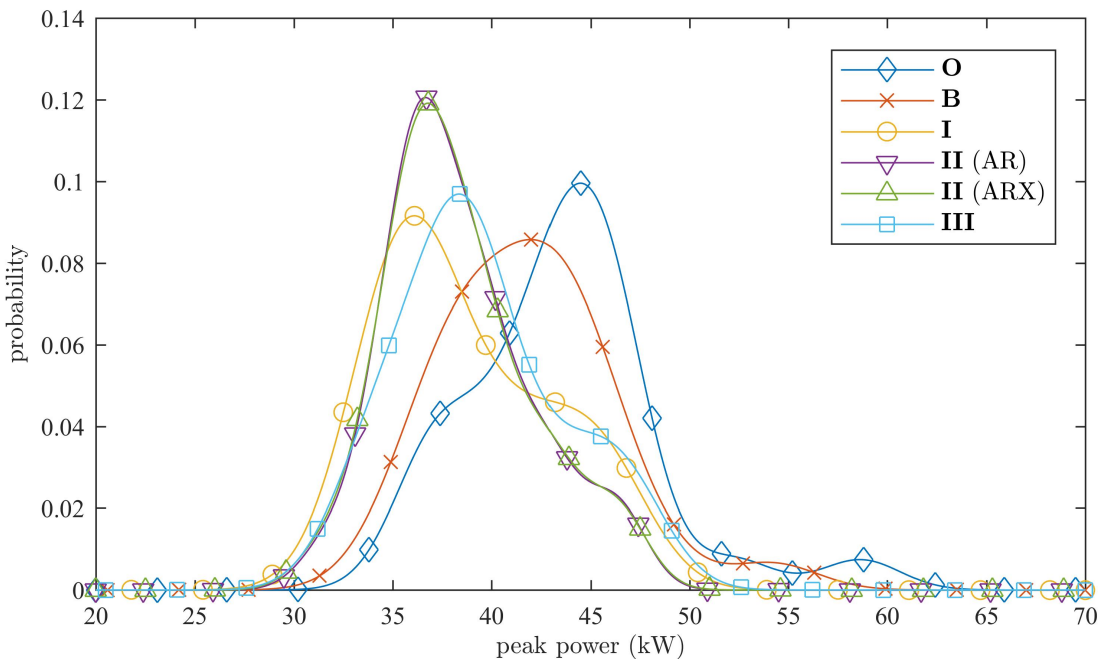


Figure 4.8: Probability of load peak when using realistic forecasts.

Using standard kernel density estimation, the PDF was plotted in Figure 4.8. The data used to generate these plots is the same data shown in Figure 4.7. Now, the probability of a peak power occurring is linked to the magnitude of this peak. It can be seen that case **O** has the highest probability around a load peak of 45kW, whilst case **B** has its highest probability around a load peak of 42kW. This indicates that even the pure half-hourly ESMU schedule had a positive impact on reducing load peaks. When adjusting the schedule based with the use of the proposed dynamic control, this peak was lowered further.

Figure 4.9 takes this analysis even further, where only the difference in peak load to the original case, case **O**, was plotted. Now, ESMU impact can easily be seen, since a high probability of positive peak load reduction indicates a beneficial impact of the

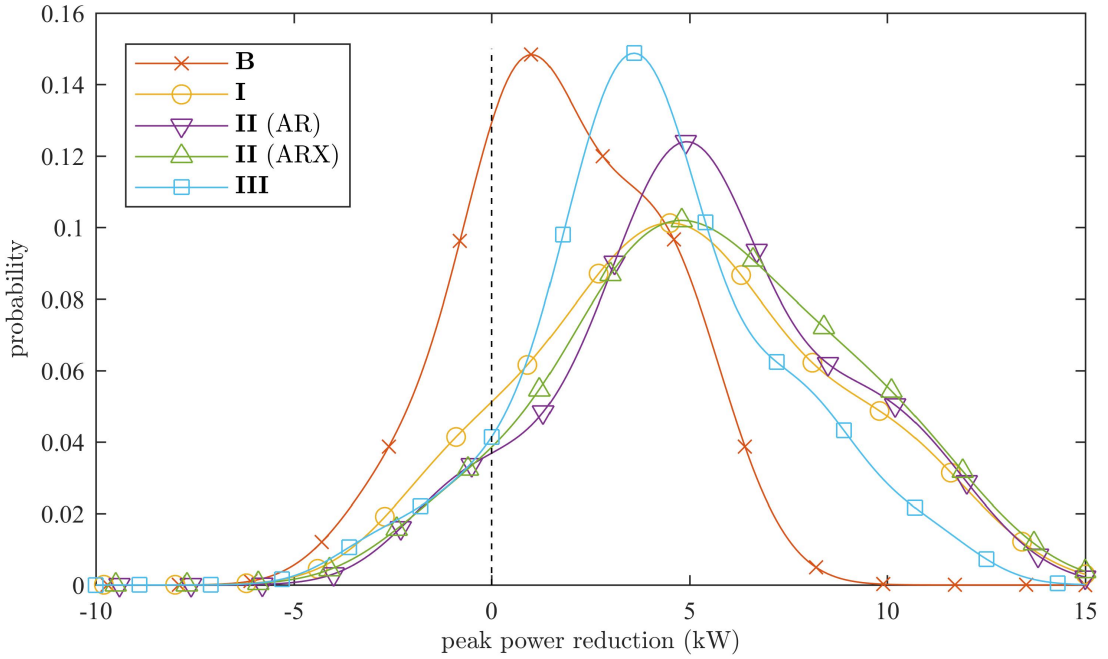


Figure 4.9: Probability of load peak reduction when using realistic forecasts.

ESMU operation, whereas a negative peak load reduction (i.e. increased peak load) indicates a worsening performance. As expected, case **O** has a slight positive impact on the system, whilst a cumulative probability of more than 25% (i.e. area under curve of case **O** to the left of 0kW) suggests that the peak might be worsened one in four times. Using dynamic control with its simplest prediction method however, i.e. case **I**, lowered this probability to only 11.8%, with the AR model in case **II** performing best at only 8%.

Beside the reduced probability of missing or worsening peak load, the probability of having a larger positive impact is also increased when using the dynamic control. Whilst the probability of reducing load peaks by 1.7kW or more was at 50% for case **B**, case **I** increased this probability to 77.7%, case **II** to 84.5 5% (AR) / 83.1% (ARX), and case **III** to 79.8%. When comparing the three dynamic control cases with each other, Figure 4.9 indicates that case **II** using an AR model for MPC performed best at reducing peak loads.

4.6 Summary

In this chapter a dynamic control method is proposed that adjusts half-hourly Energy Storage Management Unit (ESMU) schedules on a sub-half-hourly basis in order to minimise otherwise neglected sub-half-hourly power spikes without risking a shortage or surplus of ESMU stored energy. Reason behind this were, that traditional load forecasts usually lack in accuracy and temporal resolution, making it hard to schedule ESMU in an optimal manner. Recent research implements derivatives of Set-Point Control (SPC), which is typically guided by a short-term Model Predictive Control (MPC) mechanisms to address both load volatility and to prepare ESMU for upcoming load spikes. However, those approaches do not utilise the information, quality and operational certainty that would be provided by load forecasts and ESMU schedules. The proposed dynamic control addresses this shortcoming by approaching the problem from the opposite direction: i.e. it adjusts a predetermined ESMU schedule based on two linked PID compensators.

The first compensator was designed to minimise the deviation form the prescheduled ESMU's State Of Charge (SOC) profile, and the second compensator was designed to minimise the load volatility. For the latter compensator to operate however, a short-term predictive model was used to estimate the load power in the immediate future, i.e. the next time step. Different light weight and well established mechanisms were used to implement this predictive model in order to assure real-time operation and robustness of the system.

Simulating these different models to guide schedule adjustments yielded positive results for each test case that used dynamic control. In fact, dynamic control outperformed the baseline case in nearly every case, where the baseline case is the scenario of applying a traditional half-hourly ESMU schedule in an off-line manner. Whilst this baseline operation did also increase peak load under severe forecast errors, the best performing dynamic control case was able to reduce the probability of increasing

peak loads by a factor of 3.12. It is worth mentioning, that this improvement was yielded despite the fact that all cases used the same underlying and imperfect ESMU schedule.

The work presented here, demonstrates how imperfect ESMU schedules may still be used to yield more beneficial impacts. With future deployment of ESMU throughout Low-Voltage power distribution networks, advanced ESMU control is necessary to assure their impact is in accordance to volatile demand. Control, like the one proposed here, can take into account the complete range of demand volatility and, when implemented correctly, defers or avoid network reinforcement altogether. This is particularly true since ongoing electrification of UK heat and transport sectors change consumers' electricity consumption and increase stress on power distribution networks.

Chapter 5

Effects of Desynchronising Information Propagation when Distributing Smart-Charging

5.1 Overview

In previous chapters the the question regarding how one can optimally control a single battery energy storage has been addressed. It was shown that half-hourly forecasts can be used to predict demand due to customer behaviours. With this knowledge, Battery Energy Storage Systems (BESS) can be scheduled shave peak load in order to avoid overloading the already stressed system. However, sub-half-hourly issues cannot be addressed by traditional BESS schedules, which is why two successive sub-half-hourly power adjustment methods were developed. The first method improved network operation by focusing on the underlying three-phase network topology, whilst strictly following the underlying half-hourly SOC plan. The second method on the other hand alleviated this constraint by adjusting total power flow instead. Benefits from using BESS schedules complement dynamic feedback and yield improved power

profiles with reduced peak load.

The logical next step is to take such schedules and apply them to multiple, distributed batteries. To prevent the negative impact from battery charging, particularly when dealing with the home-charging of Electric Vehicles (EVs), their charging scheduling needs to be coordinated. As already discussed in Section 2, multiple EV scheduling methods exist. Approaches propose demand prioritisation, multi-tariff environments or other game theory approaches to maximise global benefit whilst reducing the individual's disadvantages. Here, coordination of charge scheduling signals becomes a vital requirement to react to other EV's charging plans. This statement is commonly acknowledged, yet in a system of distributed scheduling the assumption of perfect knowledge about the environment no longer holds.

In fact, during distributed scheduling, control instructions that may be broadcasted by each EV, to inform all other EVs in the system of updated charging plan, need not or cannot be sent at certain times unless message synchronisation is guaranteed. Therefore, this chapter studies the impact of desynchronising message propagation by adding transmission jitter to the updating broadcasts. Here, EVs are used since their so called “smart-charging” behaviour is intended to avoid home-charging related load spikes. A robust smart-charging algorithm to determine multiple EVs' charging schedule is presented and executed in both a synchronised and a desynchronised messaging scenario. This smart-charging algorithm is designed to prevent aggregated demand, due to EV charging, from reaching certain peak power. A Multi-Agent System (MAS) is implemented to perform the distributed scheduling using the Foundation for Intelligent Physical Agents (FIPA) compliant agents.

Results show how synchronised scheduling leads to expected outcomes that have also been established in literature. However, adding jitter to message broadcasting significantly changes the same algorithm's behaviour. Differences regarding rate of convergence and criteria for stability are most noticeable. In this chapter, a brief

summary of obtaining simplistic EV demand and how this is used in a typical (i.e. robust and converging) scheduling algorithm is detailed in Section 5.2. Next, the distributed control and the reasons for choosing a multi-agent system is presented in Section 5.3, alongside the two cases for synchronised and desynchronised information propagation. Section 5.4 presents and discusses the results from these two cases, upon which conclusions is drawn and presented in Section 5.5.

5.2 Coordination of EV charging

In this section, an algorithm for EV charging is presented, which is later implemented in both a synchronised and desynchronised case. Real load data is used in combination with EV demand to evaluate the performance of the algorithm at preventing new power spikes from occurring. Convergence of the algorithm is studied and convergence criteria as well as rate of convergence are presented, too.

The structure of this section is as follows. First, the means and assumptions for calculating EV demand is defined. Then the real load data is introduced and explained. The EV scheduling algorithm is introduced next, before the performance parameters are presented.

5.2.1 EV Demand

EVs were modelled as loads that, over the course of a scheduling horizon, T_{sch} , each need to consume a certain amount of energy, E_u , to simulate charging their batteries. Each EV, i.e. u , is part of a fleet of charging and coordinated EVs, i.e. $u \in [1, \dots, U]$. Unlike typical loads (e.g. households), EVs do not have a predetermined load profile in this simulation and are therefore flexible to schedule their demand at each time t a $p_{\text{EV},u,n}(t)$, where $p_{\text{EV},u,n}(t) \in \mathbf{p}_{\text{EV},u,n}$. In other words, they can autonomously assign their own charging plan over the predetermined number of future time-slots, T_{sch} .

Due to limitations in on-board power electronics, each EV's maximum charge rate, $P_{\max,u}$, is restricted and may not be exceeded. Equally, in order to meet the EV's charging demand over the scheduling horizon, T_{sch} , a soft minimum charging power, $P_{\min,u}$ is also introduced:

$$P_{\min,u} := \frac{E_u}{H} \quad (5.1)$$

Although the upper limit is hard, i.e. caused by technical restrictions, this lower limit is a necessity to initiate the scheduling procedure, which will become apparent when the scheduling algorithm is explained. Using MAS, EVs utilise their broker agents to purchase energy quantities for each time-slot, t , and also sell or "undo" some of the already acquired energy quantities if it contributed towards a new load spike.

5.2.2 Base Load

To represent real power consumption in simulations, historic customer load profiles were used in this work [62]. This dataset consisted of 7392 demand readings for 543 loads, which were sampled at half-hourly period, i.e. $\Delta t = 0.5$ hours. A single scheduling horizon was defined as one day, therefore $T_{\text{sch}} = 48$ samples.

In this context, each household, i.e. physical entity, dispatches its broker agents to order the household's daily energy demand; therefore it a scenario with some foresight is assumed. After having issued this energy request, the entire network demand is known to the supplier and can be relayed to all broker agents when they query for it. This ability is exploited when scheduling and negotiating the unknown EV charging profiles. More specifically, all households' broker agents communicate with the supplier's broker agents to optimally embed their charging profiles, $p_{\text{EV},u,n}(t)$, within this aggregated base load.

5.2.3 Scheduling Algorithm

For the EV charging coordination strategy, an algorithm was designed that generates optimised charging profiles for each EV. Here, optimality implies that when adding all aggregated charging profiles to the network's base demand, $p_{\text{base}}(t)$, no additional spikes occur in the resulting demand profile, i.e. $p_{\text{base}}(t) + \sum_{u=1}^U p_{EV,u,N}(t)$. These profiles were generated by repetitively querying for the network's base load, adjusting individual EV charging profiles, and resubmitting the adjusted charging profile. As already stated, the common assumption when designing such a scheduling algorithm is that all scheduling entities are synchronised, i.e. wait for each other, before querying for the network's base load. For visualisation, the message exchange bewteen two loads and a supplier including a synchronisation time is shown in Figure 5.1.

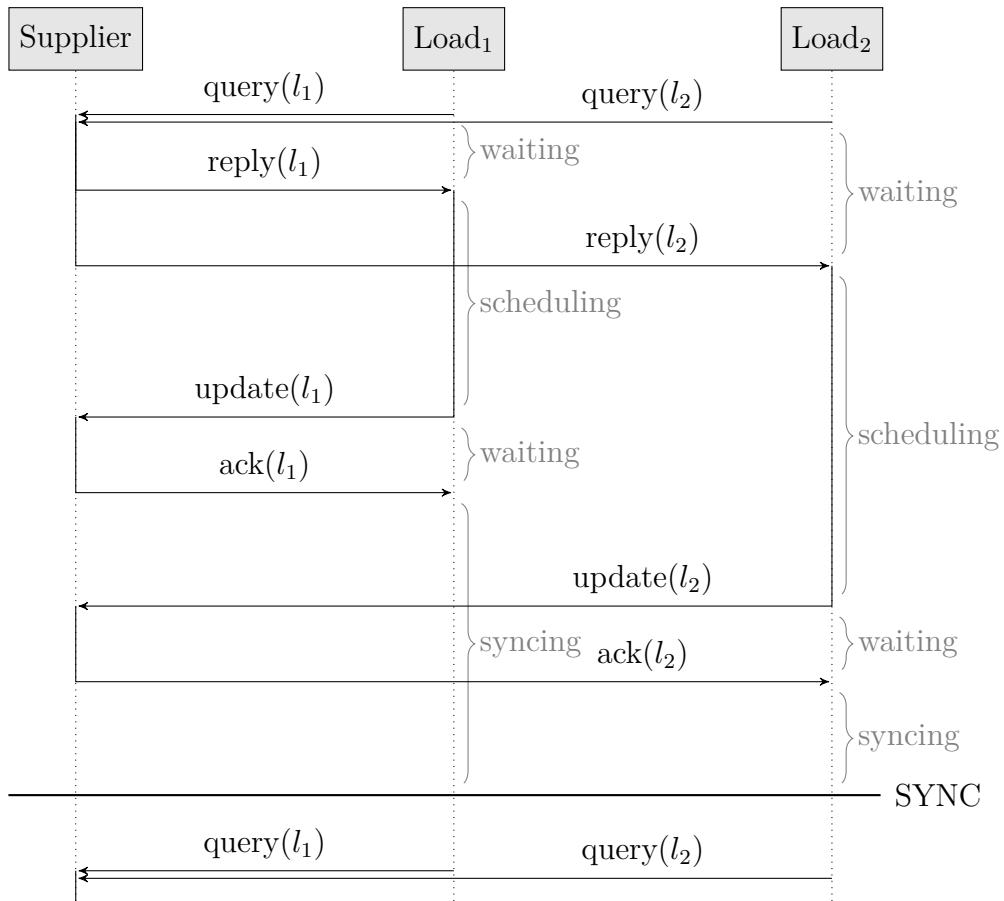


Figure 5.1: Agent synchronisation before re-scheduling their EVs charging profile.

In this figure, the horizontal arrows indicate messages being sent from loads (i.e. EV agents) to a supplier and vertical lines indicate processing or idle time. Shown within Figure 5.1 is a single scheduling iteration, which can be broken into the sub-processes of: querying, scheduling, updating and synchronising. From top to bottom, the sequential execution of these sub-processes is as follows:

First, both $load_1$ and $load_2$ query the supplier for the currently known network load (i.e. $query(l_1)$ and $query(l_2)$). This network load is used to schedule their power profiles to “fill valleys”, i.e. only charge EVs during periods of low demand. Upon receipt of a reply from the energy supplier (i.e. $reply(l_1)$ and $reply(l_2)$), both loads immediately start scheduling their profiles. In the example above, $load_1$ found a solution before $load_2$ and can therefore inform the supplier about its intended load profile sooner, by sending an update (i.e. $update(l_1)$) to the supplier. Subsequently querying the supplier for an updated network load would be premature, since the other load (i.e. $load_2$) has not yet generated and updated its load profile. Therefore, a synchronisation mechanism had to be used, forcing $load_1$ to wait until all loads have sent updates to the supplier. Here, $load_1$ waits until $load_2$ has sent an update and the corresponding profile was acknowledged by the supplier (i.e. $ack(l_2)$). Only after this had happened, a synchronisation event would be triggered (i.e. $SYNC$ event). After this synchronisation event, the next algorithm iteration is initiated and the procedure repeats. Since all subsequent iterations are similar to the one shown in Figure 5.1, only the two querying messages of the second iteration are shown.

Although the timing and message exchange has been defined, the mechanism to allocate and reallocate charging powers in order to achieve a valley filling behaviour has not yet been defined. This behaviour is shown in Figure 5.2, where several iterations numbered n are shown, and for each subsequent iteration, some amount of prescheduled power is reallocated to different time-slots.

For every iteration in Figure 5.2, charging profiles are added onto a base network

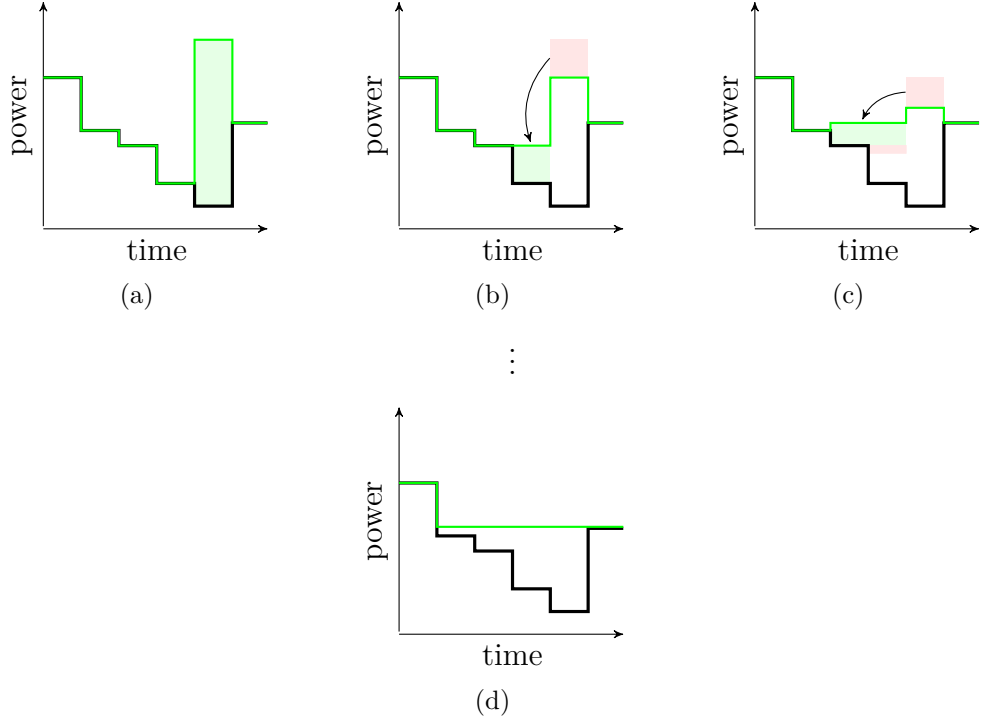


Figure 5.2: Charging power (green line) allocation on top of base network load (black line) for valley-filling behaviour. Here $n = 1$ for Fig. 5.2a, $n = 2$ for Fig. 5.2b, $n = 3$ for Fig. 5.2c, and $n = N$ for Fig. 5.2d.

load, $\mathbf{p}_{base,n}$, where $p_{base,n}(t) \in \mathbf{p}_{base,n}$. This base load is shown as the bold black line and does not change throughout EV scheduling. For any iteration, the charging profile during iteration number n , for EV u , is defined as \mathbf{p}_n (where $p_{u,n}(t) \in \mathbf{p}_n$). During the first iteration however, i.e. Figure 5.2a where $n = 1$, this charging profile is determined by assigning the maximum EV charging power to the time-slots of lowest load, until the total EV energy demand is met, i.e. at time-slot τ where $\tau = \text{argmin}(\mathbf{p}_{base})$. Since all EVs schedule their profiles based upon the same knowledge of $\mathbf{p}_{base,n}$, the aggregated charging power is likely to generate a new spike. This spike is seen on an updated or temporary demand profile, $\hat{\mathbf{p}}_{base,n}$, where $\hat{p}_{base,n}(t) \in \hat{\mathbf{p}}_{base,n}$ is defined as:

$$\hat{p}_{base,n}(t) := p_{base,n}(t) + \sum_{u=1}^U p_{u,n}(t) \forall t \text{ and } \forall n \quad (5.2)$$

For the next iteration $n + 1$, i.e. Figure 5.2b where $n = 2$, a proportion of

the previously scheduled power vector $\mathbf{p}_{\text{EV},n-1}$ is “undone”. Subsequently, the spike in the resulting $\hat{\mathbf{p}}_{\text{base},n}$ is reduced, yet the energy that has been undone needs to be reallocated. The amount by which $\mathbf{p}_{\text{EV},n-1}$ is reduced is determined by the “*undoing*” parameter α , where $\alpha \in [0, 1)$. A new reduced or temporary charging vector $\hat{p}_{\text{EV},u,n}(t)$ is therefore defined as:

$$\hat{p}_{\text{EV},u,n}(t) := p_{\text{EV},u,n-1}(t)\alpha \quad (5.3)$$

Using this temporary charging power, the regained or temporary energy demand, $\hat{E}_{u,n}$, that needs to be reallocated, can also be defined:

$$\hat{E}_{u,n} := E_u - \sum_{\tau=1}^{T_{\text{sch}}} \hat{p}_{\text{EV},u,n}(\tau) \Delta t \quad \forall u \text{ and } n > 1 \quad (5.4)$$

To include the first iteration of the algorithm, Equation 5.4 needs to be expanded to redefine $\hat{E}_{u,n}$ for all possible algorithm iterations n :

$$\hat{E}_{u,n} := \begin{cases} E_u & \text{if } n = 1 \\ E_u - \sum_{\tau=1}^{T_{\text{sch}}} \hat{p}_{\text{EV},u,n}(\tau) \Delta t & \text{otherwise} \end{cases} \quad \forall u \text{ and } \forall n \quad (5.5)$$

Following the similar procedure as for the first iteration, $\hat{E}_{u,n}$ needs to be allocated to different time-slots, where the rule of performing the power allocation is defined as:

$$p_{\text{EV},u,n}(\tau) := \begin{cases} \hat{p}_{\text{EV},u,n-1} + \frac{\hat{E}_{u,n}}{\Delta t} \beta & \text{if } \hat{p}_{\text{EV},u,n-1} + \frac{\hat{E}_{u,n}}{\Delta t} \beta \leq P_{\max,u} \\ P_{\max,n} & \text{otherwise} \end{cases} \quad \forall u \quad (5.6)$$

where $\tau = \text{argmin}(\hat{\mathbf{p}}_{\text{base},n})$ and $n > 1$

$$\text{s.t. } \hat{p}_{\text{EV},u,n-1} + \frac{\hat{E}_{u,n}}{\Delta t} \beta \geq P_{\min,u}$$

Here, a maximum “allocation” parameter, β , where $\beta \in (0, 1]$ limits the power that may be allocated to any successive time-slot, τ . To not exceed the EV’s maximum charging power, any value in the charging vector, $\mathbf{p}_{\text{EV},u,n}$, is capped to $P_{\max,u}$. If β is chosen as one, then the undone energy is allocated as quickly as possible. For smaller values of β on the other hand, the undone charge is reallocated in smaller portions. Since EV scheduling takes place over a finite scheduling horizon, T_{sch} , a constraint was added in Equation 5.6. This was done to assure that the temporary energy demand equates after some charging power was assigned to every time-slot of $\mathbf{p}_{\text{EV},u,n}$.

Any following algorithm iteration, i.e. $n > 2$ as shown in Figure 5.2c, the entire charging profile is adjusted and spread further over the base load, \mathbf{p}_{base} . In the end, i.e. when $n = N$, the ideal EV charging profiles aggregate with the base load in such a way, that the resulting network load has an optimally filled valley. This valley filling behaviour is achieved with the “undoing” and “allocation” of EV charging power from one algorithm iteration to the next. Regardless of the final network load’s shape, the algorithm terminates when the final iteration is reached, i.e. $n = N$. Rate of convergence of the algorithm differs based upon the choice of α and β values. However, convergence is in fact guaranteed when selecting values of $\alpha < 1$ and $\beta < 1$, since the algorithm satisfies the D’Alembert Criterion in those cases.

To summarise this section, the complete EV scheduling algorithm was developed by: 1. defining the message exchange and synchronisation mechanism, which is shown in Figure 5.1; 2. formulating the initial and successive “undoing” of charging power, as shown in Equation 5.3; and 3. defining the iterative update and “allocation” of the temporary energy demand, as defined in Equation 5.5. For clarity, the this smart charging algorithm’s pseudocode, performing the complete valley filling procedure, has been included in Algorithm 1.

```

Data:  $p_{base,n}$ ,  $E_u$ ,  $P_{max,u}$ ,  $P_{min,u}$ ,  $\Delta t$ ,  $T_{sch}$ 
Result:  $p_{EV,u,n}$ 

1 for  $n \leftarrow 1$  to  $N$  do
2   // Query for base load
3    $p_{base,n} \leftarrow \text{query}();$ 
4   // Forward and undo previous schedule
5   if  $n > 1$  then
6     |  $p_{EV,u,n} \leftarrow p_{EV,u,n-1}\alpha;$ 
7   else
8     |  $p_{EV,u,n} \leftarrow [0, 0, \dots, 0];$ 
9   end
10  // Determine unallocated energy
11   $\hat{E}_{u,n} = E_u - \sum_{\tau=1}^{T_{sch}} p_{EV,u,n}(\tau)\Delta t;$ 
12  // Fill valley
13  for  $\tau \leftarrow argmin(p_{base,n})$  to  $argmax(p_{base,n})$  do
14    if  $p_{EV,u,n}(\tau) + \frac{\hat{E}_{u,n}}{\Delta t}\beta \leq P_{max,u}$  then
15      |  $p_{EV,u,n}(\tau) \leftarrow p_{EV,u,n}(\tau) + \frac{\hat{E}_{u,n}}{\Delta t}\beta;$ 
16    else
17      |  $p_{EV,u,n}(\tau) \leftarrow P_{max,u};$ 
18    end
19     $\hat{E}_{u,n} = E_u - \sum_{\tau=1}^{T_{sch}} p_{EV,u,n}(\tau)\Delta t;$ 
20    // Once EV profile is found, send update
21    if  $\hat{E}_{u,n} = 0$  then
22      |  $\text{update}(p_{EV,u,n});$ 
23      |  $\text{break}();$ 
24    end
25  end
26   $\text{synchronising}();$ 
27 end

```

Algorithm 1: Robust valley filling algorithm for a single EV in

5.3 Distributed Systems

As discussed in the literature review in Chapter 2, several mechanisms exist to decentralise control of DERs. Due to their reactivity, pro-activeness and social ability, the Multi Agent System (MAS) distinguished itself from traditional software and hardware systems, which is also why it was also chosen for the coordination of smart EV charging. Several agent package implementations exist, each following different interaction paradigms. These paradigms include “Belief, Desire and Intention” (BDI), neutral behaviour or other specialised functionality [63]. From this catalogue of MAS paradigms, the Java Agent Development Framework (JADE) was chosen, since it natively implements the Foundation for Intelligent Physical Agent (FIPA) specification [64, 65]. Furthermore, JADE is an application independent package that has become quite popular, as seen by the increasing number of publications [66, 67, 68, 69, 70].

In this work, multiple virtual trading agents are used to negotiate their corresponding EV’s charging profile with other trading agents. Tying virtual agents to a physical entity is not new [71, 72, 73, 74], yet in previous work these agents directly controlled the entity whilst the agents in the presented work negotiate schedules that will be applied after schedule ratification. So called “broker” agents, following the Brokering Interaction Protocol (BIP), are implemented to facilitate this trading process. The brokers communicate with each other by following the Contact-Net Protocol (CNP). In addition, all FIPA protocols are based on the FIPA Agent Communication Language (ACL) that is required to communicate over a shared telecommunications infrastructure, and possibly include different agent packages, too. High level explanations of all protocols that were used in this implementation of FIPA agents are included in Appendix B. In this work, each broker is linked to a single EV and negotiates its charging profile over the aforementioned scheduling horizon, T_{sch} . This link is shown in Figure 5.3.

In the example in Figure 5.3, a single supplier with two brokers (one for selling

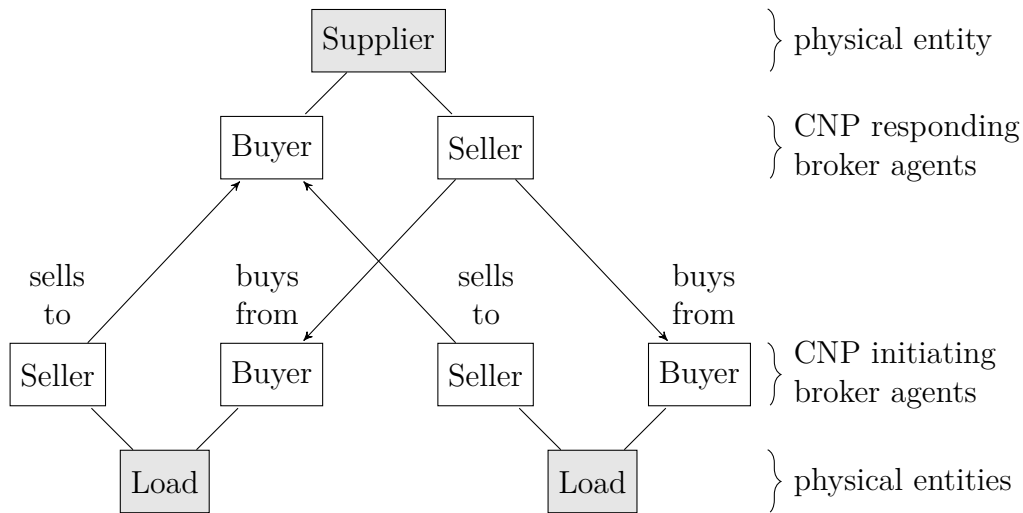


Figure 5.3: A simplified MAS structure containing virtual seller and buyer agents (white), that negotiate power/charging profiles for physical entities (grey).

and one for buying, i.e. “undoing”, energy) acts as the energy source, and two loads represent the charging EVs that dispatch their two brokers (i.e. to “allocate” and “undo” charging demand). With this kind of system architecture, charging spikes are designed to be mitigated, since all loads and their corresponding brokers execute the previously defined smart charging algorithm.

Since the architecture of MAS has now been defined, the means of implementing and desynchronising them is explained. Subsequently, all case studies and metrics that are used to assess the MAS performance are defined.

5.3.1 MAS Implementation

The MAS was written in Java and implemented on a parallel compute cluster (i.e. the *HTCondor* cluster at the former “*School of Systems Engineering*”). Here,

5.3.2 MAS Desynchronisation

Operating the agents in a desynchronised manner can be achieved in two distinct ways. Either, any idle state that is interrupted by the synchronising signal is removed, or

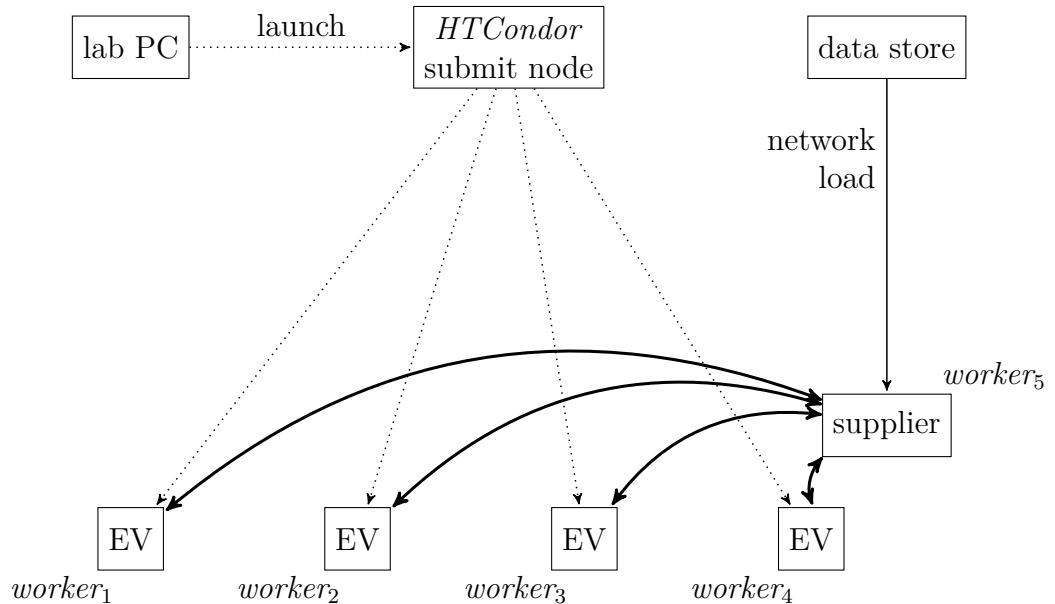


Figure 5.4: The implementation of FIPA on *HTCondor*.

agents operate within a fixed execution loop and continue after each agent's loop timer expired.

The former option would be the easier option to implement

5.3.3 Cases and Performance Metrics

5.4 Results and Discussion

5.5 Summary

Chapter 6

Cooperative Battery Operation of without Communications Infrastructure Needs

M. Zangs, P. Adams, et.al., “Distributed Energy Storage Control for Dynamic Load Impact Mitigation,” Energies, vol. 9, no. 8, p. 647, August 2016

— Available: <https://dx.doi.org/10.3390/en9080647>

T. Yunusov, M. J. Zangs, et.al., “Control of Energy Storage,” Energies, vol. 7, no 10, p. 1010, July 2017

— Available: <https://doi.org/10.3390/en10071010>

6.1 Overview

This chapter addresses the question how multiple batteries could be coordinated collectively...

6.2 Summary

Chapter 7

Conclusion

7.1 Overview of Main Findings

7.2 Knowledge Contribution

7.3 Research Limits

7.4 Future Work

Bibliography

- [1] National Grid, “Future Energy Scenarios 2016,” Tech. Rep. July, 2016.
- [2] National Grid, “Future Energy Scenarios 2015,” Tech. Rep. July, 2015.
- [3] D. Manz, R. Piwko, and N. Miller, “Look before you leap: The role of energy storage in the grid,” *IEEE Power Energy Mag.*, vol. 10, no. 4, pp. 75–84, 2012.
- [4] M. Kleinberg, N. S. Mirhosseini, F. Farzan, J. Hansell, A. Abrams, W. Katzenstein, J. Harrison, and M. A. Jafari, “Energy storage valuation under different storage forms and functions in transmission and distribution applications,” *Proc. IEEE*, vol. 102, no. 7, pp. 1073–1083, 2014.
- [5] Department for Business Enterprise and Regulatory (DBER) and Department for Transport (DfT), “Investigation into the Scope for the Transport Sector to Switch to Electric Vehicles and Plug- in Hybrid Vehicles,” tech. rep., 2008.
- [6] G. Strbac, C. K. Gan, M. Aunedi, V. Stanojevic, P. Djapic, J. Dejvises, P. Mancarella, A. Hawkes, D. Pudjianto, D. Openshaw, S. Burns, P. West, D. Brogden, A. Creighton, and A. Claxton, “Benefits of Advanced Smart Metering for Demand Response based Control of Distribution Networks,” Tech. Rep. April 2010, 2010.
- [7] F. R. Kalhammer, “Energy-Storage Systems,” *Sci. Am.*, vol. 241, no. 6, pp. 42–51, 1979.

- [8] J. Eyer and G. Corey, “Energy Storage for the Electricity Grid : Benefits and Market Potential Assessment Guide,” tech. rep., Sandia National Laboratories, 2010.
- [9] E. Barbour, “Energy Storage Sense,” 2015.
- [10] E. Barbour, I. A. G. Wilson, J. Radcliffe, Y. Ding, and Y. Li, “A review of pumped hydro energy storage development in significant international electricity markets,” *Renew. Sustain. Energy Rev.*, vol. 61, pp. 421–432, 2016.
- [11] The Economist, “Packing some power,” *Econ.*, 2012.
- [12] F. R. McLarnon and E. J. Cairns, “Energy Storage,” *Annu. Rev. Energy*, vol. 14, pp. 241–271, 1989.
- [13] H. Ibrahim, A. Ilinca, and J. Perron, “Energy storage systems-Characteristics and comparisons,” *Renew. Sustain. Energy Rev.*, vol. 12, no. 5, pp. 1221–1250, 2008.
- [14] H. Chen, T. N. Cong, W. Yang, C. Tan, Y. Li, and Y. Ding, “Progress in electrical energy storage system: A critical review,” *Prog. Nat. Sci.*, vol. 19, no. 3, pp. 291–312, 2009.
- [15] I. Hadjipaschalidis, A. Poullikkas, and V. Efthimiou, “Overview of current and future energy storage technologies for electric power applications,” *Renew. Sustain. Energy Rev.*, vol. 13, no. 6-7, pp. 1513–1522, 2009.
- [16] X. Luo, J. Wang, M. Dooner, and J. Clarke, “Overview of current development in electrical energy storage technologies and the application potential in power system operation,” *Appl. Energy*, vol. 137, pp. 511–536, 2015.

- [17] W. Jewell and R. Ramakumar, “The effects of moving clouds on electric utilities with dispersed photovoltaic generation,” *IEEE Trans. Energy Convers.*, vol. EC-2, no. 4, pp. 570–576, 1987.
- [18] Ofgem, “RIIO - Electricity Distribution - Annual Report 2015-16,” Tech. Rep. February, 2017.
- [19] Ofgem, “December 2013 UK Storms Review – impact on electricity distribution customers,” Tech. Rep. March, 2014.
- [20] HM Government, *The UK Low Carbon Transition Plan: National strategy for climate and energy*. No. July 2009, 2009.
- [21] Royal Academy of Engineering, *Generating the Future: UK energy systems fit for 2050*. 2010.
- [22] A. Poghosyan, D. V. Greetham, S. Haben, and T. Lee, “Long term individual load forecast under different electrical vehicles uptake scenarios,” *Appl. Energy*, vol. 157, pp. 699–709, 2014.
- [23] I. Richardson, M. Thomson, D. Infield, and C. Clifford, “Domestic electricity use: A high-resolution energy demand model,” *Energy Build.*, vol. 42, no. 10, pp. 1878–1887, 2010.
- [24] T. Yunusov, D. Frame, W. Holderbaum, and B. Potter, “The impact of location and type on the performance of low-voltage network connected battery energy storage systems,” *Appl. Energy*, vol. 165, pp. 202–213, 2016.
- [25] G. Ault, D. Frame, N. Hughes, and N. Strachan, “Electricity Network Scenarios for Great Britain in 2050,” tech. rep., 2008.

- [26] G. P. Harrison, A. Piccolo, P. Siano, and a. R. Wallace, “Exploring the trade-offs between incentives for distributed generation developers and DNOs,” *IEEE Trans. Power Syst.*, vol. 22, no. 2, pp. 821–828, 2007.
- [27] M. J. Zangs, P. B. E. Adams, T. Yunusov, W. Holderbaum, and B. A. Potter, “Distributed energy storage control for dynamic load impact mitigation,” *Energies*, vol. 9, no. 8, 2016.
- [28] T. van der Klauw, J. Hurink, and G. Smit, “Scheduling of Electricity Storage for Peak Shaving with Minimal Device Wear,” *Energies*, vol. 9, p. 465, 2016.
- [29] D. M. Greenwood, N. S. Wade, P. C. Taylor, P. Papadopoulos, and N. Heyward, “Storage and Real-Time Thermal Ratings to Defer Network Reinforcement,” *IEEE Trans. Sustain. Energy*, vol. 8, no. 1, pp. 374–384, 2017.
- [30] N. S. Wade, P. C. Taylor, P. D. Lang, and P. R. Jones, “Evaluating the benefits of an electrical energy storage system in a future smart grid,” *Energy Policy*, vol. 38, no. 11, pp. 7180–7188, 2010.
- [31] O. Palizban and K. Kauhaniemi, “Energy storage systems in modern grids — Matrix of technologies and applications,” *J. Energy Storage*, vol. 6, pp. 248–259, 2016.
- [32] Y. Yang, H. Li, A. Aichhorn, J. Zheng, and M. Greenleaf, “Sizing strategy of distributed battery storage system with high penetration of photovoltaic for voltage regulation and peak load shaving,” *IEEE Trans. Smart Grid*, vol. 5, no. 2, pp. 982–991, 2014.
- [33] C. J. Bennett, R. a. Stewart, and J. W. Lu, “Development of a three-phase battery energy storage scheduling and operation system for low voltage distribution networks,” *Appl. Energy*, vol. 146, pp. 122–134, 2015.

- [34] L. Wang, D. Liang, A. F. Crossland, P. C. Taylor, D. Jones, and N. S. Wade, “Coordination of Multiple Energy Storage Units in a Low Voltage Distribution Network,” *IEEE Trans. Power Syst.*, vol. 6, no. 6, pp. 2906–2918, 2015.
- [35] A. Oudalov, R. Cherkaoui, S. Member, and A. Beguin, “Sizing and Optimal Operation of Battery Energy Storage System for Peak Shaving Application,” in *2007 IEEE Lausanne Power Tech*, pp. 621–625, 2007.
- [36] K. Baker, G. Hug, and X. Li, “Energy Storage Sizing Taking Into Account Forecast Uncertainties and Receding Horizon Operation,” *IEEE Trans. Sustain. Energy*, vol. 8, pp. 331–340, jan 2017.
- [37] Y. Wang, X. Lin, and M. Pedram, “Adaptive control for energy storage systems in households with photovoltaic modules,” *IEEE Trans. Smart Grid*, vol. 5, no. 2, pp. 992–1001, 2014.
- [38] M. Rowe, T. Yunusov, S. Haben, C. Singleton, W. Holderbaum, and B. Potter, “A Peak Reduction Scheduling Algorithm for Storage Devices on the Low Voltage Network,” *IEEE Trans. Smart Grid*, vol. 5, no. 4, pp. 2115–2124, 2014.
- [39] S. Haben, J. Ward, D. Vukadinovic Greetham, C. Singleton, and P. Grindrod, “A new error measure for forecasts of household-level, high resolution electrical energy consumption,” *Int. J. Forecast.*, vol. 30, no. 2, pp. 246–256, 2014.
- [40] T. Gybel, L. F. S. Larsen, K. Edlund, and J. Bagterp, “Model predictive control technologies for efficient and flexible power consumption in refrigeration systems,” *Energy*, vol. 44, no. 1, pp. 105–116, 2012.
- [41] M. C. Such and C. Hill, “Battery energy storage and wind energy integrated into the Smart Grid,” in *2012 IEEE PES Innov. Smart Grid Technol.*, pp. 1–4, 2012.

- [42] W. Li and Z. G. Zhang, “Based on time sequence of ARIMA model in the application of short-term electricity load forecasting,” *ICRCCS 2009 - 2009 Int. Conf. Res. Challenges Comput. Sci.*, pp. 11–14, 2009.
- [43] H. Nie, G. Liu, X. Liu, and Y. Wang, “Hybrid of ARIMA and SVMs for short-term load forecasting,” *Energy Procedia*, vol. 16, no. PART C, pp. 1455–1460, 2011.
- [44] T. Sannomiya, H. Hayashi, T. Ishii, and R. Ikeda, “Test results of compensation for load fluctuation under a fuzzy control by a 1 kWh/1 MW SMES,” *IEEE Trans. Appl. Supercond.*, vol. 11, no. 1, pp. 1908–1911, 2001.
- [45] S. X. Chen, H. B. Gooi, and M. Q. Wang, “Solar radiation forecast based on fuzzy logic and neural networks,” *Renew. Energy*, vol. 60, pp. 195–201, 2013.
- [46] H. Xia, H. Chen, Z. Yang, F. Lin, and B. Wang, “Optimal energy management, location and size for stationary energy storage system in a metro line based on genetic algorithm,” *Energies*, vol. 8, no. 10, pp. 11618–11640, 2015.
- [47] H. Liu, H. Tian, X. Liang, and Y. Li, “New wind speed forecasting approaches using fast ensemble empirical model decomposition, genetic algorithm, Mind Evolutionary Algorithm and Artificial Neural Networks,” *Renew. Energy*, vol. 83, pp. 1066–1075, 2015.
- [48] S. A. Kalogirou, E. Mathioulakis, and V. Belessiotis, “Artificial neural networks for the performance prediction of large solar systems,” *Renew. Energy*, vol. 63, pp. 90–97, 2014.
- [49] H. Quan, D. Srinivasan, and A. Khosravi, “Short-term load and wind power forecasting using neural network-based prediction intervals,” *IEEE Trans. Neural Networks Learn. Syst.*, vol. 25, no. 2, pp. 303–315, 2014.

- [50] D. Lee and R. Baldick, “Short-term wind power ensemble prediction based on gaussian processes and Neural networks,” *IEEE Trans. Smart Grid*, vol. 5, no. 1, pp. 501–510, 2014.
- [51] H. Pezeshki, P. Wolfs, S. Member, and G. L. S. Member, “A Model Predictive Approach for Community Battery Energy Storage System Optimization,” in *PES Gen. Meet. — Conf. Expo. 2014 IEEE*, pp. 27–31, 2014.
- [52] A. G. R. Vaz, B. Elsinga, W. G. J. H. M. van Sark, and M. C. Brito, “An artificial neural network to assess the impact of neighbouring photovoltaic systems in power forecasting in Utrecht, the Netherlands,” *Renew. Energy*, vol. 85, pp. 631–641, 2016.
- [53] E. Reihani, M. Motalleb, R. Ghorbani, and L. Saad Saoud, “Load peak shaving and power smoothing of a distribution grid with high renewable energy penetration,” *Renew. Energy*, vol. 86, pp. 1372–1379, 2016.
- [54] L. Xiao, W. Shao, M. Yu, J. Ma, and C. Jin, “Research and application of a hybrid wavelet neural network model with the improved cuckoo search algorithm for electrical power system forecasting,” *Appl. Energy*, vol. 198, pp. 203–222, 2017.
- [55] T. Yunusov, W. Holderbaum, and B. Potter, “Cost function for sub-agent elements in multi-agent energy management system,” in *2011 2nd IEEE PES Int. Conf. Exhib. Innov. Smart Grid Technol.*, pp. 1–8, 2011.
- [56] American National Standards Institute Inc., “ANSI/NEMA MG 1-2011,” tech. rep., 2011.
- [57] Power and Energy Society, “Distribution Test Feeders,” 2017.

- [58] M. Zangs, T. Yunusov, W. Holderbaum, and B. Potter, “On-line adjustment of battery schedules for supporting LV distribution network operation,” in *2016 Int. Energy Sustain. Conf. IESC 2016*, 2016.
- [59] Scottish and Southern Energy Power Distribution, DNV-GL, GE, Honeywell, L. Fund, University of Reading, and Bracknell Forest Council, “Thames Valley Vision - Project library - Published documents,” 2016.
- [60] A. H. Mohsenian-Rad, V. W. S. Wong, J. Jatskevich, R. Schober, and A. Leon-Garcia, “Autonomous demand-side management based on game-theoretic energy consumption scheduling for the future smart grid,” *IEEE Trans. Smart Grid*, vol. 1, no. 3, pp. 320–331, 2010.
- [61] H. A. Mostafa, R. E. Shatshat, and M. M. A. Salama, “A Correlated Equilibrium Game-Theoretic Approach for Multiple Participants Electric Distribution Systems Operation,” *IEEE Trans. Smart Grid*, vol. 7, no. 1, pp. 32–42, 2016.
- [62] Commission for Energy Regulation (CER), “Irish Social Science Data Archive. CER Smart Metering Project,” 2002.
- [63] M. Luck, R. Ashri, and M. D’Inverno, *Agent-Based Software Development*. Norwood, MA, USA: Artech House, Inc., 2004.
- [64] Telecom Italia, “Java Agent Development Framework,” 2015.
- [65] Foundation For Intelligent Physical Agents, “FIPA Agent Management Specification,” tech. rep., 2002.
- [66] E. L. Karfopoulos and N. D. Hatziargyriou, “A Multi-Agent System for Controlled Charging of a Large Population of Electric Vehicles,” *IEEE Trans. Power Syst.*, vol. 28, pp. 1196–1204, may 2013.

- [67] F. Y. S. Eddy and H. B. Gooi, “Multi-agent system for optimization of microgrids,” in *8th Int. Conf. Power Electron. - ECCE Asia*, (Jeju), pp. 2374–2381, Ieee, may 2011.
- [68] M.-T. Kuo and S.-D. Lu, “Design and Implementation of Real-Time Intelligent Control and Structure Based on Multi-Agent Systems in Microgrids,” *Energies*, vol. 6, pp. 6045–6059, nov 2013.
- [69] S. Mocci, N. Natale, S. Ruggeri, and F. Pilo, “Multi-agent control system for increasing hosting capacity in active distribution networks with EV,” in *2014 IEEE Int. Energy Conf.*, (Cavtat), pp. 1409–1416, Ieee, may 2014.
- [70] W. Li, T. Logenthiran, V. T. Phan, and W. L. Woo, “Intelligent Multi-Agent System for Power Grid Communication,” *IEEE Reg. 10 Annu. Int. Conf. Proceedings/TENCON*, pp. 3386–3389, 2017.
- [71] T. Nagata and H. Sasaki, “A multi-agent approach to power system restoration,” *IEEE Trans. Power Syst.*, vol. 17, no. 2, pp. 457–462, 2002.
- [72] A. L. Dimeas and N. D. Hatziargyriou, “Operation of a multiagent system for microgrid control,” *IEEE Trans. Power Syst.*, vol. 20, no. 3, pp. 1447–1455, 2005.
- [73] P. H. Nguyen, W. L. Kling, I. G. Kamphuis, and P. Ribeiro, “Integration of agent-based functions to facilitate operation of Smart Distribution Networks,” in *2011 2nd IEEE PES Int. Conf. Exhib. Innov. Smart Grid Technol.*, (Manchester), pp. 1–5, Ieee, dec 2011.
- [74] T. Nagata, Y. Ueda, and M. Utatani, “A multi-agent approach to smart grid energy management,” in *2012 10th Int. Power Energy Conf.*, (Ho Chi Minh City), pp. 327–331, Ieee, nov 2012.

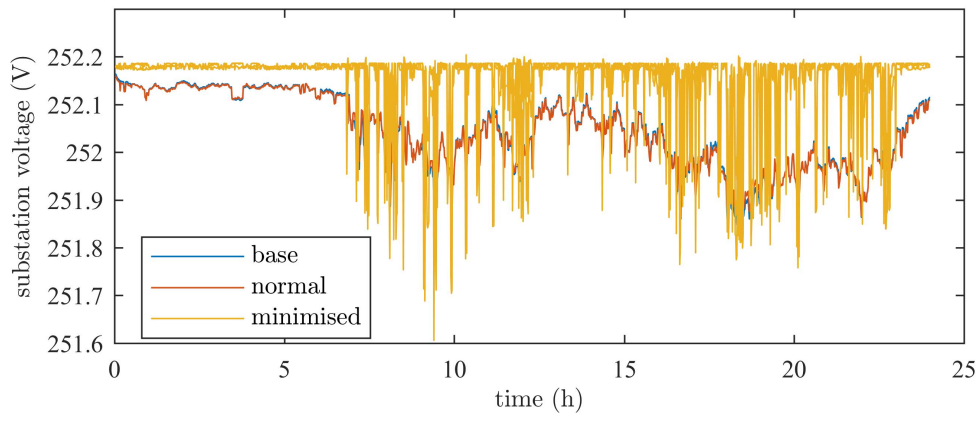
Appendix A

Additional Results

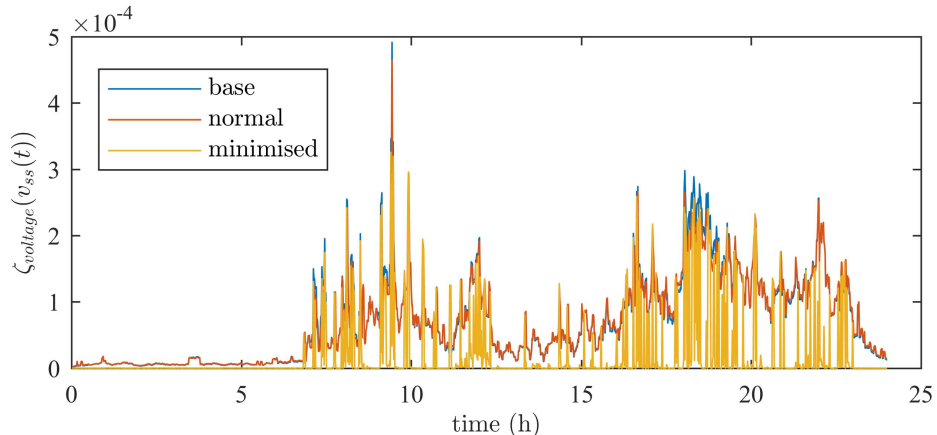
A.1 Improving operation performance of battery schedules at sub-half-hourly resolution

A.1.1 Additional Time Series Analysis

Since the plots in Section 3.5.1 are averages over a 10 minute moving average window (in order to aid visual representation of the volatile data), the raw and unfiltered data is included for reference in this appended section.

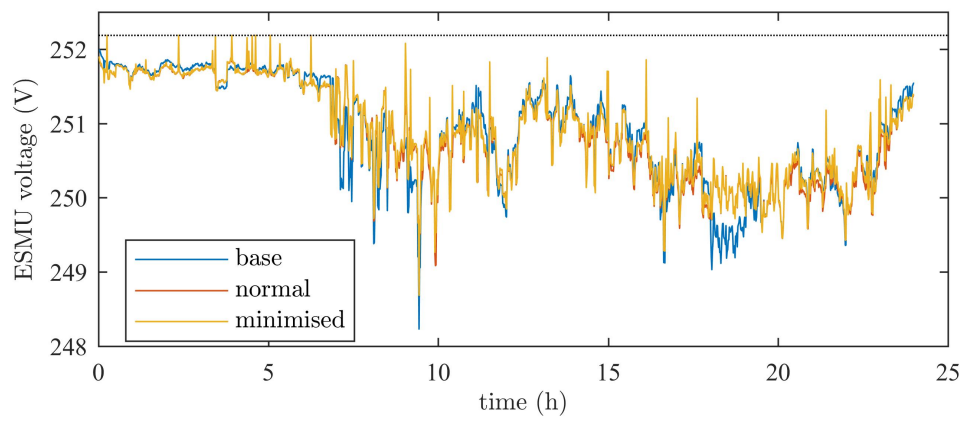


(a) Voltage levels as measured at the substation

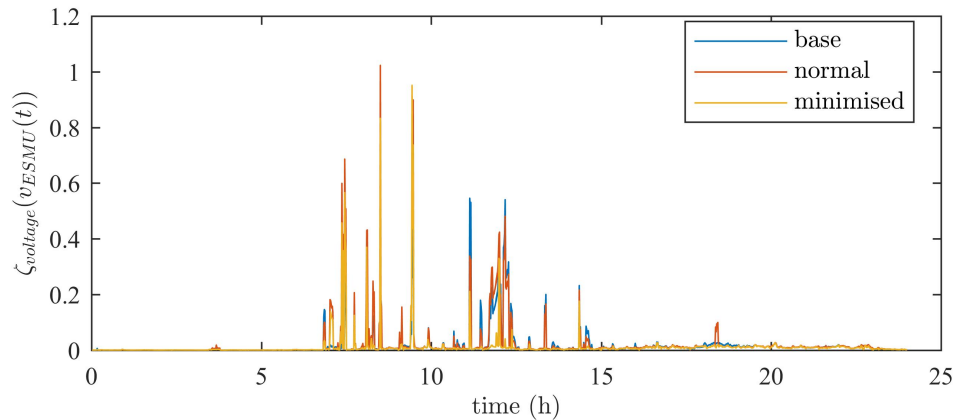


(b) Cost associated with the voltage levels as measured at the substation

Figure A.1: Additional substation voltage level comparison between base, normal and the case where the ESMU's schedule was adjusted.

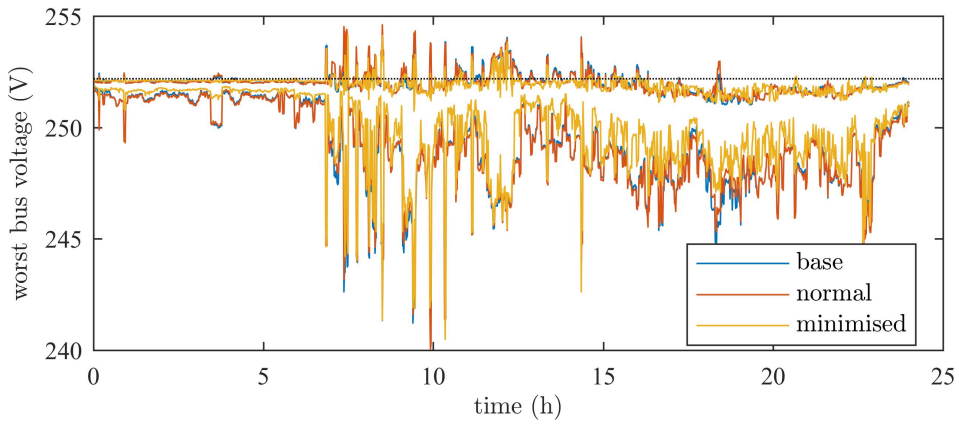


(a) ESMU voltage levels

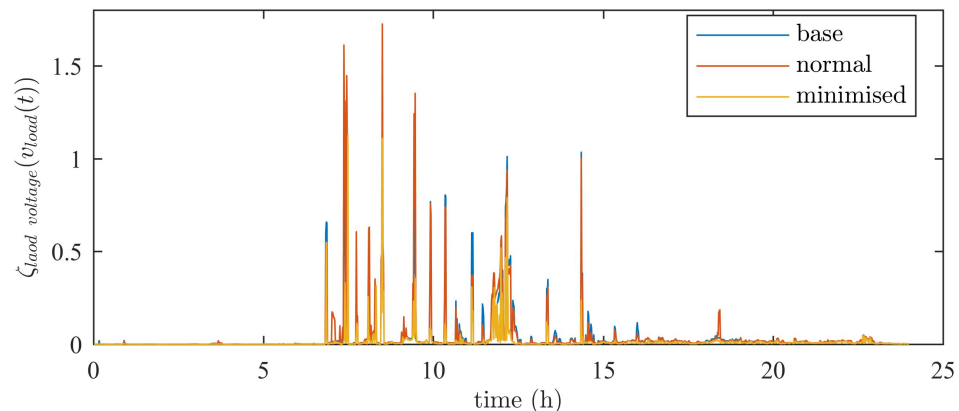


(b) Cost associated with the ESMU voltage levels

Figure A.2: Additional ESMU voltage level comparison between base, normal and the case where the ESMU's schedule was adjusted.

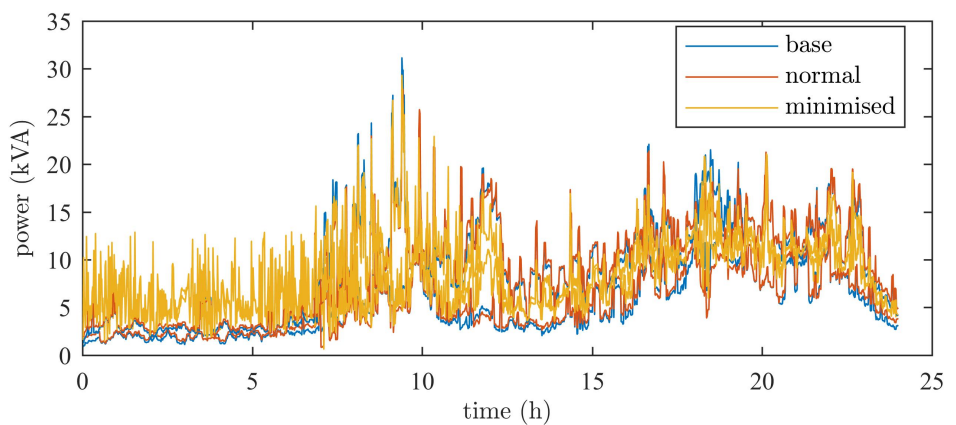


(a) Highest and lowest voltage levels in entire network

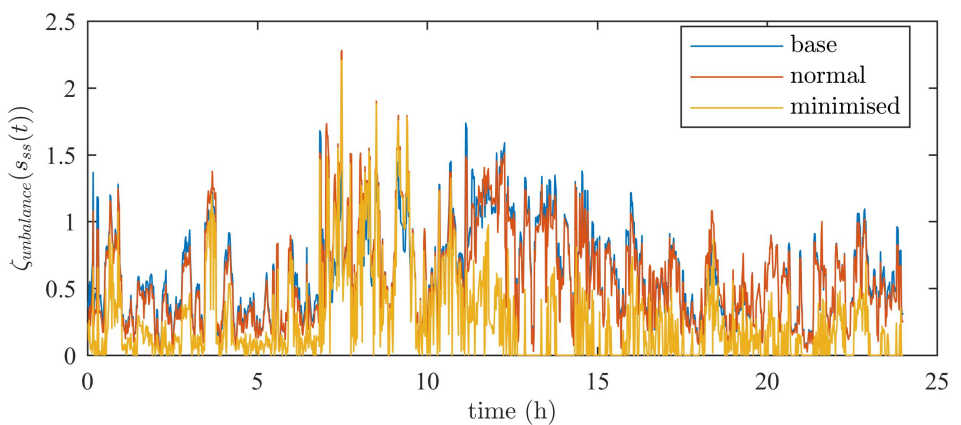


(b) Cost associated with highest and lowest voltage levels in entire network

Figure A.3: Additional voltage level comparison between base, normal and the case where the ESMU's schedule was adjusted.

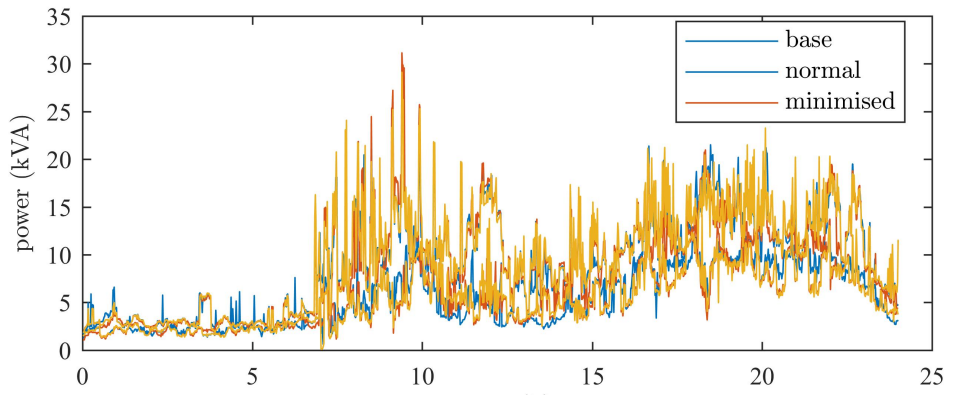


(a) Highest and lowest phase power

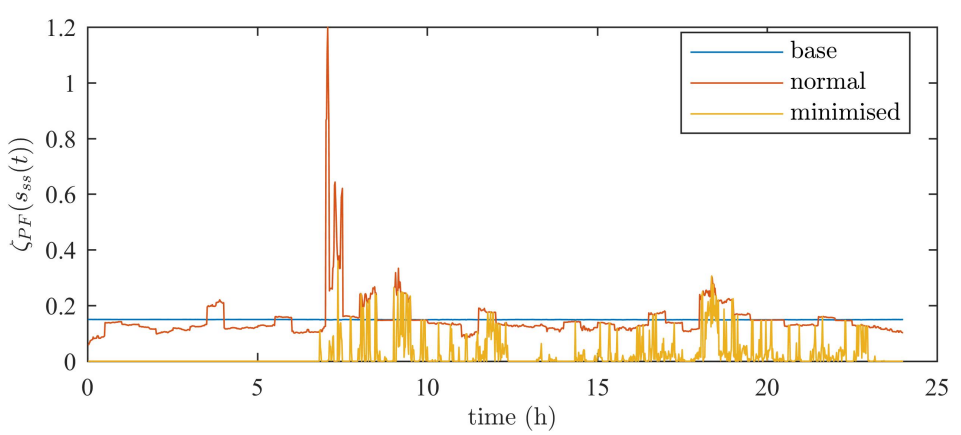


(b) Phase unbalance cost

Figure A.4: Additional phase unbalance cost comparison between base, normal and the case where the ESMU's schedule was adjusted.

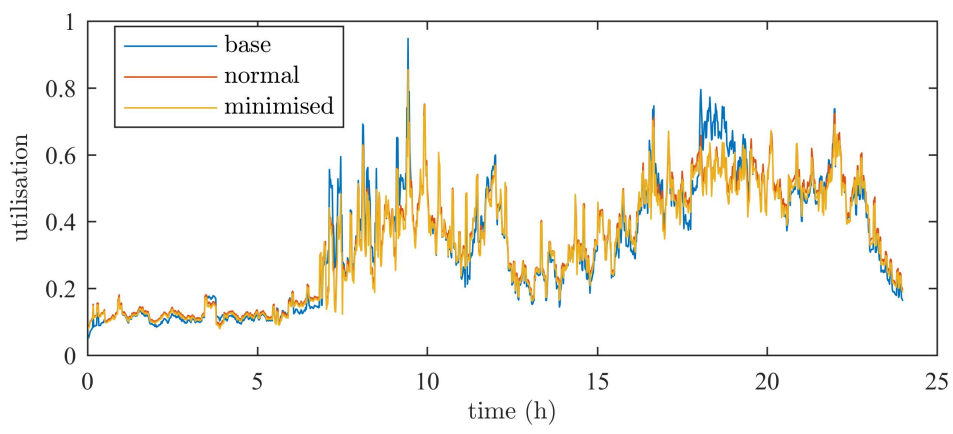


(a) Network load

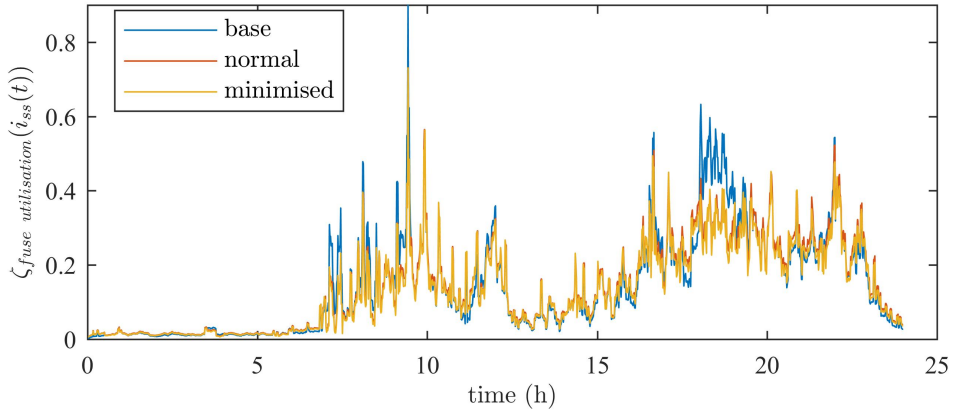


(b) Power factor

Figure A.5: Additional power factor cost comparison between base, normal and the case where the ESMU's schedule was adjusted.

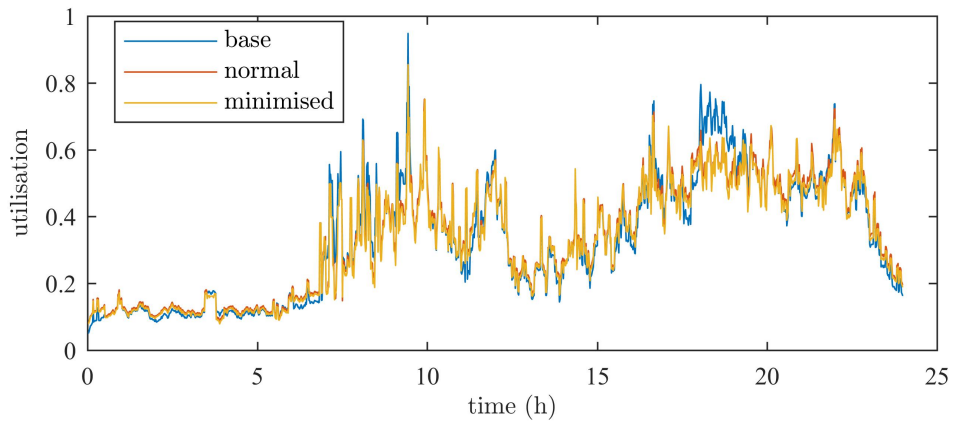


(a) Utilisation of the substation fuse

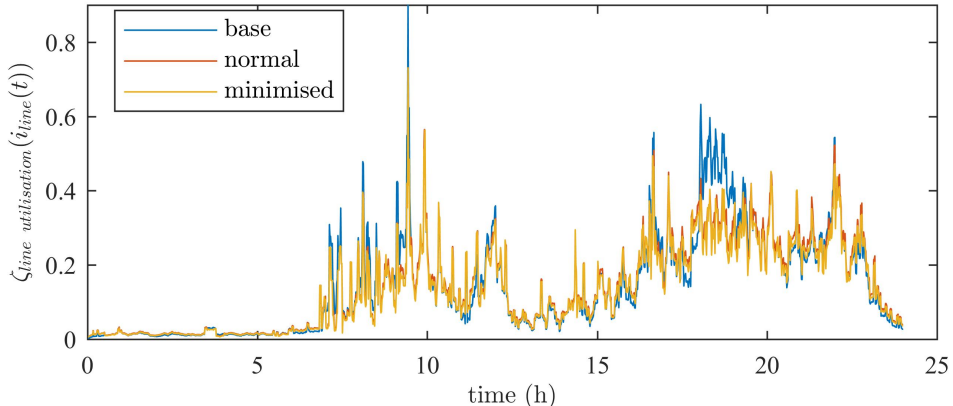


(b) Cost associated with the utilisation of the substation fuse

Figure A.6: Additional comparison of the substation fuse utilisation between base, normal and the case where the ESMU's schedule was adjusted.

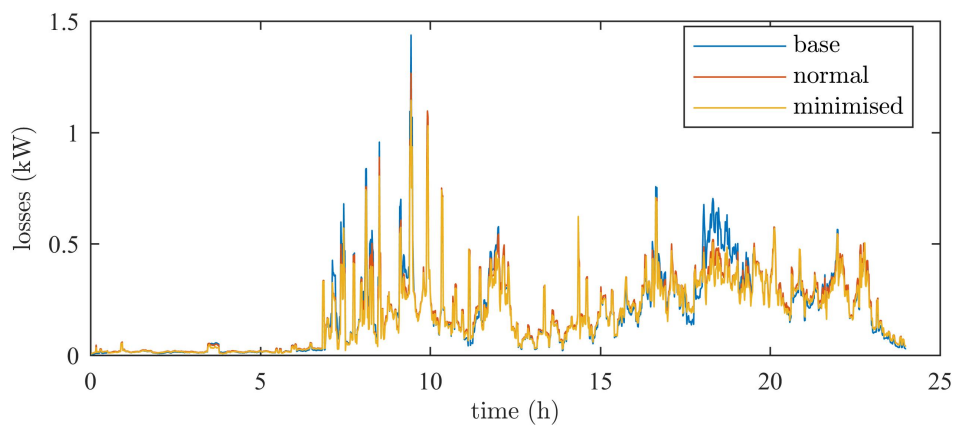


(a) The highest line utilisation of any line in the entire network

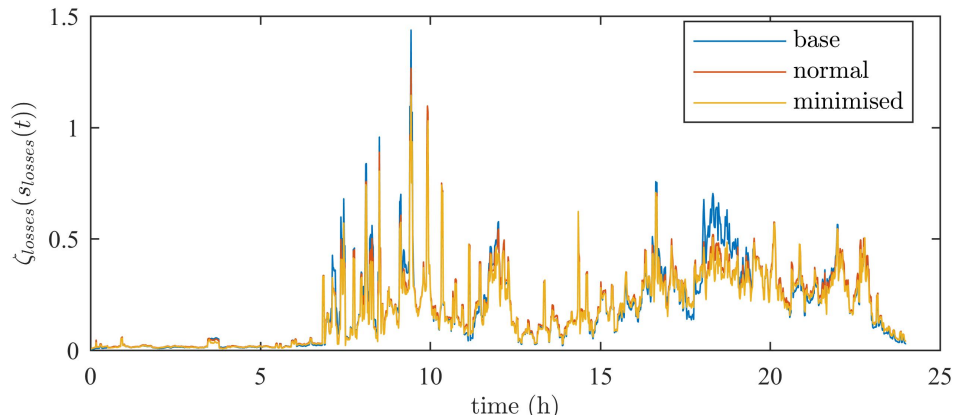


(b) The highest cost associated to the highest line utilisation of any line in the entire network

Figure A.7: Additional line utilisation comparison between base, normal and the case where the ESMU's schedule was adjusted.



(a) Distribution losses



(b) Cost associated to distribution losses

Figure A.8: Additional comparison of distribution loss cost between base, normal and the case where the ESMU's schedule was adjusted.

A.1.2 Additional Difference Analysis

Only the cost differences for the case of actual cost minimisation were compared in Section 3.5.2. Therefore, all remaining cost differences have been included in this appended section.

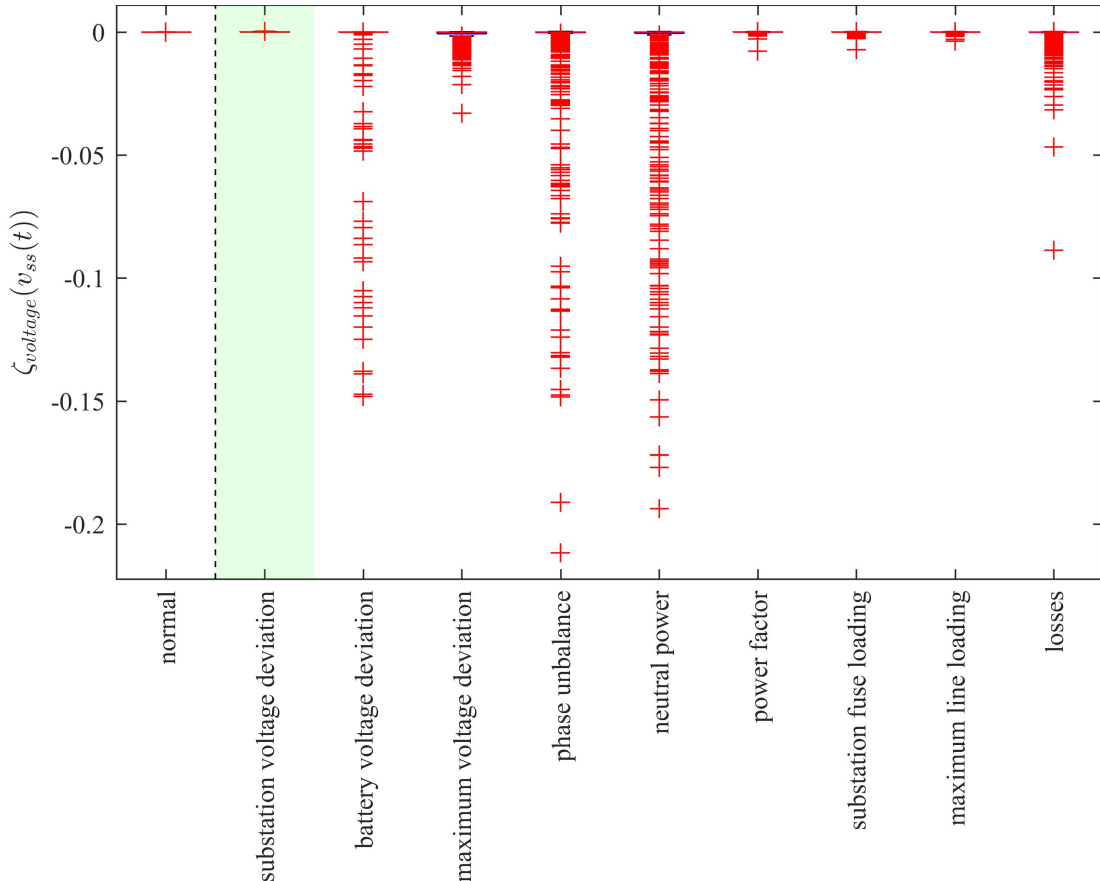


Figure A.9: Cost difference spread, based on the ESMU schedule adjustment to minimise substation voltage deviation

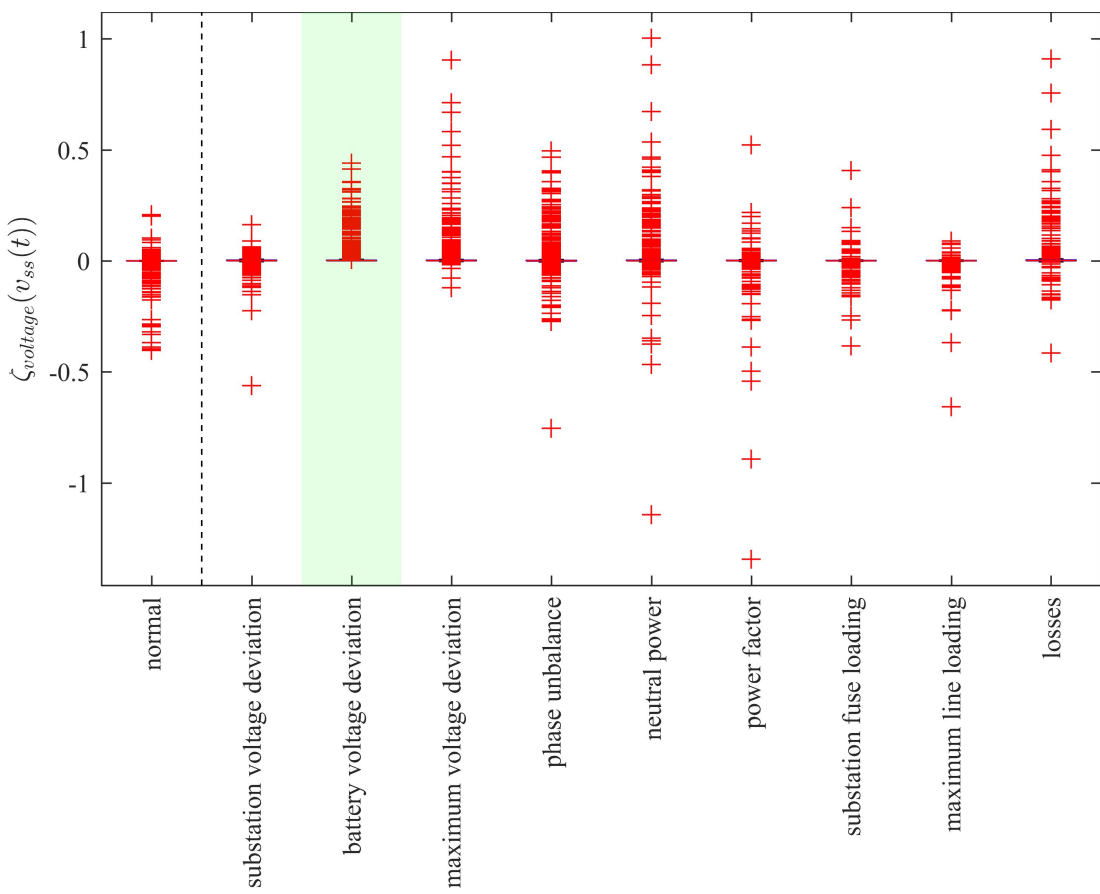


Figure A.10: Cost difference spread, based on the ESMU schedule adjustment to minimise ESMU's PCC voltage deviation

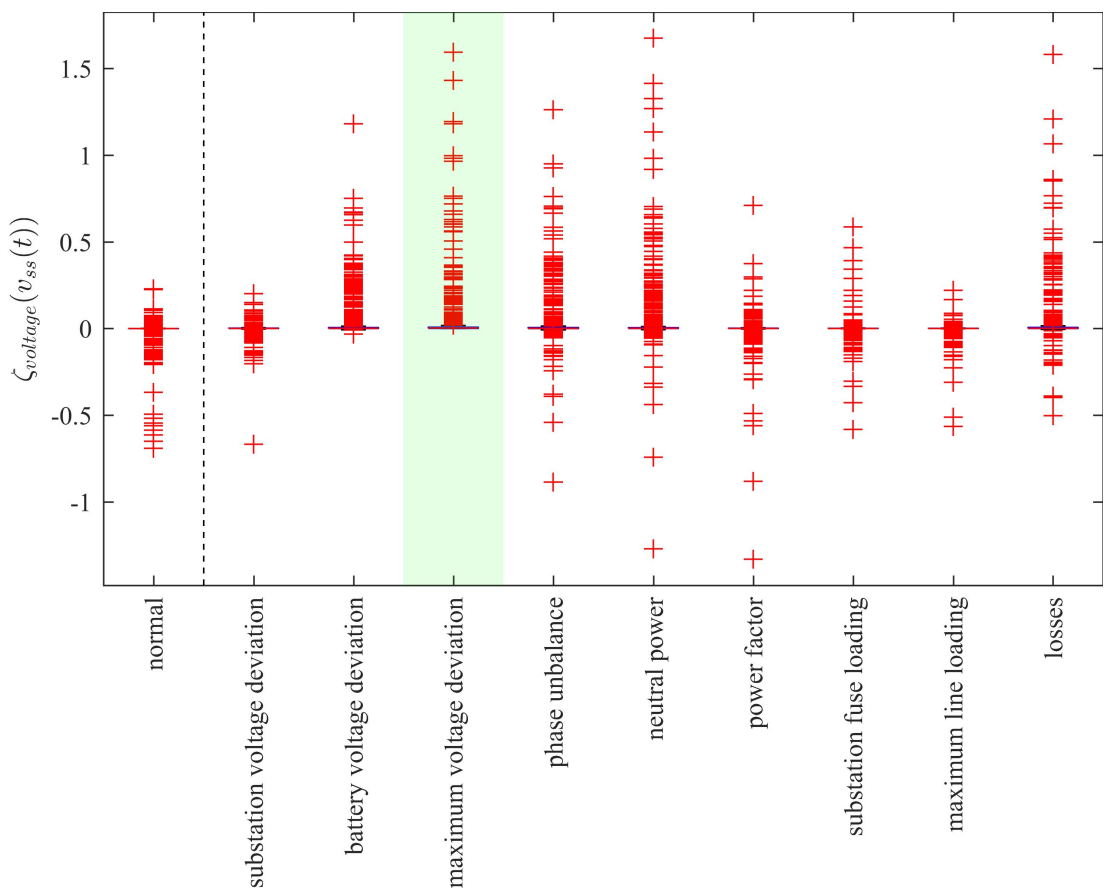


Figure A.11: Cost difference spread, based on the ESMU schedule adjustment to minimise the maximum voltage deviation on any bus of the network

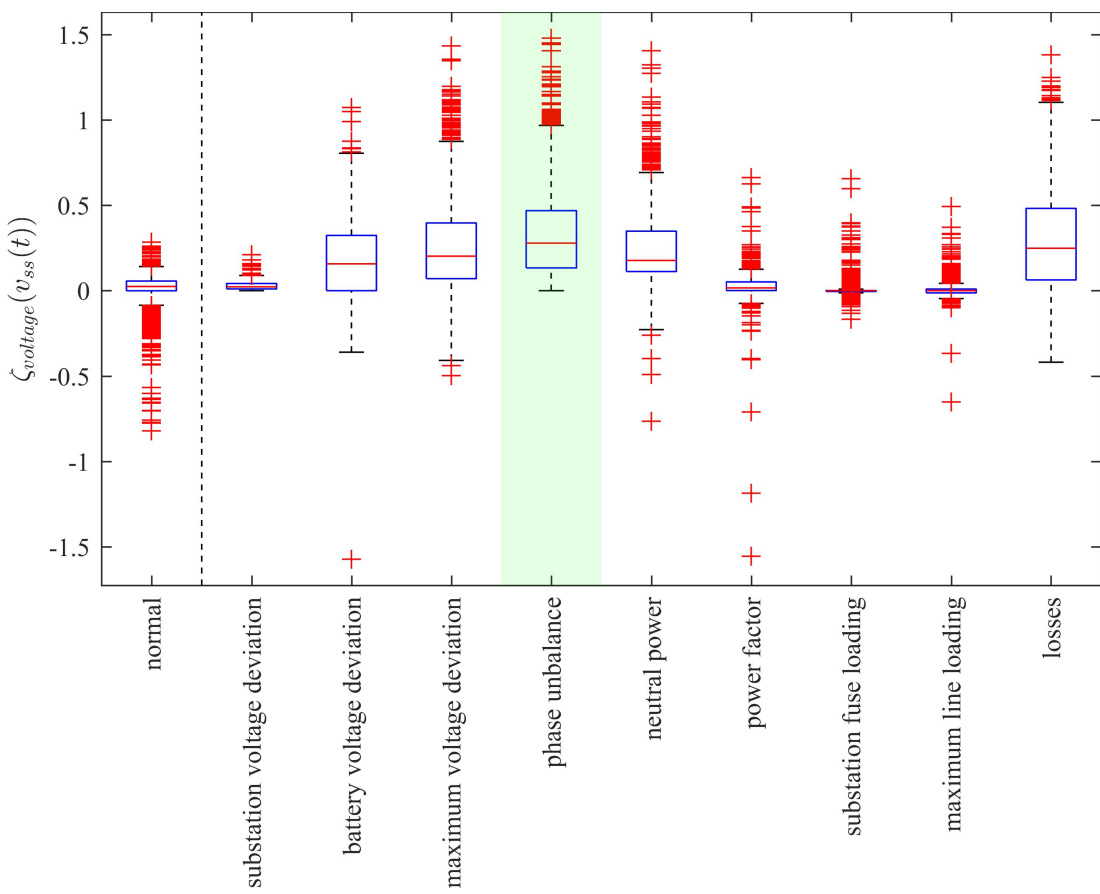


Figure A.12: Cost difference spread, based on the ESMU schedule adjustment to minimise the network's phase unbalance

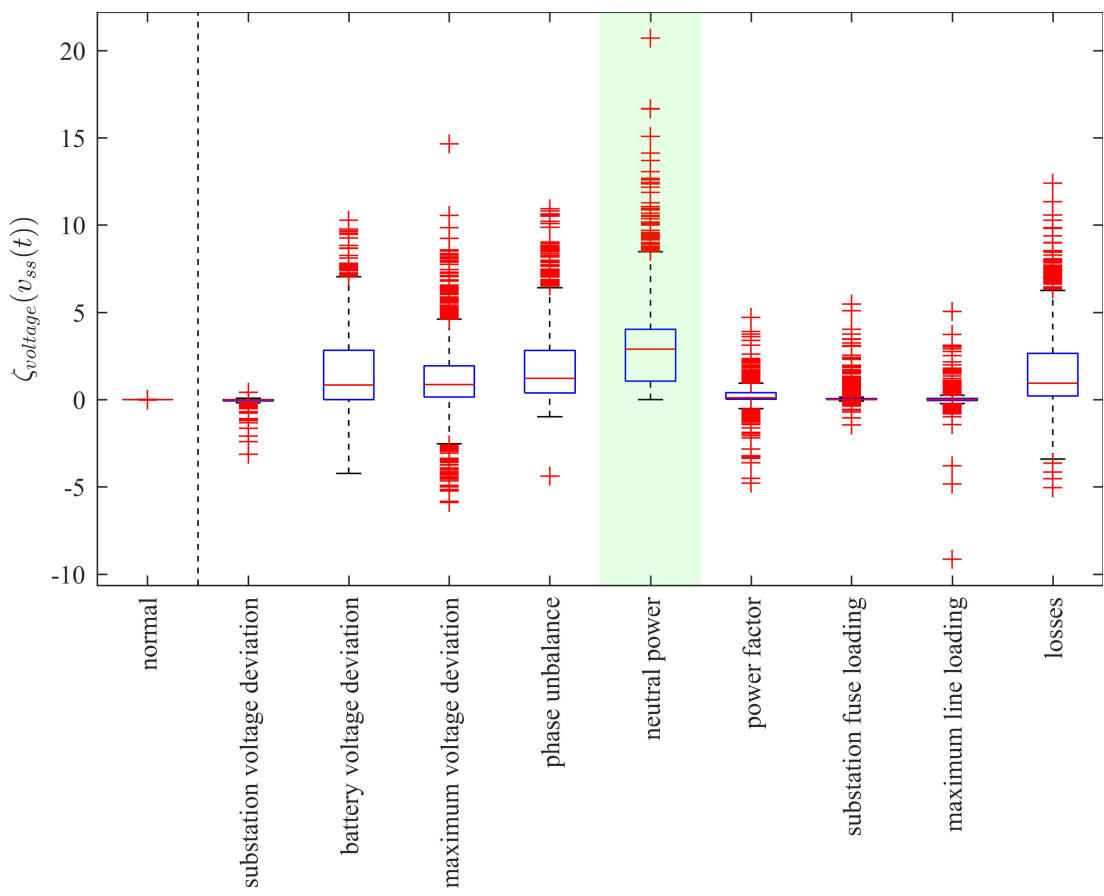


Figure A.13: Cost difference spread, based on the ESMU schedule adjustment to minimise the network's power flow in the neutral conductor

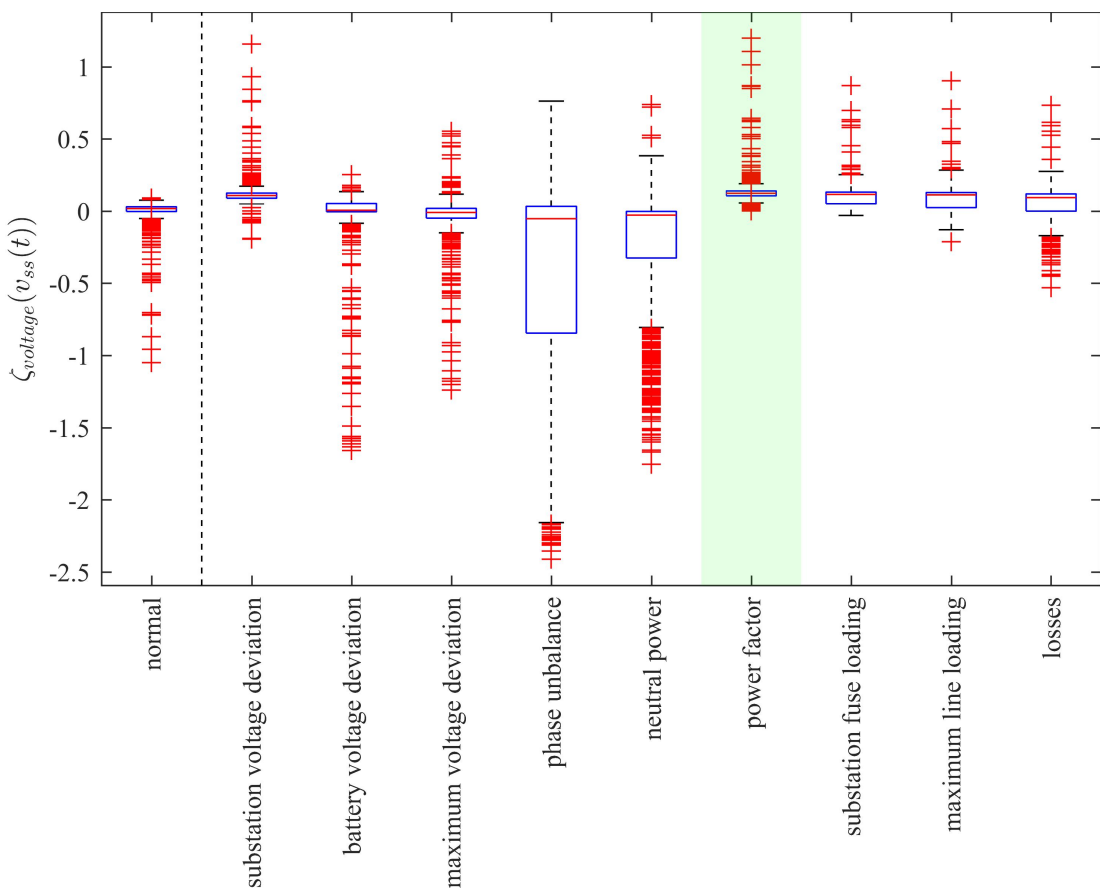


Figure A.14: Cost difference spread, based on the ESMU schedule adjustment to minimise the network's offset to unity power factor

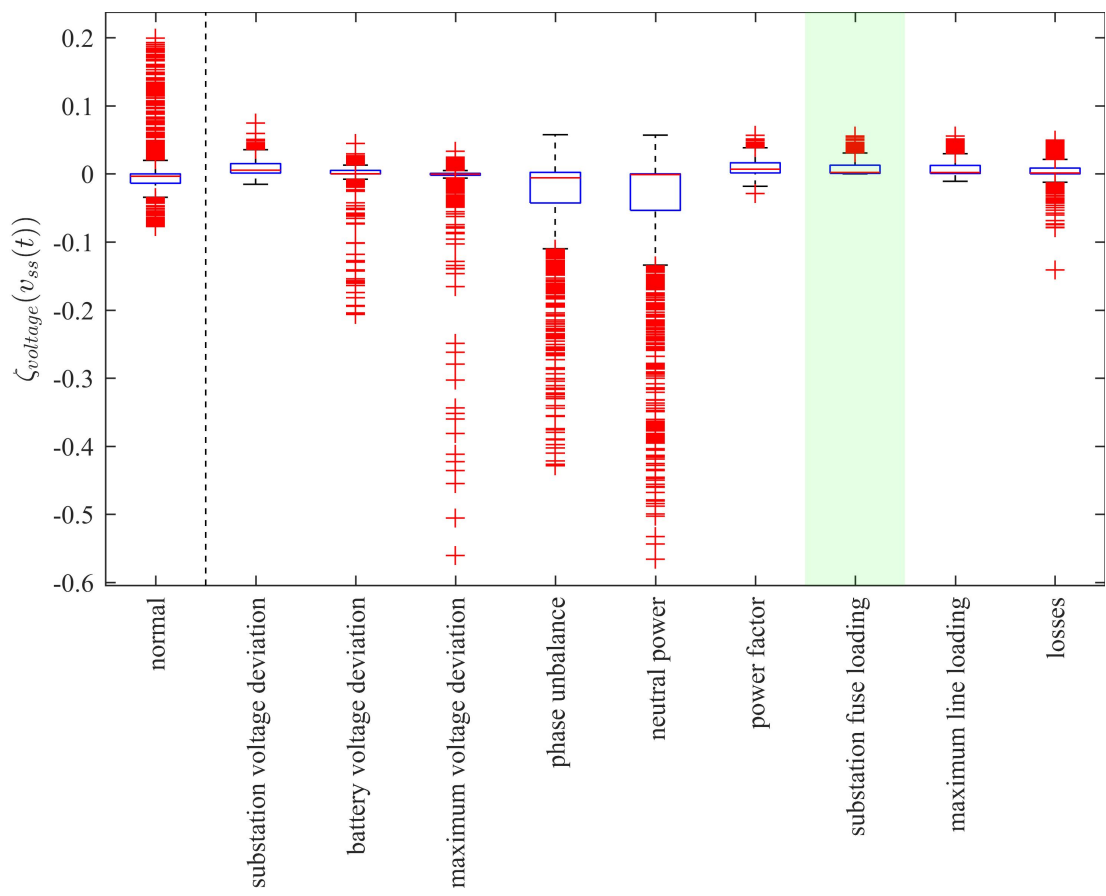


Figure A.15: Cost difference spread, based on the ESMU schedule adjustment to minimise the substation's fuse utilisation

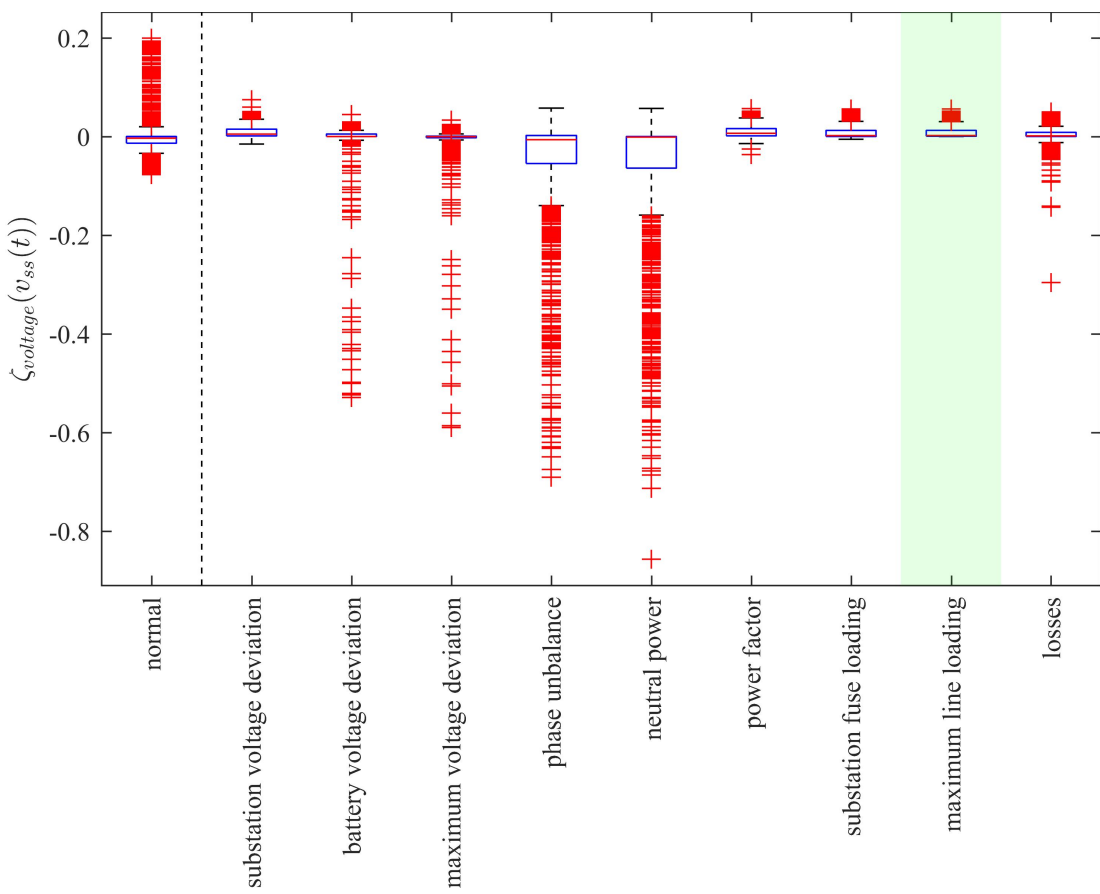


Figure A.16: Cost difference spread, based on the ESMU schedule adjustment to minimise the maximum line utilisation of any line in the network

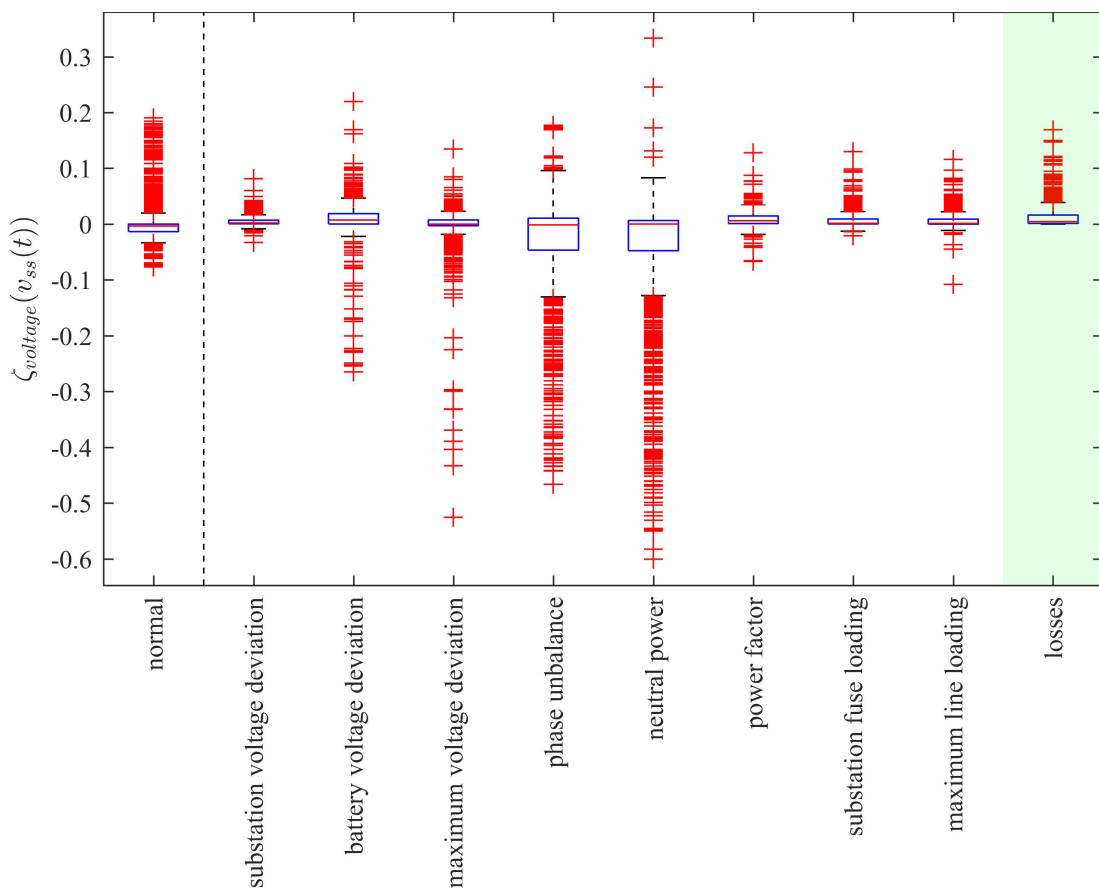


Figure A.17: Cost difference spread, based on the ESMU schedule adjustment to minimise distribution losses

A.1.3 Probability Density Analysis

The details described in this section address the prerequisites for the performed null hypothesis test in Section 3.5.3. These steps lie beyond the content of the corresponding chapter, yet have been included for completeness. Here, each step to condition the raw data for the t -test is explained in detail.

The original data is a highly volatile and non-stationary time-series that has a non-gaussian probability distribution. However, in order to apply the t -test, these criteria have to be met. Data conditioning steps were followed for each dataset that would modify the properties of the time-series without modifying their context. These steps are listed below and go as follows: First

1. the time-series is rescaled using the $\log()$ function, then
2. the rescaled values is averaged over N samples, then
3. the averages are split into two distinct sections (one prior to 11am and one after 11am), then
4. the sections are compared against each other (i.e. by computing the difference), then
5. the comparison's auto-correlation is computed to check for the presence of self-dependence.
 - (a) If the self-dependence is low enough (i.e. within confidence interval) the t -test is executed
 - (b) otherwise the data is feathered and the auto-correlation is tested again, and
 - (c) if the results still indicate a self-dependence, then a different N is chosen and the steps are repeated.

To visualise this procedure, the dataset corresponding to the minimisation of distribution losses, i.e. $\zeta_{\text{losses}}()$, is presented and the data modifications are explained. Since the steps apply to all data sets, only one is being presented in this appendix.

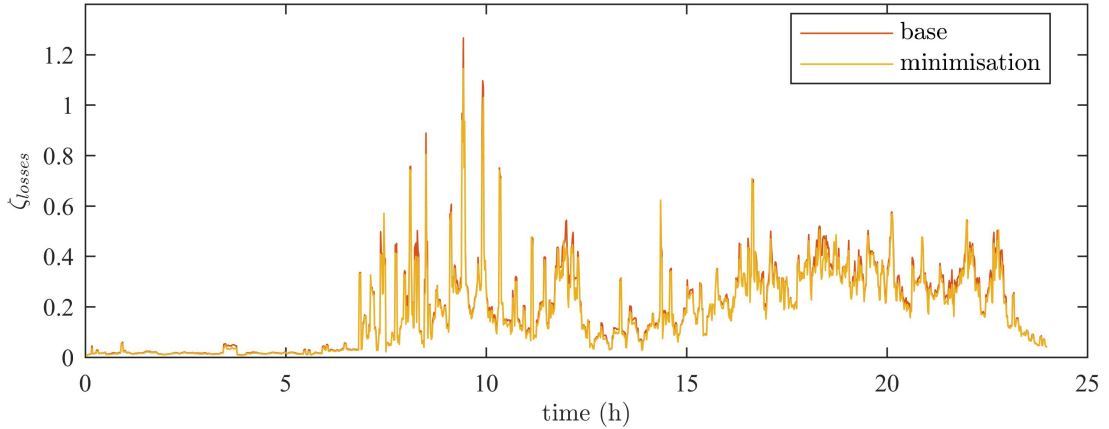


Figure A.18: Raw time-series that are supposed to be compared.

Figure A.18 shows the raw data of the two time-series that are going to be compared in the t -test. Since this data is very spiky and has many values located closely to zero, they are scaled using the $\log()$ function.

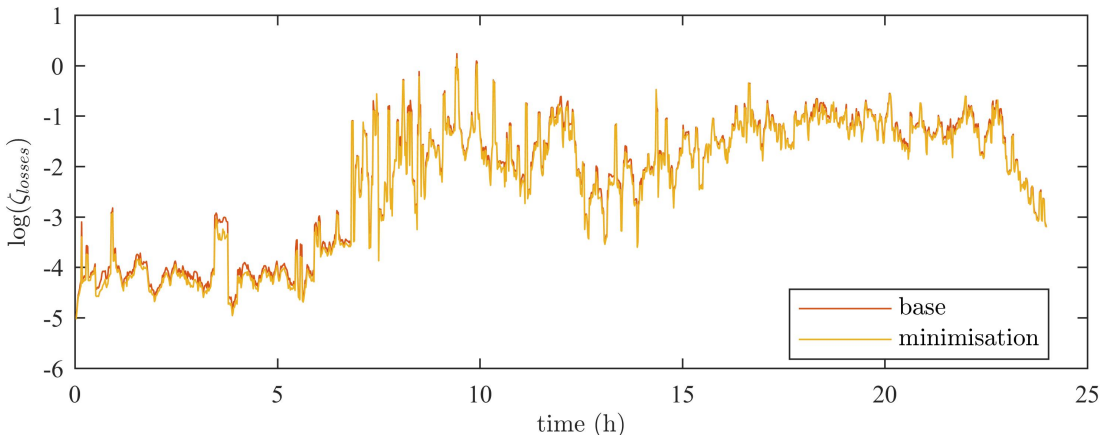


Figure A.19: Rescaled time-series that are supposed to be compared.

Figure A.19 shows this rescaled cost. It can be observed how differences, e.g. the increase in load during the morning hours, has become more apparent. Nonetheless, this data is still volatile and is averaged over N values.

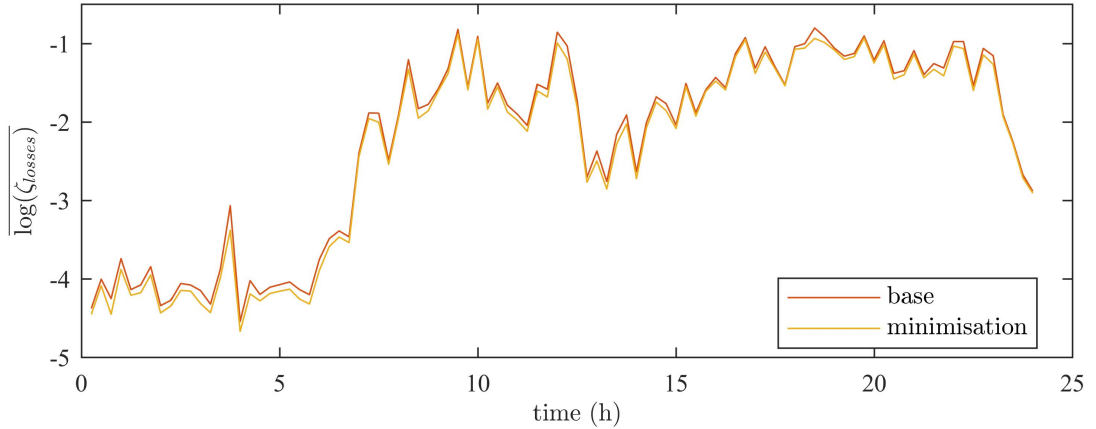


Figure A.20: Averaged log-scaled time-series.

The two different levels in the data can clearly be observed in Figure A.20. This distinction in levels allows an easy separation of the data into two sections: *morning* and *afternoon*.

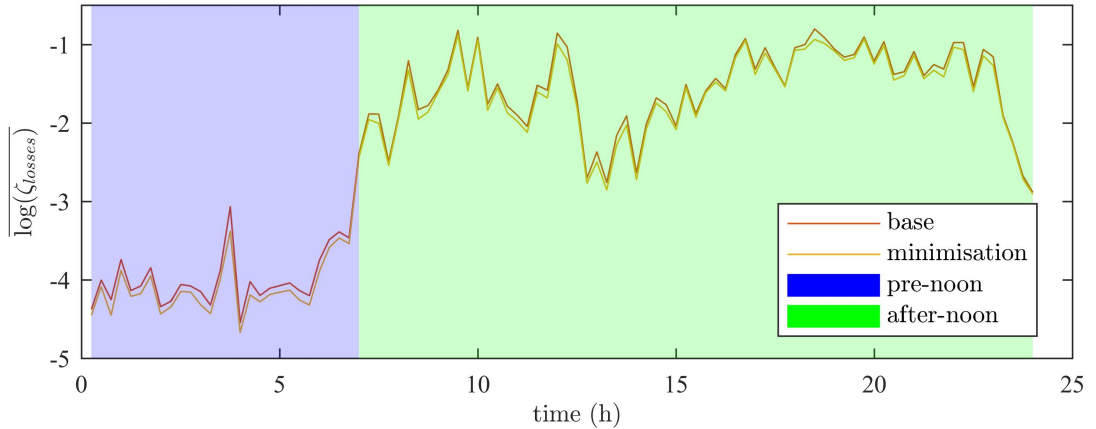


Figure A.21: Splitting of the conditioned data into two stationary sections

The preconditioned data in the two sections, that are highlighted in Figure A.21, are now compared by computing their difference. Figure A.22 shows this difference.

This difference is now auto-correlated and to indicate if any “self-dependence” (i.e. indicating auto-regression) is still present in the data. Results from both sections are shown in Figure A.23

Using the statistics package *MINITAB*, the significance bounds are determined. If any auto-correlation value lies outside this bound, then the data still contains

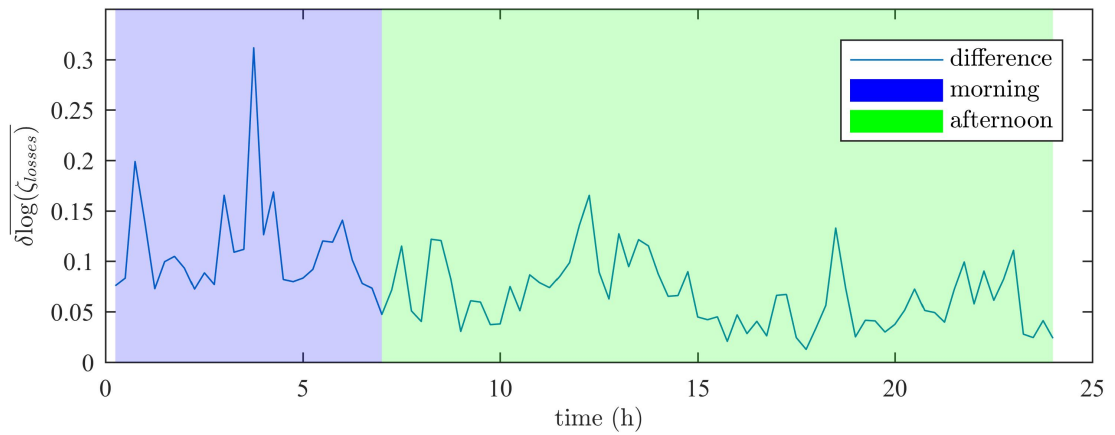


Figure A.22: Difference of the two pre-conditioned time-series.

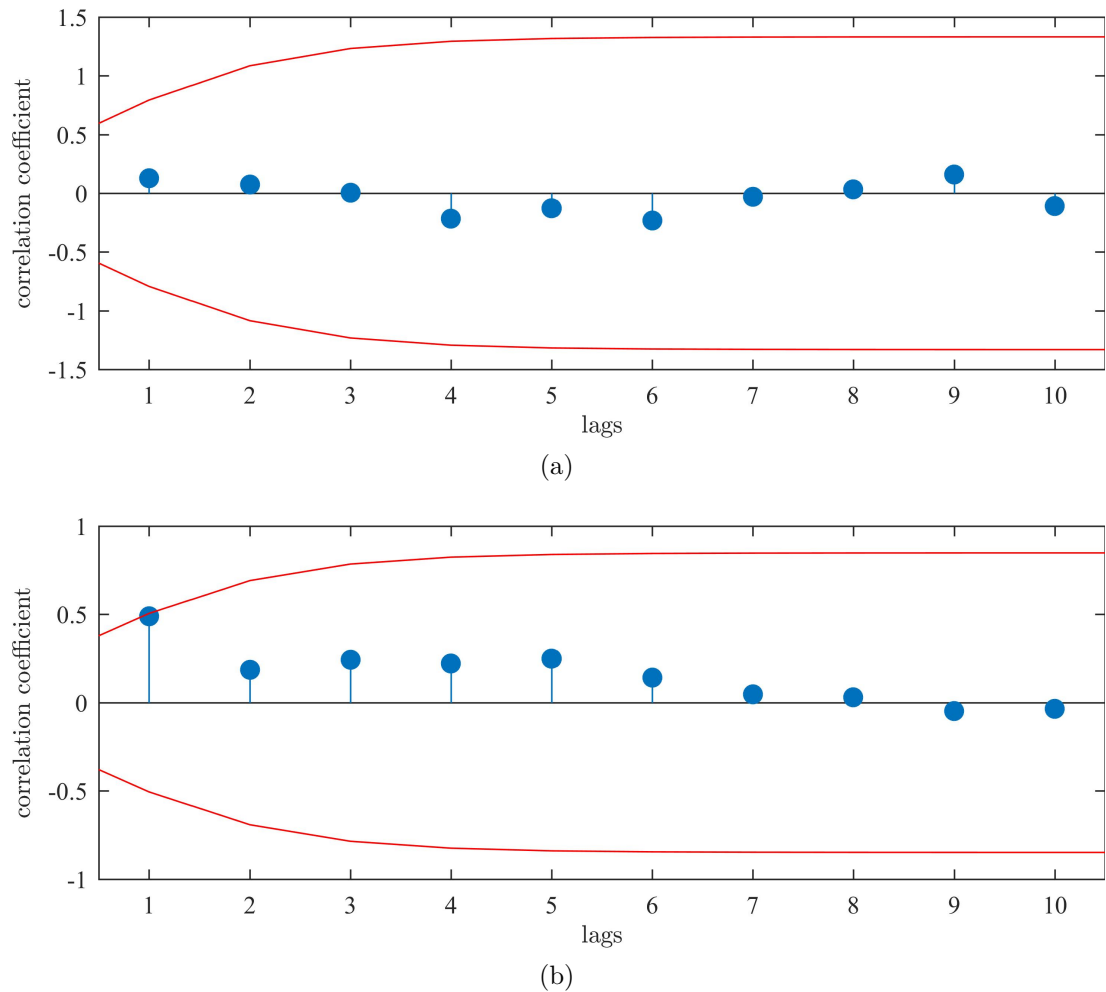


Figure A.23: Auto-correlation of signal for (A.23a) morning and (A.23b) afternoon sections

significant self-dependence and must be re-conditioned. In the case presented in Figure A.23 however, the auto-correlation indices lie within the bounds for all lags. Therefore, the criteria for the *t*-test are met and the data can be assessed. In this case, the *t*-test resulted in $p < 0.001$, which is the same value that is used in the “Probability Density Analysis” Section 3.5.

Appendix B

Multi-Agent Systems

B.1 FIPA Implementation

B.2 Communication Protocols

Appendix C

Stochastic EV Demand Model

Appendix D

Network Simulation Interface

D.1 OpenDSS

D.2 Java

D.3 MATLAB

D.4 Python